

Momentum Spectroscopic Studies of Atomic and Molecular Ionisation

A THESIS

submitted for the Award of Ph. D. degree of

MOHANLAL SUKHADIA UNIVERSITY

in the

Faculty of Science

by

Vandana Sharma



Under the Supervision of

Bhas Bapat, Reader, Physical Research Laboratory, Ahmedabad

DEPARTMENT OF PHYSICS

FACULTY OF SCIENCE

MOHANLAL SUKHADIA UNIVERSITY

UDAIPUR

Year of submission: 2007

To
my parents
and
teachers

Contents

Certificate	ix
Declaration	xi
Abstract	1
1 An overview	3
1.1 Probing at the atomic scale	3
1.2 Electron-molecule collisions	4
1.3 Birth of Momentum Spectroscopy	7
1.4 Motivation and outline of the work	10
2 The Ion Momentum Spectrometer	13
2.1 Requirements	13
2.2 The experimental set-up	14
2.2.1 Collision geometry	14
2.2.2 Extraction of reaction products	15
2.2.3 Electron detector	17
2.2.4 Ion imaging detector	18
2.3 Optimisation of spectrometer performance	22
2.3.1 Projectile-target overlap	22
2.3.2 Signal processing	24
2.4 List Mode Data Acquisition	26
2.5 Building the ion momentum vector	29
2.6 Test results	31

3	Multi particle coincidence and momentum maps	35
3.1	Multi-ion coincidence	36
3.2	Coincidence momentum maps	38
3.3	Information from TOF coincidences	39
3.3.1	Dissociation channels	39
3.3.2	Lifetime of metastable ions	41
3.4	Information from full momentum maps	42
3.4.1	Geometry estimation	43
3.4.2	Energy levels	45
3.5	Need for quantum chemical calculations	47
4	Fragmentation of a linear triatomic : CO₂	49
4.1	Break-up channels	50
4.2	Two body break-up	50
4.2.1	Lifetime of metastable CO ₂ ²⁺	52
4.2.2	Potential energy surface of molecular ion	53
4.3	Three-body break-up	54
4.3.1	Geometry of dissociating molecular ion	56
4.4	Considerations for polyatomics	60
5	Fragmentation of symmetric polyatomics : CCl₄, SF₆	61
5.1	Stability patterns in molecular ion fragments	62
5.2	Migration of atoms during dissociation	68
5.3	Alteration in geometry	69
5.4	Effects due to asymmetry	76
6	Site specific dissociation: C₂H₅OH	77
6.1	Tools of trade: Isotopic substitution	78
6.2	Identification of fragment ions	79
6.2.1	Ions not requiring rearrangement of bonds	81
6.2.2	Ions requiring rearrangement of bonds	82
6.3	Decay channels of C ₂ H ₅ OH ²⁺	86

<i>Contents</i>	vii
6.3.1 Preferred channels	88
6.3.2 Electronic energy levels	88
6.3.3 Open questions	89
7 Summary and future direction	91
7.1 Summary of the present work	91
7.2 A view into the future	93
Bibliography	95
Publications	105
Acknowledgements	109

Certificate

I feel great pleasure in certifying that the thesis entitled “Momentum Spectroscopic Studies of Atomic and Molecular Ionisation” embodies a record of the results of investigations carried out by Vandana Sharma under my guidance. I am satisfied with the analysis of data, interpretation of results and conclusions drawn.

She has completed the residential requirement as per rules.

I recommend the submission of thesis.

Date:

Name and Designation of Supervisor

Declaration

I hereby declare that the work incorporated in the present thesis entitled “Momentum Spectroscopic Studies of Atomic and Molecular Ionisation” is my own work and is original. This work (in part or in full) has not been submitted to any University for the award of a Degree or a Diploma.

Signature of the Candidate.

Abstract

This thesis concerns the study of fragmentation dynamics of highly charged triatomic and polyatomic molecular ions created by high energy electron impact on neutrals. A momentum spectrometer was designed and assembled to carry out the study. An event-by-event reconstruction of the momentum space spanned by the fragments helped us to study various aspects of dissociation, such as identification of channels, lifetime of metastables, kinetic energy release, angular distribution of fragments and preferential bond breaking. Some deductions are supported by quantum chemical computations.

The symmetry of a molecular ion is often different from that of the ground state of the neutral. For a linear triatomic, CO_2 , we deduced that geometry of the dication is different from that of the neutral. For polyatomics such as CCl_4 and SF_6 , the change is very substantial and involves migration of atoms. In addition, we have identified certain stability patterns in the fragments. The stability depends on the possibility of forming filled hybrid molecular orbitals, which in turn is related to even/odd electron numbers in the fragment ions. In asymmetric polyatomic molecules which have a few identical atoms attached to different skeletal atoms, such as $\text{C}_2\text{H}_5\text{OH}$, we have observed association of atoms during dissociation. This is reflected in the formation of H_2^+ and H_3^+ . We determined the site-specific probability of such rearrangements. Contrary to the expectation based on bond strength, we find that the O–H bond breaks preferentially over C–O or C–H bonds, depending on the dissociation channel.

Chapter 1

An overview

1.1 Probing at the atomic scale

Atoms and molecules form everything that we see around us. Many efforts have been made in order to understand the structure of atoms and molecules. How does one look inside atoms or molecules and locate an electron? In order to determine the position of an object we must somehow ‘see’ it. In our normal experience, this is done by reflecting or scattering light from the object to the observer’s eyes. When observing an object as small as an electron, its interaction with a single photon or a charged particle is to be considered.

The first scattering experiment to understand the structure of atoms was done by Rutherford in 1911. The inference drawn from the experiment was that the atom consists of a positively charged heavy nucleus with negatively charged electrons arranged around it; the electrons occupy a volume many times larger than that occupied by the nucleus.

The information about the static structure of atoms, like binding energies and electronic energy levels of the electrons, have been investigated successfully – both theoretically and experimentally. This is reflected in the comprehensive databases available for atomic and ionic energy levels and transition probabilities [CHIA, NIST]. On the other hand, we still face a problem in investigating the dynamic situation (that is, the response of atoms to external perturbations) in atomic scattering reactions like single ionisation of helium by photon or charged particle impact. The dynamics of a molecule are far more complex, and difficult

to investigate, compared to those of atoms.

The investigation of molecular structure parallels the study of atomic structure in some ways. A major part of the study of molecular structure is the description of the bonds which are formed between atoms. Atoms are held together in a molecule by an attractive potential energy. This potential energy varies with the distance between the two atoms in a molecule and is represented by a potential energy curve (PEC). In polyatomic molecules, the potential energy is a function of several internuclear distances and angles, and is represented by a potential energy surface (PES).

The dynamics of molecules are probed by photons or charged particle impact. An easily available projectile is an electron. Energy of the incident particle is an important parameter. If the energy is high enough, multiply charged molecular ions may be formed. A molecule and its molecular ion are different entities in many respects. A molecule is more stable as compared to its molecular ions. Singly charged molecular ions are generally more stable than multiply charged molecular ions. Being unstable, molecular ions relax via different pathways, because of which numerous changes can occur: change in bond lengths and bond angles, dissociation into various fragments, etc. The decay pathway is governed by the PES of the precursor molecular ion involved in the dissociation. Hence, the knowledge of PES will help us to understand the dynamics of dissociation. In addition, substantial change in the geometry of molecular ions may occur, leading to an unexpected conformation. The changes may also involve dissociation of some bonds followed by formation of new bonds. Our knowledge of these processes is very little. The study of the above mentioned processes brought about by electron impact on molecules is the mainstay of this thesis.

1.2 Electron-molecule collisions

The collision of an electron with a molecule may lead to a number of different effects. Collisions are categorised as elastic and inelastic collisions. In elastic collisions, no energy is transferred to the internal motion of the molecule. In inelastic

collisions, some kinetic energy is lost by the electron in the excitation of internal degrees of freedom of the molecule. Further classification of inelastic collisions can be made as ionising and non-ionising collisions, depending on whether or not sufficient energy is transferred for ejection of one or more electrons from the molecule. Non-ionising inelastic collisions cause excitation of molecular states.

The perturbation of the molecule by an electron depends on the velocity of the projectile electron. The velocity of the projectile electron, v_p , relative to the velocity of the valence electron of the molecule, v_e , often influences the outcome of the perturbation. The ratio v_p/v_e is the parameter employed for categorising low and high energy collisions. Low energy collisions are those for which $v_p/v_e < 1$ while for high energy collisions $v_p/v_e \geq 1$.

A slow electron spends large amount of time near the molecule and affects the molecular wave function in a non-perturbative regime. An electron of low energy may combine with the molecule and form a transient negative molecular ion, which dissociates promptly. Slow electron collisions do not follow optical selection rules [Chr83, Mor83]. Transitions to symmetry and / or spin-forbidden states are easily achieved, especially at large scattering angles (i.e. for large momentum transfer). The reason for deviations from the optical case is that in the optical case the electric dipole interaction dominates, while in the latter case all orders of multipoles and electron exchange terms are important [Chr83, Mor83, Mas69]. This relaxation of optical selection rules makes possible the study of energy levels which are not accessible by optical methods. Collisions may often access metastable states. A large number of molecular electronic states have been discovered by low energy, large scattering angle electron impact excitation.

At high impact energy the electron spends very little time near the molecule. The interaction time is short, the momentum transfer by the projectile to the target molecule is small and scattering angles close to zero dominate. In high energy electron scattering the target experiences a sharply pulsed (in time) electric field. The interaction can be treated as a perturbation, and the post-collision interaction between the projectile and the ionisation products can be neglected. Due to short collision times, it can be described in terms of first order perturba-

tion theory. This is the Born approximation [Bor26]. It is valid when the incident electron energy is high compared to the binding energy of the bound electron to be excited or ionised.

In high energy collisions, ionisation generally is the dominant channel, followed by the dissociation and excitation channels. However, in low to intermediate energy collisions, it is not possible to separate out a dominant channel because often many inelastic channels strongly couple with one another. Developing an accurate theory of low energy electron impact is quite difficult because of many coupled channels.

Complete information about a collision can be obtained from a fully differential cross-section, i.e. cross-section differential in all observables of the final state. A fully differential cross-section can in fact be directly compared to the square of the transition matrix element [Kel00]. Any cross-section integrated over one or more observable gives us rather less information, but experimental difficulties usually leave us with just that much. To obtain such cross-sections, it is necessary to have kinematically complete information (barring the spin) which means that momenta, or angles and energies, of all involved particles have to be observed in coincidence.

The first kinematically experiment was on single ionisation of helium by electron impact in 1969 [Ehr69, Ama69]. This experiment detected the scattered and the ejected electrons simultaneously and measured their angular and energy distributions. Such experiments are known as $(e, 2e)$ experiments where ' e ' represents 'projectile electron' and ' $2e$ ' represents 'scattered and ejected electron'. Complete kinematic information was obtained by scanning the spectrometer over all emission angles and energies. The efficiency for angle and energy resolved detection was in the range 10^{-3} – 10^{-6} for one electron detection. For electron pair detection it was not better than 10^{-7} . The next logical step was kinematically complete double ionisation experiments, i.e. $(e, 3e)$ experiments. The first $(e, 3e)$ experiment was done by Lahmam-Bennani *et al* in 1989 in which all the energies and directions of the three outgoing electrons were measured in coincidence [Lah89]. In a related development, the first photo-double-ionisation

experiment was done on helium in 1993 [Sch93] using similar coincidence techniques. The simultaneous detection of two or more electrons yielded extremely small coincidence rates. One of the fundamental technical challenges for these fully differential experiments was the small solid angle coverage. For a complete 4π solid angle coverage the apparatus had to be rotated in small steps, which was a time consuming process and needed long term stability of the apparatus. The momentum space imaging technique discussed in next section is a concept to overcome this basic problem. It covers a 4π solid angle for the coincident, three dimensional, momentum resolved measurements of ions and electrons from atomic and molecular reactions, without the need for step-by-step scanning.

1.3 Birth of Momentum Spectroscopy

Momentum spectroscopy was first realised experimentally for studying ion-atom collisions in 1992 by Ali *et al* [Ali92]. The final state of the projectile ion was estimated by complete momentum measurement of the scattered projectile and ions created in the interaction volume. The idea behind momentum spectroscopy is as follows. Consider a well localised and nearly stationary ensemble of target atoms or molecules, ionised by charged particle impact or by photoabsorption. A homogeneous electric field guides the ions and electrons formed in the reaction to a position (x, y) on the plane of a detector placed perpendicular to the applied electric field, following a flight of duration t from the instant of the reaction (refer Figure 1.1). The motion of the fragments is completely determined by their initial position, the momentum balance in the reaction, and the electric field. From the positions and flight time of the detected ions the trajectories of ions are reconstructed and the three momentum components (p_x, p_y, p_z) of are derived.

With the newly developed techniques the complete momentum vector of the recoil ion emerging from an atomic collision was measurable with a good momentum resolution and a solid angle of nearly 4π sr [Dor93]. The final state mo-

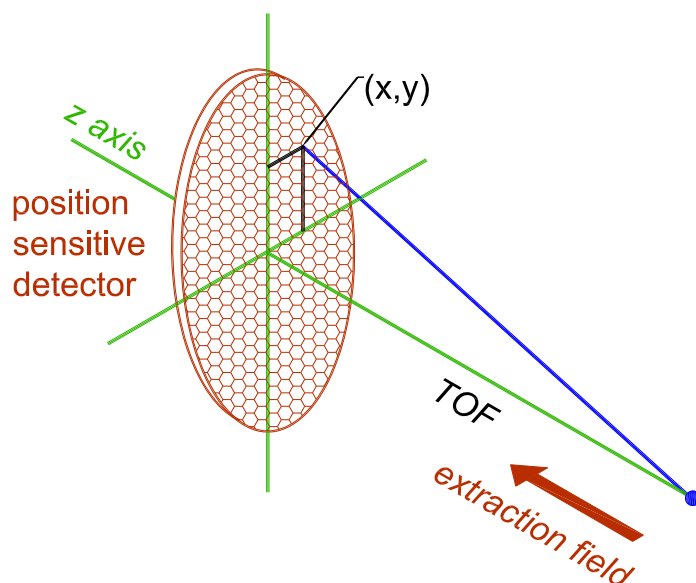


Figure 1.1: Illustration of temporal and spatial dispersion of ions in an electric field. Such dispersion is the basis of the momentum spectroscopy technique.

menta of the products of a reaction are interrelated by three momentum and one energy conservation law. Thus, if N particles are created in the final channel then it is necessary to measure $3N - 4$ momentum components for a complete kinematic experiment. The four remaining components can be extracted from momentum and energy conservation laws. This was first demonstrated in an experiment by Ali *et al* for single ionisation of helium by Ar^{8+} impact [Ali92]. The azimuthal and polar scattering angles of the projectile were measured in coincidence with the three dimensional momentum vector of the recoil ion. The energy loss of the projectile and the momentum of the emitted electron was later on deduced using conservation laws. However, in many fast ion-atom collisions the relative momentum change of the projectile is very small (typically $\Delta p/p < 10^{-5}$) and cannot be directly measured. In such cases coincident momentum measurement of ion and electron provides the only access to fully differential cross sections. Experimental set-ups incorporating simultaneous electron and ion momentum measurements are known as *reaction microscopes* [Mos96a]. The first kinematically complete experiment using a reaction microscope was single ioni-

sation of Helium by impact of Se^{28+} , done by Moshhammer *et al* [Mos96b, Mos97]. Complete momentum map of He^+ and the ejected electron was obtained and the small change in the projectile momentum was deduced. This was possible only because of event-by-event momentum mapping of the reaction products.

Kinematically complete experiment with five fold differential cross-section for double ionisation of helium by fast ion impact was successfully done [Bap99, Bap00]. In these experiments the momentum transferred by the projectile to the target was determined. In another series of experiments, fully differential cross-section for double ionisation of helium by photon and electron impact was determined with a better accuracy and higher efficiency than that achieved by conventional $(\gamma, 2e)$ and $(e, 3e)$ experiments [Spi95, Spi96, Spi96, Dor96]. Moreover, state-selective scattering-angle-dependent studies of single and double-electron capture into different shells of the projectile at medium velocities were performed [Mer95a, Kam95, Cas96].

Initially momentum spectroscopy technique was used to study atomic reactions only. At the turn of the century the technique has come to be exploited for studying molecular reactions [Sie00, Bak01, Jan02, Sie02a, Red03, Tak05]. It has become a powerful tool to investigate the dissociation dynamics of unstable molecular ions. Due to the high detection efficiency for momentum resolved detection of all particles, and the ability to record several particles in rapid succession, momentum spectroscopy is well suited for multi-ion coincidence measurement of products of molecular dissociation. The power of the technique to study molecular dissociation dynamics is described at length in the coming chapters. Other than momentum spectroscopy, velocity map imaging (VMI) has also been used quite extensively for momentum resolved measurements. In this technique all ions with a given velocity produced in the interaction volume are mapped onto the same radius on a two-dimensional position sensitive detector. The limitation of this technique is that it requires time-slicing of the events to obtain the momentum distribution and hence samples only part of the momentum space at a time. Two comprehensive reviews on the momentum imaging methods and applications are [Ull03b, Par03].

1.4 Motivation and outline of the work

Multiply charged molecular ions play an important role in understanding the chemistry of the atmospheres of astrophysical objects. Molecular ions, for example H_3^+ , H_3O^+ , CO^+ , H_2O^+ etc., have been observed in many stars [Dal76, Man80, Ban04]. The quantitative understanding of the energetics and reaction dynamics of multiply charged ions may be relevant for technological development in different fields such as hot plasmas (fusion devices), laboratory discharges, or high intensity ion sources. They play a significant role in the chemistry of the upper atmosphere and of interstellar space [Asc03, Mai03]. These reasons and the fundamental aspects related to molecular ions have attracted increasing attention of physicists and chemists.

In the gas phase, multiply charged molecular ions exhibit a different behaviour compared to the well-known solution chemistry of metal multiply charged ions [Asc03, Qay04, Lev05a]. Very little is known about these multiply charged molecules, primarily due to their instability. The PES of multiply charged molecular ions often have unusual features. These features are due to the competition between the repulsive Coulomb interaction, and the attractive terms generated by chemical bonding and charge induced dipole interactions [Lev05a]. When repulsion dominates, the so-called “Coulomb explosion” leads to a separation of the charges accompanied by bond breaking. The internal energy stored in the molecular ion is converted into kinetic energy of fragments. The information about the lifetime, bond angle, electronically excited energy levels etc. of multiply charged molecular ions is carried by the fragments.

Measuring the complete momentum of all fragments is thus a tool to extract information about unstable molecular ions. We can image a complete snapshot of the molecular ion breakup process by measuring the correlated momentum vectors of all collision products. Such measurements will not only provide information about the charge states and potential energy surfaces but also shed light on the mechanism and dynamics of their excitation, ionisation and fragmentation process. The angular correlation between momentum vectors may

tell us about the geometry of the fragmenting molecular ion. This motivated us to investigate dissociation dynamics of unstable molecular ions, or precursors, by momentum spectroscopy of fragments.

For the present study molecular ions were created by high energy electron impact on free molecules. The energy is high enough to ensure that the break-up is purely unimolecular and is not influenced by the properties of the projectile or by post-collision interaction with the projectile. Questions such as – is the geometry of the dissociating molecular ion same as that of neutral molecule? which bond breaks preferentially and what is its probability? is there any preferential decay channel of dissociating molecular ion? which electronically excited energy levels are involved in a break-up? – were attempted.

To carry out these studies we built a multi-particle momentum spectrometer. The next two chapters describe the experimental set-up used for multi-hit coincidence study of different fragment ions produced in a collision. The set-up was first tested with an atomic gas (Argon) and later on triatomic and polyatomic molecules were studied. The linear triatomic molecule, CO_2 , was studied quite extensively. The study on CO_2 is described in fourth chapter. The fifth chapter deals with the fragmentation of polyatomic molecules having a high order of symmetry, viz. CCl_4 and SF_6 . We observed migration of atoms during dissociative ionisation of these molecules, and determined the altered geometry in case of CCl_4^{2+} . The sixth chapter concerns site specificity in dissociative ionisation. A large scale rearrangement of atoms is observed in the dissociation alcohols. An attempt is made to determine the site specificity in the break-up and formation of bonds of that molecule. The seventh chapter summarises the work done and the inferences drawn from the study.

Chapter 2

The Ion Momentum Spectrometer

2.1 Requirements

For the work reported in this thesis many different aspects of dissociation of molecules were studied in order to understand the dynamics of the process. To pursue the study we designed and built a momentum spectrometer. The primary requirement of the experiment is to detect and identify ions which are formed in collision regions and measure their complete momentum vectors. The combination of a TOF mass spectrometer and an imaging detector permits us to identify the ions and to measure their momentum vectors. The TOF is measured with respect to a trigger signal which defines the instant of interaction between target and projectile. To obtain the trigger, a pulsed projectile beam is often used. However, the interaction itself provides a trigger for ion flight time measurement in the form of the ejected electron, provided the electron is detected nearly instantaneously. Since our projectile beam is not pulsed, we use the ejected electron as the trigger to start the ion flight time measurement. The TOF of an ion depends not only on its m/q ratio but also on its momentum along the flight axis (which we call the z axis). To extract the momenta transverse to the z -axis, we use a large area imaging detector which records the position (x, y) of arrival of the ion on the detector placed perpendicular to the TOF axis. This (x, y, t) information for each ion is recorded and stored in an event list. The three momentum components

(p_x, p_y, p_z) of each ion are reconstructed event-by-event.

This chapter describes the apparatus and the efforts put in to bring it up to its optimum performance. The performance of spectrometer was tested with argon gas, the results of which are discussed at the end of the chapter.

2.2 The experimental set-up

The momentum spectrometer is housed in a stainless steel vacuum chamber of diameter 300 mm and height 570 mm. It has eight ports in one plane for arranging the electron gun, the gas jet, the faraday cup and a provision for admitting a laser beam. All ports are metal gasket sealed. The chamber is pumped by a single 520 lit/sec turbomolecular pump backed by a dry scroll pump. The ultimate pressure, achieved after bakeout, is 5×10^{-9} mbar. The components of the spectrometer are described below.

2.2.1 Collision geometry

Two considerations are important in creating the source of ions for a momentum spectrometer. The first is that the target should be internally cold, and the second is that the reaction volume should be well localised. The well localised reaction volume is achieved by having a projectile–target crossed beams geometry. The cold target is achieved by supersonic expansion of the gas. However, it is not possible to generate a supersonic beam of all gases or liquids. A supersonic beam is not a must if the momenta to be measured are sufficiently larger than the thermal spread of the target molecules. In our set-up we use an effusive beam produced by a capillary of inner diameter 0.15 mm and length 12 mm. A target number density at the exit of the capillary is about 10^{13} cm^{-3} .

Ionisation of the target is carried out by electron impact. An electron beam is produced by an electron gun of electrostatic design. Its electron source is an indirectly heated cathode. The energy of the electrons can be varied over the range 600–1900 eV. The gun uses an Einzel lens for focusing the beam and electrostatic deflectors for steering it. The gun is 200 mm long. The focal length can be varied

over 250–300 mm. The focal spot of the beam is about 0.5–0.8 mm. A 80 mm deep Faraday cup biased at +30 V is used to collect the electrons. The ionisation volume is about 3 mm³.

2.2.2 Extraction of reaction products

One of the key aspects of the momentum spectroscopic technique is the homogeneity over a large volume, of the electric field used for extraction of ions from the reaction volume. There are various methods of creating a homogeneous extraction field. One of the methods consists of uniformly winding a carbon fibre around four germanium coated isolator rods with a gap along the length of the rods. A voltage applied along the fibre is distributed according to the resistance of the fibre [Mer95a]. Another arrangement uses a pair of large plates with a resistive coating. A voltage can be applied to the edges of the plates, creating a uniform field *along* the length of the plate. In the present apparatus, we achieve this by co-axially stacking 12 thin aluminium rings, equally spaced, in a potential divider arrangement.

The outer and inner diameters of the 2 mm thick rings are 200 mm and 100 mm, respectively. Figure 2.1 shows the details of the spectrometer. The dashed line shows the plane of interaction of projectile beam and target beam. Counting away from this central plane, the top rings are labeled $t_1 \dots t_6$ and the bottom rings are labeled $b_1 \dots b_6$. The distance between the two consecutive rings are 20 mm. The distance between the topmost, t_6 , and bottommost, b_6 , rings is 220 mm. The b_2 ring (30 mm below the central plane) and the t_6 ring (110 mm above the central plane) have high transmission meshes on them, creating a uniform field over a cylindrical volume of 100 mm diameter and 140 mm height (See Figure 2.1). The transmission coefficient of the wire mesh is about 95%. Immediately above the t_6 ring is the drift region for ions, defined by a 100 mm diameter tube terminated at the top by a high transmission wire mesh and held at the same potential as the t_6 ring. The length of the drift tube is 220 mm, following the Wiley-McLaren condition ($d = 2s$) which nullifies the effect of the spatial spread of the reaction volume on the TOF resolution [Wil55]. The nullification is impor-

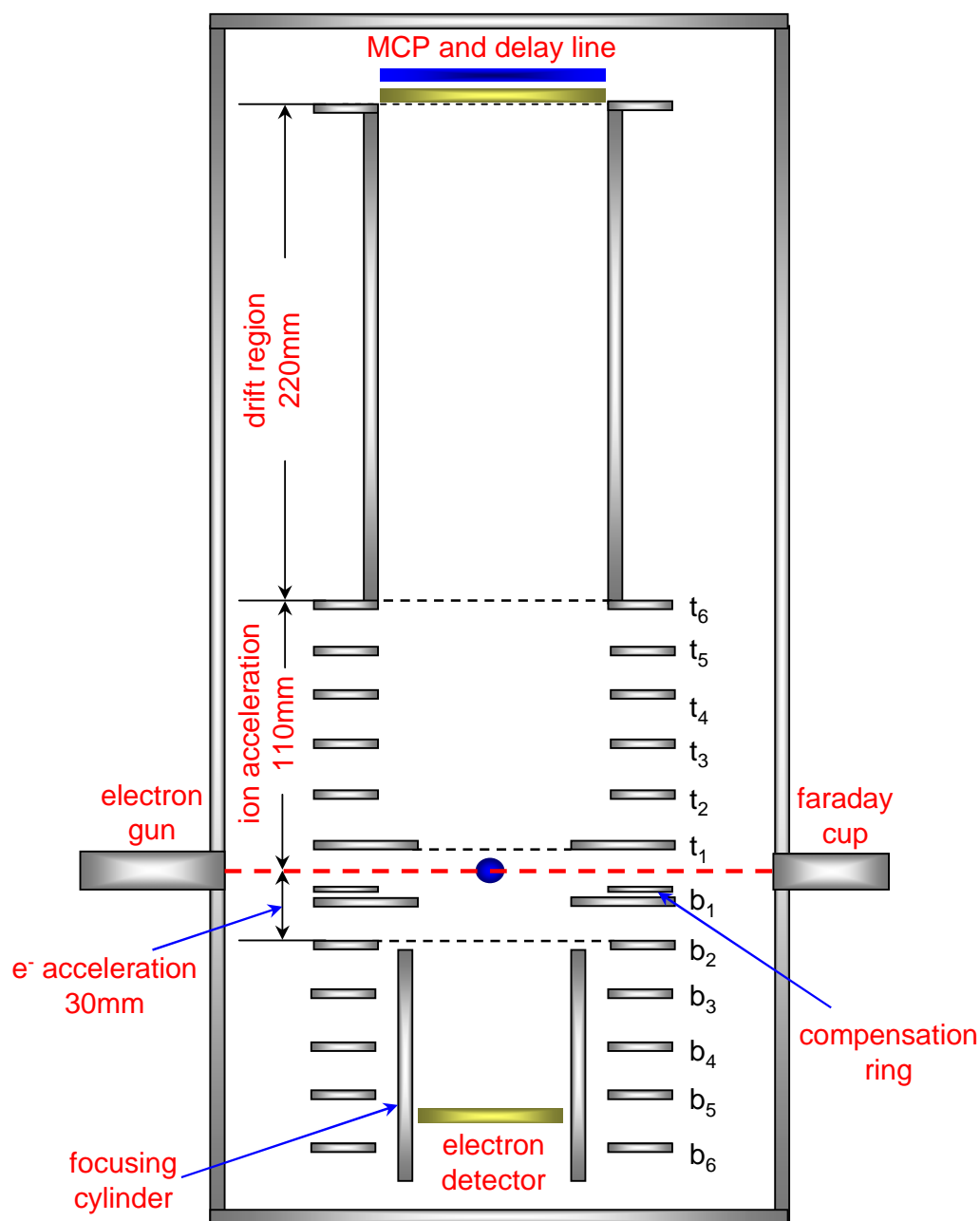


Figure 2.1: Schematic of the momentum spectrometer built for studying molecular fragmentation. The stack of rings for field generation is clearly seen. The red thick horizontal dashed line indicates the plane of the e-beam and molecular beam. The blue circle at the centre of the chamber represents the interaction region. The black dashed lines represent the meshes on plates b_2 , t_1 and t_6 .

tant, because a practical reaction volume is not point-like. An extended reaction volume has two problems. First, the ions start at different potentials. Second, the ions travel different distances during acceleration. These cause a spread in flight times for ions of same mass and initial momentum. Hence, a momentum spectrometer with an acceleration region alone, but no field free drift region is not as good as one with a field free region. A commonly used design for a TOF spectrometer has two successive acceleration stages and a drift region to improve the mass resolution. However, it destroys the information about the initial momentum of ions.

The potential divider arrangement comprises a resistor chain. The resistors are 200 k Ω each and have a low temperature coefficient and tight nominal value tolerance. The measured values of the potentials on the rings deviate less than 0.05% of the notional values. The uniformity of the electric field E , as estimated by computer simulation, is better than 1 in 10^3 . The central plane of the stack is at zero potential, and the electron and molecular beams lie and intersect in this plane. The overlap volume is quite well centred in the extraction volume. The extraction field accelerates the ions vertically upwards and the electrons downwards. The field strength can be varied from 15 V/cm to 90 V/cm. This field is much stronger than that employed in momentum spectrometers for atomic collisions (typically 5 V/cm), thereby leading to a poorer momentum resolution. However, strong fields are essential here, in order to collect the energetic dissociating fragments.

2.2.3 Electron detector

The electron detector is a 40 mm diameter MCP which is 40 mm away from the interaction region (10 mm below the b_2 plate). An MCP has several million channels and each channel works as an independent electron multiplier. The inner surface of each channel is coated with a semiconducting material, which serves as a secondary electron multiplier. Energetic electrons entering a channel release secondary electrons from the wall of the channel (see Figure 2.2). The secondary electrons are accelerated by an electric field developed by a voltage ap-

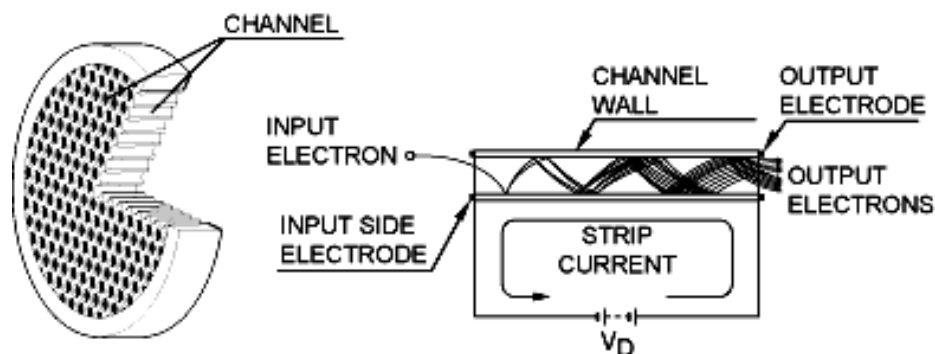


Figure 2.2: Operation principle of an MCP. Charged particles hitting the surface of the MCP generate secondary electrons which are accelerated by the applied voltage V_D . These secondary electrons then again strike the channel surface and produce more electrons, creating a charge cloud.

plied across both the ends of the MCP. They travel along parabolic trajectories until they in turn strike the channel surface again, thus producing more secondary electrons. Successive strikes yield a cloud of around 10^7 – 10^8 electrons, which emerges from the rear of the MCP. It is advantageous to stack together two or three MCP (called Chevron or Z-stack configurations, respectively) to get better performance, due to increased gain. Under appropriately applied voltages the detection efficiency for charged particles is about 60%.

2.2.4 Ion imaging detector

For any imaging experiment a large area position sensitive detector is a must. For charged particle imaging, the first stage of the detector comprises a MCP. Position encoding is achieved in the second stage, where a coordinate is assigned to the centroid of the electron cloud emerging from the back of the MCP. Three popular methods are the charged coupled device, the wedge and strip anode and the delay-line anode. The principles of these imaging devices are discussed below.

Charged coupled device camera

The charged coupled device (CCD) camera is the simplest of the three methods mentioned. In this method, the electron cloud created by the MCP falls on a semi-transparent phosphor screen where it is transformed into a localised photon shower. This light is then imaged on a CCD camera. Such a system has a utility in direct determination of the position of particle impact. However, due to the slow electronic readout of the optical image, it is not very useful for obtaining timing information or rapid readouts.

Wedge and Strip detector

The wedge and strip detector was a revolution in the field of charged particle imaging. The working principle of the wedge and strip detector is as follows. The wedge and strip anode consists of a base germanium layer, on which three repetitive metallic structures are etched. These anode structures are ‘wedge’ (W), ‘strip’ (S) and ‘meander’ (M) (see Figure 2.3). This pattern is made so that the electron cloud will hit all three structures or electrodes. Thus the charge will spread over all three electrodes. From the relative fractions of the charge arriving on each of the electrodes the center of gravity of the electron cloud can be estimated [Kay88] by the following expressions:

$$x \propto \frac{Q_S}{Q_S + Q_W + Q_M}, \quad y \propto \frac{Q_W}{Q_S + Q_W + Q_M} \quad (2.1)$$

Here, Q_W , Q_S and Q_M are the amount of charge collected by the wedges, the stripes and the meander, respectively. The position resolution depends on the charge collection efficiency, and hence longer charge integration times are required to achieve good resolution. At the expense of count rate, a wedge and strip detector can offer resolution as good as 0.1 mm.

Delay line anode

The delay-line is a bare copper wire wound across opposite edges of an insulating plate. Two crossed pairs of delay lines, isolated from one another, give a 2-D

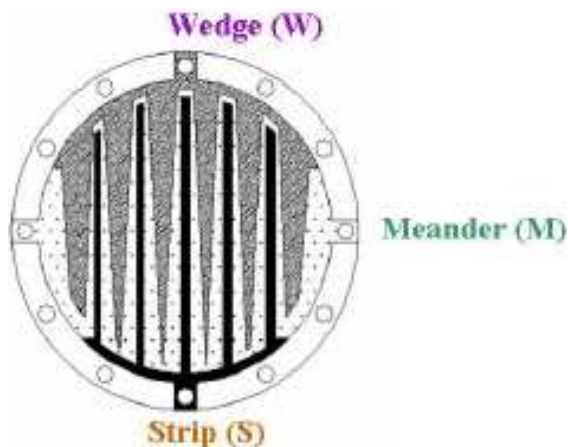


Figure 2.3: *The Wedge and Strip detector.*

grid as shown in Figure 2.4. The details of the position encoding can be found in [Jag98, Roent]. An electron shower (from the back of the MCP) on this grid causes image charge pulses to travel to the ends of the wires, giving four pulses for each particle hit. The signals from the MCP as well as the delay line anode are fed to preamplifiers with a gain between 50–100, and are constant fraction discriminated to generate NIM standard timing pulses. The signal from the primary electron shower of the MCP is used to time the ion arrival. The time difference between the signals arriving at ends of the delay-line is proportional to the distance of the the electron shower from the mid-point of the delay-line. For a crossed pair of delay lines, which form the x and y grid, the position is derived from the time differences between the pairs of pulses reaching the ends of the two delay lines:

$$x = (t_{x1} - t_{x2}) v_{\text{signal}}, \quad y = (t_{y1} - t_{y2}) v_{\text{signal}} \quad (2.2)$$

Here v_{signal} is the pulse propagation velocity along the delay-line, which is almost equal to the speed of light.

Since the propagation time from one end of a delay-line to the other is a constant, the quantities $t_{x1} + t_{x2}$ and $t_{y1} + t_{y2}$ are constants for a given delay-line. These sums can be used as a consistency test for genuine signals. The relevance of time sum will be clarified later.

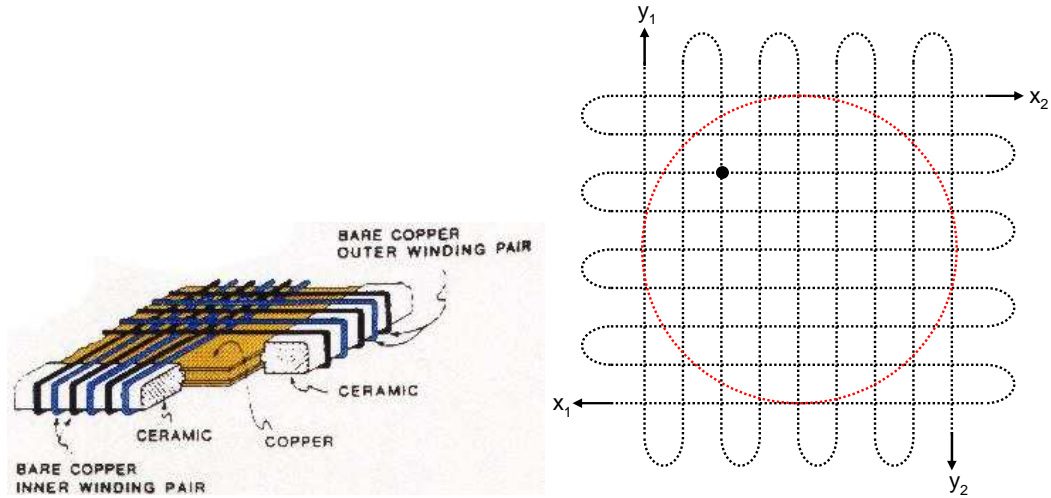


Figure 2.4: [Left] Detail of a helical wire delay-line anode (DLD). [Right] Operation principle of delay-line anode. The red circle defines the boundary of the MCP. Secondary electron from MCP are accelerated towards the DLD. Every event generates four signals on DLD. One at every end of the orthogonal delay lines: x_1 , x_2 , y_1 and y_2 . Position x and y is then calculated by $x_1 - x_2$ and $y_1 - y_2$

Selection of anode

Momentum spectroscopy requires a large area position sensitive detector with good position resolution and fast timing signals. In most applications the delay-line anode is superior to the wedge and strip detector. The biggest advantage is very fast readout allowing a count rate of about 1 MHz. Another advantage is that large area delay-line anodes can be made without any loss of position resolution where as the wedge and strip detector results in proportional reduction of the resolution. Thus, we have chosen for our spectrometer a chevron configuration MCP with a delay-line anode. It has an active diameter of 76 mm. Its position resolution is $250 \mu\text{m}$ and the time resolution is 1 ns.

2.3 Optimisation of spectrometer performance

The performance of the momentum spectrometer was optimised for proper overlap of the electron beam with the gas beam and for signal processing. The details are described below.

2.3.1 Projectile-target overlap

The electron gun is mounted on one of the eight cross ports of the chamber. The gun is shielded from external electric and magnetic fields by enclosing it within a grounded mu-metal sleeve. The electron beam can be swept in the transverse direction by electrostatic deflectors. At the focal spot the sweep is about ± 20 mm. The focal length can also be varied between 150–200 mm from the exit aperture. Coarse tuning of the beam is done by observing the beam spot on a fluorescent screen, and fine tuning is done on the basis of the TOF and position spectra. An atomic gas (eg. Argon) is used for this purpose, so that there is a negligible momentum width of the ions. It is important to ensure that the overlap of the electron beam and the molecular beam occurs within about 0.5 mm of the axis of the spectrometer in order to obtain high coincidence efficiency. The position of the overlap along the extraction axis is equally critical, in order to meet the time-focus condition, $d = 2s$. The drift tube was designed in such a way that its length could be altered by a few mm. By several trials, with minor variations in the tube length the condition $d = 2s$ was met. The parallelity of the stack plates and the drift tube is also well taken care of in the present set-up by appropriate designing and precision machining of the stack and drift tube structure. The measured imperfection is 0.2 mm in 330 mm.

The electron beam suffers a deviation as it traverses normal to the extraction field. A 1300 eV beam suffers a deviation of 4–24 mm at the target, for extraction fields between 15–90 V/cm. Even with the extraction field on, it is possible to position the beam on the target, by changing its entry angle. However, this leads to a large number of secondary electrons due to the beam grazing the extraction ring. These secondary electrons increase the electron background count and affect the

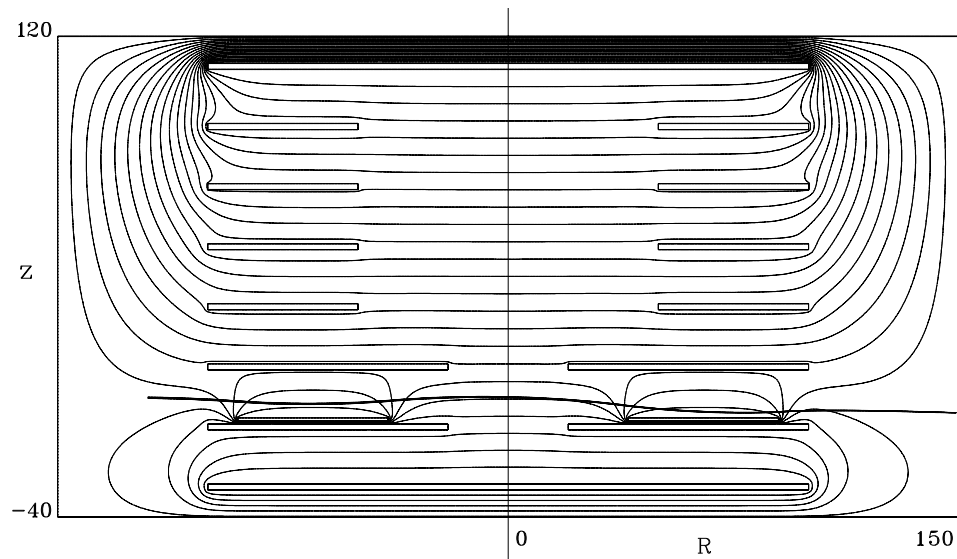


Figure 2.5: Trajectory of a 1300 eV electron beam through the extraction stack with the compensation ring and the modified t_1 and b_1 extraction rings with smaller inner diameters. The extraction field is 60 V/cm, and the compensation ring produces an opposing field of approximately the same magnitude. Distances are in mm. The trajectory simulation calculations were done using the TRICOMP software.

quality of the spectrum. Furthermore, the beam is not properly collected by the Faraday cup. To get around these problems, we have introduced a ring electrode (named compensation plate), which partially compensates for the effect of the extraction field on the e-beam. This ring has inner diameter 80 mm and outer diameter 190 mm, and is placed between the central plane and the b_1 ring. It provides an upward acceleration to the e-beam twice during its transit through the spectrometer. By tuning voltage on the compensation plate and the beam entry angle, it becomes possible to transport the beam without loss to the Faraday cup, while simultaneously intersecting the gas beam, as seen from a computer simulation (Figure 2.5). To minimise the distortion of the extraction field due to the compensation field, the inner diameter of the t_1 and b_1 stack rings is reduced to 40 mm. The uniformity of the extraction field around the ionisation volume

remains unaltered to within 1%, while the effective open area for transport of ions remains unchanged. Introduction of compensation plate reduced the electron background count rate. Before the introduction of the compensation plate the electron count rate was about 10 times the ion count rate. The compensation plate reduced this to about 3 times, besides making it possible to measure the transported electron beam current.

2.3.2 Signal processing

Ion signals

To detect all ions with equal efficiency it is necessary to operate the detector at saturation (i.e. constant gain region). The detection efficiency of the detector is proportional to the impact velocity of the detected particle [Sav95]. Hence, for a given channel plate voltage ions having small m/q are more likely to be detected than those having large m/q . We determined the voltage at which the detector efficiency was equal for all ions of interest. To do this, the ratio $\text{Ar}^+/\text{Ar}^{2+}$ of ions arising from ionisation of argon was studied as a function of the voltage on front face of the MCP while keeping a fixed potential difference across the plates. We found that ratio did not change beyond -3600 V front face voltage.

However, during most of the runs we fixed the bias on the front channel plate at -2800 V, because at some stage we noticed that a higher voltage increased the background ion counts drastically. This may have been due to a small discharge near the MCP, which could have caused irreparable damage to the detector. Since most of our results do not pertain to absolute intensity measurements, the application of -2800 V does not affect our analysis. The timing pulse from the MCP has a width of 1 ns and an amplitude of 20 mV.

To extract the signal from the delay-line anode, it should be operated at positive potential relative to the potential on the MCP back. While optimising the voltages we kept a fixed potential difference between MCP back and delay-line anode and operated at the factory prescribed potential difference of 250 V.

A dedicated signal extraction unit is supplied by the manufacturers of the

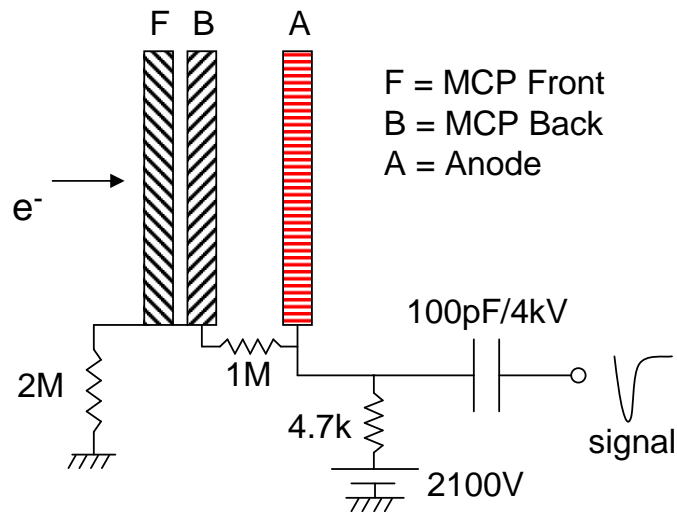


Figure 2.6: Schematic of the biasing of the channelplate for electron detection in the present set-up. For positive ion detection, the voltage on the front face of the channelplate is negative, while the back is grounded through a resistor and the anode is maintained at a positive potential.

delay-line detector. Within this unit the primary signal from the MCP and four signals from the delay lines are processed through a RC network. The drawn out signal cannot be observed directly, but can be observed after the amplification stage. The factory gain setting (about 80) was not disturbed during the course of the experiment. The amplified signal goes to built-in CFDs which give out NIM standard logic pulses. The five NIM outputs were then fed to a multi-channel time to digital convertor (TDC).

Electron signals

The connections of the electron detector are shown in Figure 2.6. The anode is maintained at 2100 V and this voltage is distributed on the front and back channel plates in accordance with the biasing resistance and the intrinsic resistance of the plates. The resistance across the front and back face of the channel plates is 120 M Ω . The potential on the front and back MCP can be calculated, which comes out to be 35 V and 2080 V, respectively.

The signal from electron channel plate was drawn out through a capacitor and dropped across a resistor and was amplified by a preamplifier. The gain of the amplifier was 100. The amplified signal was then fed to a constant fraction discriminator (CFD) and then the NIM output from the CFD was fed to START of the TDC.

One hurdle encountered during the set-up was due to face to face positioning of the electron and the ion MCPs with a large electric field between them. This caused a stray flow of ions from the electron MCP to the ion MCP, distorting the image on the ion detector. To minimise this effect the electron MCP was moved away from the reaction volume, and a weak barrier potential was arranged near the electron MCP to suppress ion feedback. With the increased distance, electron focusing became necessary, which was achieved by introducing a grounded cylinder as shown in Fig. 2.1. The focusing cylinder also reduced stray electron pick-ups. Electron trajectory simulations showed that upto 22 eV electrons were collected with 100% efficiency.

2.4 List Mode Data Acquisition

Data acquisition for the momentum spectrometer is based on six timing signals: one from the electron MCP, one from the ion MCP and four from the delay-line. The electron MCP signal serves as a master START for every event, triggering five channels of the TDC (LeCroy 133MTD). The first four channels are stopped by the delay-line signals, giving the ion position. The fifth channel is stopped by the ion MCP signal, giving the ion TOF. The TDC has a 500 ps resolution, and a 32 μ s range. The maximum event rate can be about 1.2 kHz with all channels active. For the present measurements the rate is maintained around 250 Hz as at higher count rates stray coincidences lead to a heavy background. Figure 2.8 shows the sequence of data acquisition.

Digitised outputs of the five channels are read event after event, and stored as a list on a computer disk. The TDC has a PC interface written in the MS Visual C++ language. The program is called CoboldPC, which stands for "Computer Based

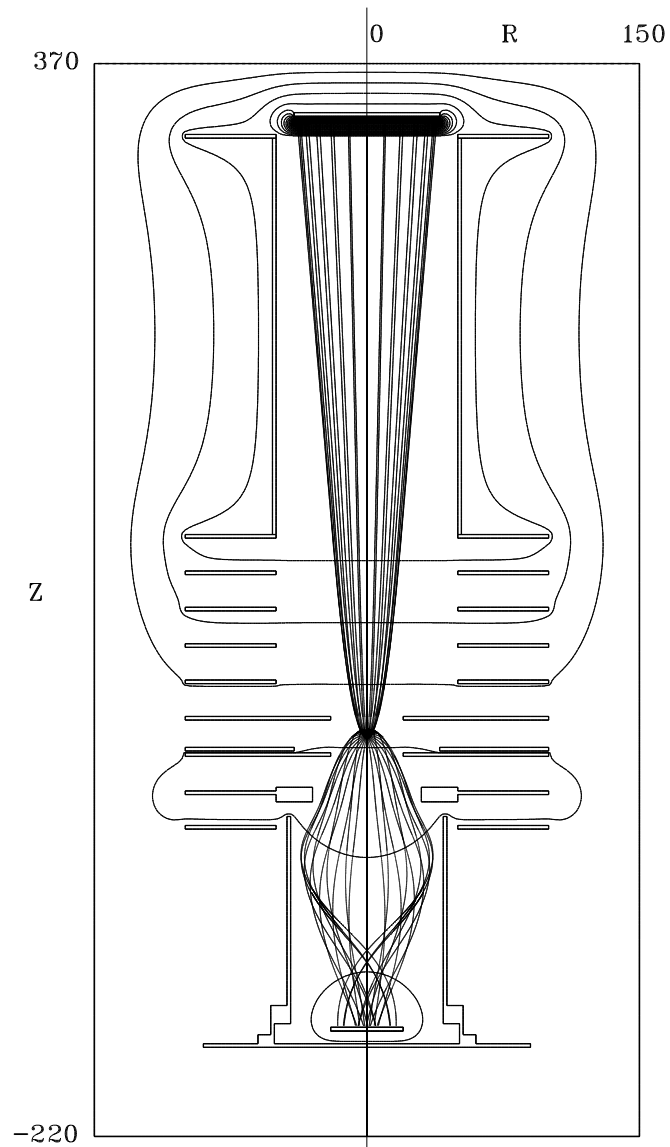


Figure 2.7: Trajectory simulation for the electron and CO^+ from a dissociative ionisation of CO_2 . It shows that electron show that the upto 22 eV electrons are collected completely when the extraction field is 50V/cm whereas CO^+ having energy 11eV energy are collected with 100% efficiency. Simulations were done using the TRICOMP software.

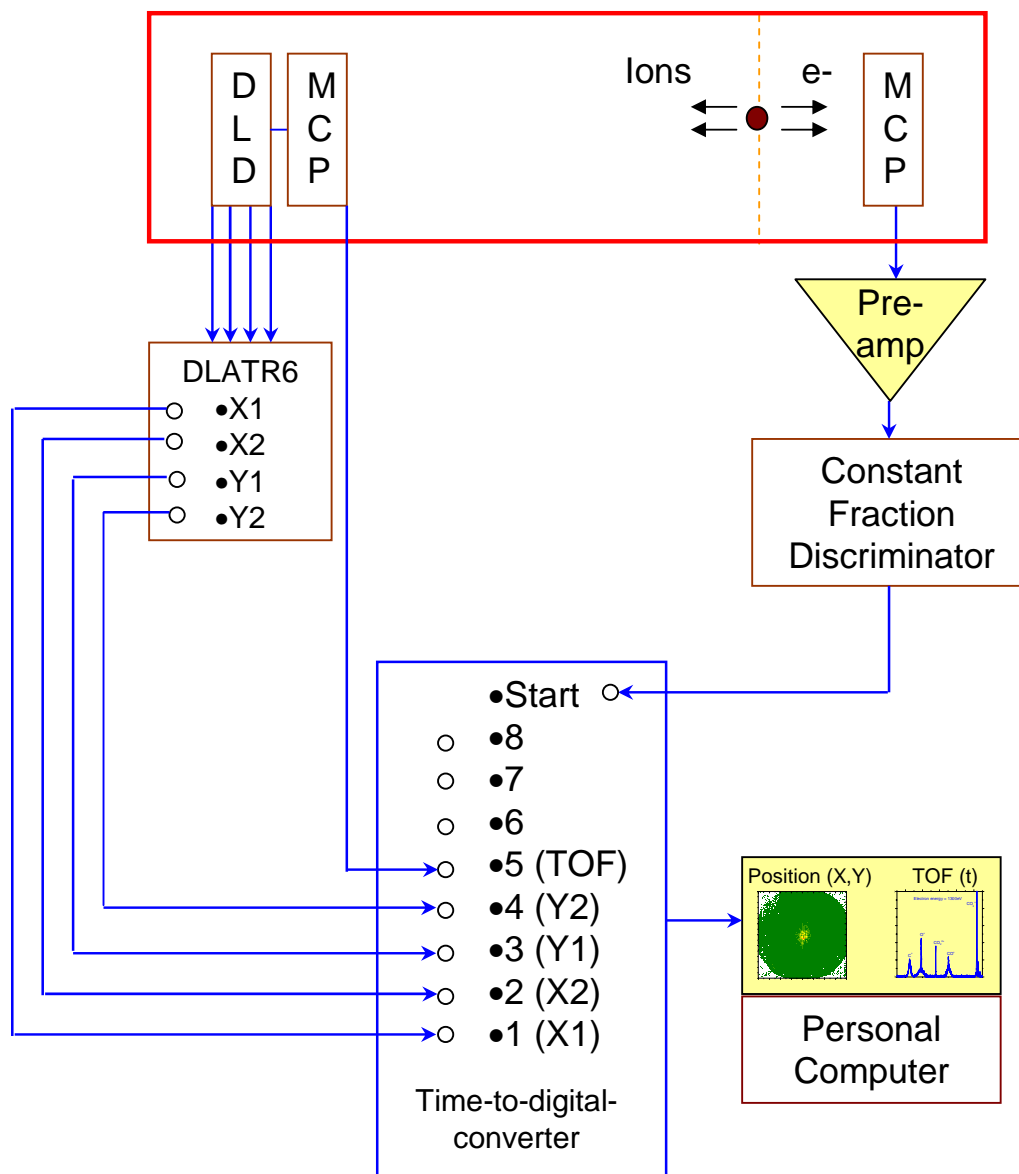


Figure 2.8: Reading out the events. The electron signal serves as the master start for all channels. Channels 1–4 are used to get position information of ions, while channel 5 gives the TOF. The TDC has a computer interface via the CoboldPC program, which reads the events into a list mode file.

Online-offline Listmode Data Analyser". The program writes the events into a list mode file (online data acquisition). The same program is also used to analyse list mode data after acquisition (offline analysis). List mode is a special technique used in collision physics. In this mode all acquired information (named coordinates in CoboldPC) is stored event by event in a data list. The original CoboldPC program is meant for imaging, using the four delay-line signals. The program was modified to accept five inputs so that the vital TOF information could also be recorded simultaneously with the position. The event list adapted to our requirements contains (x_1, x_2, y_1, y_2) and t , entries, obtained from the delay-line anode and the electron-ion coincidence respectively. From these entries we get the x, y position using Eq. 2.2.

The same program can be used to analyse the list mode data after the experiment is over (offline analysis). The primary offline function is the generation of the momentum data from the x, y, t triplet, which is described in detail in the next section. The program is capable of sorting data from several events, performing complex calculations, transformations, conditional sorting, creating new variable from old ones, histogramming events etc. and displaying the processed data.

2.5 Building the ion momentum vector

The TOF of an ion depends on the initial momentum component along the extraction axis, the length of the extraction region, s , the length of drift region, D , and the extraction field, E_s . Let us first see how the TOF of an ion is obtained. Consider an ion that is created in the ionisation region, having charge q , mass m and initial momentum along the extraction axis p_z . The time t_s taken by the ion to reach the field free drift region is given by

$$s = \frac{p_z}{m} t_s + \frac{1}{2} \frac{qE_s}{m} t_s^2. \quad (2.3)$$

Solving Eq. 2.3 gives the TOF in extraction region

$$t_s = \frac{-p_z/m + \sqrt{[p_z/m]^2 + (qE_s/m)s}}{qE_s/m}. \quad (2.4)$$

The time, (t_D), spent by the ion in the drift region is

$$t_D = \frac{D}{\sqrt{[p_z/m]^2 + (qE_s/m)s}}. \quad (2.5)$$

The total time the ion takes to reach the detector is, hence, given by

$$t = t_s + t_D = \frac{-(p_z/m) + \sqrt{[p_z/m]^2 + (qE_s/m)s}}{qE_s/m} + \frac{D}{\sqrt{[p_z/m]^2 + (qE_s/m)s}}. \quad (2.6)$$

Setting the Wiley-McLaren condition $2s = D$ gives

$$t = \sqrt{2m} \left[\frac{-p_z/\sqrt{2m} + \sqrt{p_z^2/2m + qsE_s}}{qE_s} + \frac{s}{\sqrt{p_z^2/2m + qsE_s}} \right]. \quad (2.7)$$

The TOF, t_0 , for ions which have zero initial energy is given by

$$t_0 = \sqrt{2m} \left[\frac{\sqrt{qsE_s}}{qE_s} + \frac{s}{\sqrt{qsE_s}} \right]. \quad (2.8)$$

Cases in which $(p_z^2/2m) \ll qsE_s$, the difference between the flight times of zero energy and non-zero initial velocity ions can be written in a simplified. The condition is well satisfied in our spectrometer. Combining Equations 2.7 and 2.8, we get

$$p_z = qE_s(t - t_0). \quad (2.9)$$

Once the TOF (t) and the position (x, y) is obtained, the momentum vector of each registered ion can be derived. The momentum components parallel to detector plane and perpendicular to the TOF axis are given by following expressions:

$$p_x = m \times (x - x_0) / t, \quad (2.10)$$

$$p_y = m \times (y - y_0) / t, \quad (2.11)$$

where (x_0, y_0) is the centroid of the interaction volume projected on the detector plane.

The first condition to be satisfied by the recorded events for consideration for momentum analysis is the time sum condition explained in Sec. 2.2.4. Only those events which satisfy this condition carry complete time and position information. Other events, which form about 10% of the total, are ignored during offline analysis.

The next step towards extracting momentum values is the identification of the ion species, and the $p_z = 0$ point in the TOF spectrum for each species. To this end, the TOF spectrum of an atomic gas like Argon is recorded. The mean positions of the Ar^+ , Ar^{2+} and Ar^{3+} TOF peaks are taken to be $p_z = 0$ points for the respective ion species. A linear fit of these TOF points to $(m/q)^{1/2}$ provides the m/q calibration and $p_z = 0$ position for *all* ion species. As the final step, we set a window demarcating the TOF distribution of the ion of interest and transform the (t, x, y) values to (p_z, p_x, p_y) . This exercise is carried out for each recorded ion species.

2.6 Test results

We first look into the momentum resolution of our instrument. Throughout this thesis, atomic units are used for momenta. One a.u. of momentum is the RMS momentum of an electron in the ground state of the H-atom, in units of $|e| = m_e = \hbar = 1$, $c = 1/\alpha$, and equals 2.04×10^{24} kgm/s.

The limit on the momentum resolution imposed by the spatial resolution of the detector is

$$\Delta p_{x,y} = m\Delta x/t, m\Delta y/t \quad (2.12)$$

where Δx (or Δy) is the position resolution of the detector, which is 0.25 mm. We find $\Delta p_{x,y} = 2.1$ a.u. for Ar^+ . The detector imposed limit on the p_z resolution is

$$\Delta p_z = qE_s\Delta t \quad (2.13)$$

This comes out to be 0.3 a.u., based on a 1 ns timing resolution.

Another related quantity is the upper limit on mass resolution based on the TOF spectrometer design, as defined by Wiley and McLaren. Based on a source extent (Δs) of 2 mm and an extraction length s of 110 mm, this value is

$$M/\Delta M = 16[s/\Delta s]^2 = 48400$$

The secondary estimate of $M/\Delta M$ based on the initial kinetic energy width of the ions is not relevant to the present spectrometer, as its primary purpose is to

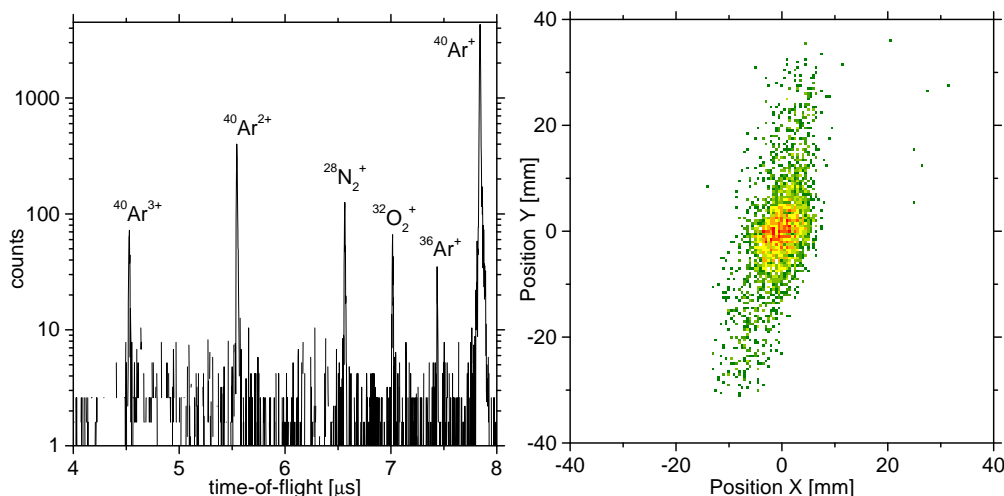


Figure 2.9: [Left] TOF mass spectrum of ions arising from 1300 eV electron-impact on Ar. [Right] Position spectra of Ar^+ ion arising from 1300 eV electron-impact on Ar, obtained by filtering of raw data. The intense red spot close to the centre is a projection of the overlap of the gas beam and the electron beam on the detector plane.

measure the initial kinetic energy itself.

The momentum resolution finally achieved depends on additional factors, such as the thermal spread of the target, spatial extent of the reaction volume, non-uniformity of the fields and deviation of the reaction volume from the mid-plane of the spectrometer. To estimate this, we perform an analysis of the spectrum obtained for an atomic target, such as Argon. All results discussed here are for 1300 eV electron energy and 60 V/cm extraction field. The gas used here has 99.95% purity. The peaks corresponding to N_2 and O_2 mass are due to air contamination in the gas line itself, but they do not affect the present analysis.

Figure 2.9 shows a TOF spectrum of ions arising from ionisation of Ar. The width of the Ar^+ peak may essentially be taken to be the limit of mass resolution and p_z resolution. The FWHM of the Ar^+ TOF peak is 9 ns, while the modal TOF is 7842 ns. This gives a mass resolution $M/\Delta M = 436$.

Figure 2.9 shows the x - y position spectra of Ar^+ ion. The standard deviations of x and y distributions are found to be 2.1 mm and 3.4 mm respectively. σ_y

is larger, because the ionising electron beam runs parallel to the y axis and thus ions are formed over a broader range of the y coordinate than of the x coordinate. These standard deviations translate to $\sigma_{p_x} = 9.5$ a.u. and $\sigma_{p_y} = 10.2$ a.u. The standard deviation of the p_z distribution of Ar^+ is found to be 2.4 a.u. The scalar momentum resolution $[\sigma_{p_x}^2 + \sigma_{p_y}^2 + \sigma_{p_z}^2]^{0.5}$ works out to be 14 a.u. Figure 2.10 shows the momentum spectra of the Ar^+ ion.

We note that the momentum spread of Ar atoms at room temperature is 12.4 a.u. It is thus clear, that in the present set-up the achievable resolution is limited by the thermal width of the target and spatial spread (especially along the electron beam direction) of the reaction volume. It should however be noted, that the resolution of the z -component alone is higher, since the effusion of the gas is perpendicular to the z -axis.

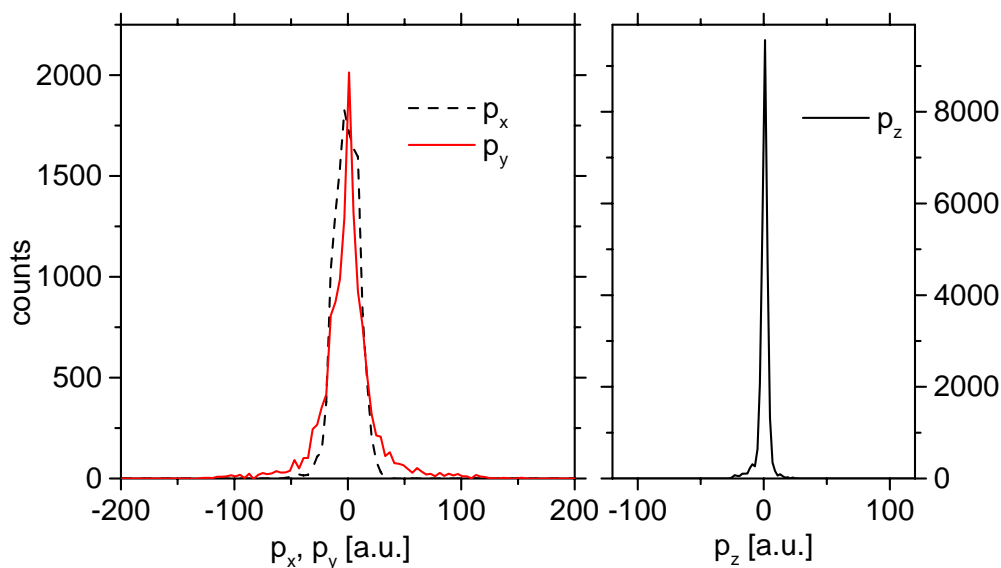


Figure 2.10: Distributions of the p_x , p_y , p_z components of Ar^+ ions.

The resolution thus achieved is adequate for the study of molecular fragmentation, as the energies of the fragments are much larger than the thermal energy of the target. A further consideration in the study of molecular targets is that the number of particles ejected from a single collision can be quite large (depending upon the complexity of the molecule). To study the complete kinematics of

the molecular break-up one needs to detect all fragments from a single event in coincidence. Only then will it be possible to obtain complete kinematics of a break-up. This is possible if detector and the data acquisition system have multi-hit capability. The multi-hit coincidence technique and its power are the subject of the next chapter.

Chapter 3

Multi particle coincidence and momentum maps

The energy transferred to a molecular target may get dispersed in various ways. Besides electronic processes nuclear motion comes into the picture. Nuclear motion manifests itself as vibrations, rotations, bending, stretching of molecular bonds. The time scales of nuclear and electronic motion are very different. Nonetheless, if several electrons are removed in a collision, the response of the residual multiply charged molecular ion can be quite dramatic. Multiply charged molecular ions are transient species. They fragment on timescales ranging from fs to μ s, leading to the formation of atomic or molecular ions. The transient nature of molecular ions make their study challenging. Studying them by spectroscopic technique is difficult as they cannot be stored in large numbers for long. A line of investigation opens up, if one realises that the information about these transient species is carried by the fragments arising from them. Detecting all fragments in coincidence and measuring their complete momenta is a tool for obtaining various types of information about these molecular ions. The dynamics of fragmentation of triatomic and polyatomic molecules is complex, as compared to diatomic molecules, due to the coupling between additional internal degrees of freedom, i.e. bending, as also due to the presence of several features on their potential energy surfaces (PES). Therefore, the dissociation of triatomic and polyatomic molecular ions holds many surprises and is yet to be understood completely.

Combining the technique of momentum spectroscopy with the multi-ion coincidence technique leads to complete kinematic information and thus helps us to understand the fragmentation dynamics. The combination is known as multi-hit momentum imaging. The combination not only enables us to decipher the decay pathways, but also throws light on the PES of the dissociating molecular ion. When aided by computed PES, complete kinematic data can unravel the dynamics of molecular dissociation. This chapter deals with the technique of multi-hit momentum imaging to study fragmentation dynamics of multiply charged molecular ions and an overview of methods for extracting various physical quantities from the data. We will see how the ion momentum spectroscopy method can be naturally adapted to coincidence measurements, and thereby becomes a powerful tool for studying molecular fragmentation.

3.1 Multi-ion coincidence

Consider a molecule that undergoes dissociative ionisation at time $t = 0$ and is accelerated towards the ion detector. The ejected electron provides a ‘time zero’ marker from which the flight times of the fragment ions are measured. Ions arising from a single break-up will have correlated flight times. Neglecting for the moment the z component of the ion momenta, the TOF of ions is proportional to $\sqrt{m/q}$, and hence the ions will be recorded in a time-ordered sequence at the detector. This forms the basis of the multi-ion coincidence technique and is shown schematically in Figure 3.1.

The only addition we need to the ion momentum spectrometer for implementing the multi-ion coincidence idea is a detector that can record several ions in quick succession without loss in its position resolving capability. In other words, the detector should have a low dead-time without compromising the position resolution. The delay-line anode satisfies these conditions rather well. Naturally, the detector capability has to be complemented by equally capable read out and storage electronics. The DLD80 and the TDC8 form an ideal combination for our study. In the present set of experiments we can observe coinci-

Event number	Ion1	Ion2	Ion3	Ion4
...
101	$(t, x, y)_{101,1}$	–	–	–
102	$(t, x, y)_{102,1}$	$(t, x, y)_{102,2}$	$(t, x, y)_{102,3}$	–
103	$(t, x, y)_{103,1}$	$(t, x, y)_{103,2}$	–	–
104	$(t, x, y)_{104,1}$	–	–	–
105	$(t, x, y)_{105,1}$	$(t, x, y)_{105,2}$	–	–
106	$(t, x, y)_{106,1}$	$(t, x, y)_{106,2}$	$(t, x, y)_{106,3}$	$(t, x, y)_{106,4}$
107	$(t, x, y)_{107,1}$	–	–	–
...

Table 3.1: Schematic of the event list. The position and temporal information of fragment ions resulted from a single fragmentation event are stored in an event list. The event list later on be sorted for analysis once the acquisition is over.

dence rate, one has to keep a moderate count rate. In our case the ion count rate is 500 Hz and the electron count rate is 1200 Hz. The electron-ion coincidence rate is about 300 Hz whereas the electron-ion-ion coincidence rate is 30–50 Hz. Coincidence rates are molecule- and projectile-specific. The numbers reported here are for CO under 1300 eV electron impact.

3.2 Coincidence momentum maps

The primary step towards extracting correlated momenta of fragments is identification of coincident ion pairs. For each ion in the chosen coincident ion pair, we first establish the $p_z = 0$ point in their TOF distribution and determine the extents of the TOF peaks as explained in Section 2.5. We then filter out from the event list those events whose t values fall within the extent of the TOF peak. For these events the three momentum components for each correlated fragment are calculated. The distribution of events as a function of correlated momentum components is histogrammed, forming the ion pair *momentum map*. The

method can be trivially extended to higher order correlations present in a many-body break-up.

From the three momentum components of each fragment ion and multi coincidence information, it is possible to identify dissociation channels, to extract their branching ratios, to obtain the lifetime of metastable precursor ions, to estimate the geometry of highly charged molecular ion precursors, to obtain fragment ion kinetic energy release distributions, which in turn can be related to the energy levels of the precursors, etc. The coincident TOF alone carries information about the dissociation channels of the molecular ions and lifetime of molecular ion if it is metastable. Deeper information can be derived from complete momentum maps.

3.3 Information from TOF coincidences

Ion TOF coincidences laid the foundation of the experimental studies of molecular fragmentation. The first electron-ion-ion coincidence experiment was done in 1986 by Frasinski *et al* [Fra86]. Largely speaking, the molecules studied were triatomics, like NO_2 , CO_2 , SO_2 , OCS , and focused on identification of the break-up channels. Mechanisms leading to the break-up, were proposed, based on shapes and slopes of the correlated TOF distributions. On the basis of the ion pair intensities branching ratios were calculated [Cur85, Mil86, Ela87a, Ruh90, Hsi95]. A few unexpected break-up patterns for multiply charged organic molecules were studied and some evidence for rearrangement of atoms prior to dissociation was found [Ruh90, Rej02, Kri04, Fur05]. Field and Eland applied the electron-ion-ion coincidence technique to deduce for the first time the lifetime of a metastable molecular dication [Fie93].

3.3.1 Dissociation channels

An unstable molecular ion breaks up via various pathways. As an example consider the break-up of dicationic molecular ion (ABC^{2+}). There can be three two-body dissociation channels in which two fragments are ions. Similarly, there can

be three three-body fragmentation channels with two ion fragments.

For each of the ion pairs, the correlated TOF distribution will appear as an island on a t_1, t_2 plot. The position of the centroid of the island corresponds to ions with $p_z = 0$. The size and the shape of the islands depends on the mechanism of formation of the pair. Figure 3.2 is a coincidence map of photoions from CO_2 .

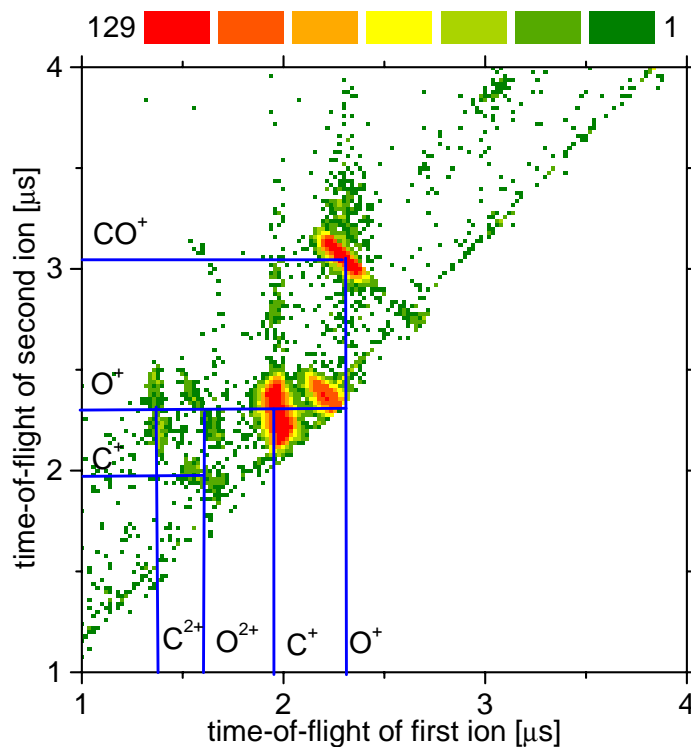


Figure 3.2: Coincidence map of fragments arising from ionisation of CO_2 by 200 eV photons. The prominent ion pairs $\text{C}^+:\text{O}^+$, $\text{O}^+:\text{O}^+$, $\text{O}^+:\text{CO}^+$ arise from the break-up of CO_2^{2+} . The less intense ion pairs $\text{C}^{2+}:\text{O}^+$, $\text{O}^{2+}:\text{O}^+$, $\text{O}^{2+}:\text{C}^+$ arise from the break-up of CO_2^{3+} . The varying shape and slope of each island reflect different break-up mechanisms.

A fragmentation may be classified as one step (concerted) or two step (sequential), based on whether the bonds break simultaneously or one after the other. The sequential process is further classified as initial charge separation (ICS) and deferred charge separation (DCS). In ICS, the breaking of the first bond releases one atomic ion and a diatomic ion. The diatomic ion fragments in the

second step. In DCS, the breaking of the first bond releases a neutral atom and a diatomic cation, which breaks up in the second step. This classification was made by Eland [Ela87b] based on the shapes of the islands in an ion pair coincidence map and the slope of the line fitted to the intensity distribution in the island.

For the one step process, the shape of the distribution is either cigar-like or dumbbell-like. For the two step ICS process, the slope of the best-fit line to the distribution is given by the following expressions (following [Ela91]):

$$\text{slope} = \frac{m_{c^+}}{m_{c^+} + m_A} \text{ or } \frac{m_{c^+} + m_A}{m_A} \quad (3.1)$$

where, m_A is the mass of the undetected neutral fragment and m_C^+ is the mass of the lighter fragment. For decay via DCS, the slope of the best-fit line is

$$\text{slope} = -q_1/q_2 \quad (3.2)$$

where q_1 and q_2 are the charges on the fragment ions.

3.3.2 Lifetime of metastable ions

Multiply charged molecules, if metastable, will break-up into fragments after a delay, as compared to the case of prompt fragmentation. The flight times of fragment ions from a delayed fragmentation will therefore differ from the flight times in case of a prompt dissociation. This will alter the characteristics of the (t_1, t_2) distribution. The lifetime of the precursor ion can be determined from the alterations in the distribution. Generally, lifetimes comparable with the flight times are sampled by this method.

Figure 3.3 is the schematic of the coincidence map [Fie93]. The main island 1 is due to the prompt decay of AB^{2+} . This island has a long tail extending upto the $t_1 = t_2$ diagonal. Apart from the tail, there is a V-shaped structure at the end of the tail. The tail is formed due to the breaking up of the precursor ion in the extraction region at different distances from collision region. The V is due to break-ups in the field free region of the TOF spectrometer. The tail and V are thus indicative of a metastable decay.

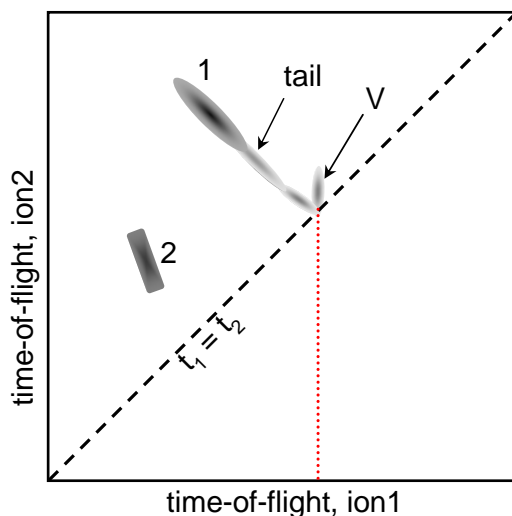


Figure 3.3: Schematic of the ion-ion coincidence map of fragments arising from a break-up. The tail and the V attached to the main coincidence island '1' are due to metastable states of the precursor molecular ion. Island '2' is due the decay of an unstable precursor molecular ion. The dotted line from the apex of the V indicates the TOF of the precursor molecular ion, if it were to remain undissociated.

The lifetime (τ) can be obtained from the counts in the V (I_V) and in the tail (I_{tail}) by following expression:

$$\frac{I_{\text{tail}}}{I_V} = f(\exp(T/2\tau)). \quad (3.3)$$

Here, f is the transmission factor of the spectrometer, which is 90% in our case, and T is the TOF of the stable precursor molecular ion. An application of this method to dicationic CO_2 appears in the next chapter.

3.4 Information from full momentum maps

To unravel information leading to potential energy surfaces of the intermediate multiply charged molecular ion and the geometric structure of the fragmenting system, a full momentum map of all fragments arising from a single break-up is necessary. This is easily accomplished in our experiment, if all fragments are charged. This is also accomplished provided the break-up is unimolecular and

there is only one neutral fragment. This is because in a unimolecular break-up we can determine the momentum of the undetected neutral fragment by the momentum balance in the centre-of-mass frame. We can treat the laboratory frame itself as the centre-of-mass frame, because the momenta of the fragments are much larger than the momenta of the parent molecular and the thermal energies of the parent neutrals. Once the complete momenta of fragment ions and neutrals are deduced, the intermediate geometry of the multiply charged molecular ion and KER during the dissociation is unambiguously determined.

3.4.1 Geometry estimation

Multiply charged molecular ions are expected to favour equilibrium geometries which differ from those of the parent neutral molecule, because of the altered charge distribution. As a consequence of the near equivalence of the laboratory and centre-of-mass reference frames, the relative angles between the fragment momentum vectors can be taken to be the angle between the departing fragments in the molecular ion reference frame. These can be further considered to be the bond angles of the precursor molecular ion (see Figure 3.4). If the momentum vectors of the ions flying apart are \vec{p}_A and \vec{p}_B , then the angle between them is given by

$$\alpha_{A:B} = \cos^{-1} \left[\frac{\vec{p}_A \cdot \vec{p}_B}{|p_A||p_B|} \right]. \quad (3.4)$$

The above analysis can be extended to any pair of fragments from a single event, including ion-neutral pairs, under the conditions previously mentioned. The geometry of the molecular ion at the instant of break-up is determined from these angles. As an example, the angular distribution of fragment ions arising from a three-body break-up of a dicationic water molecule is shown in Figure 3.5.

The momentum vectors of the fragments in a two-body break-up are equal but opposite, and no non-trivial information can be obtained from the angular distributions of such break-ups.

Due to the random orientation of molecules in a free target, it is difficult to obtain the angular distributions of the fragments in the molecular frame of ref-

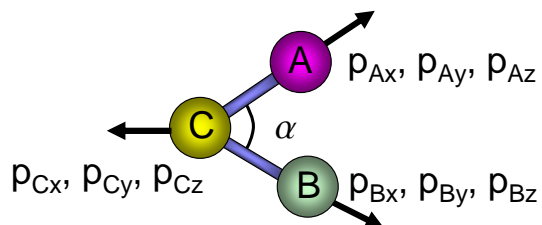


Figure 3.4: Definition of alpha.

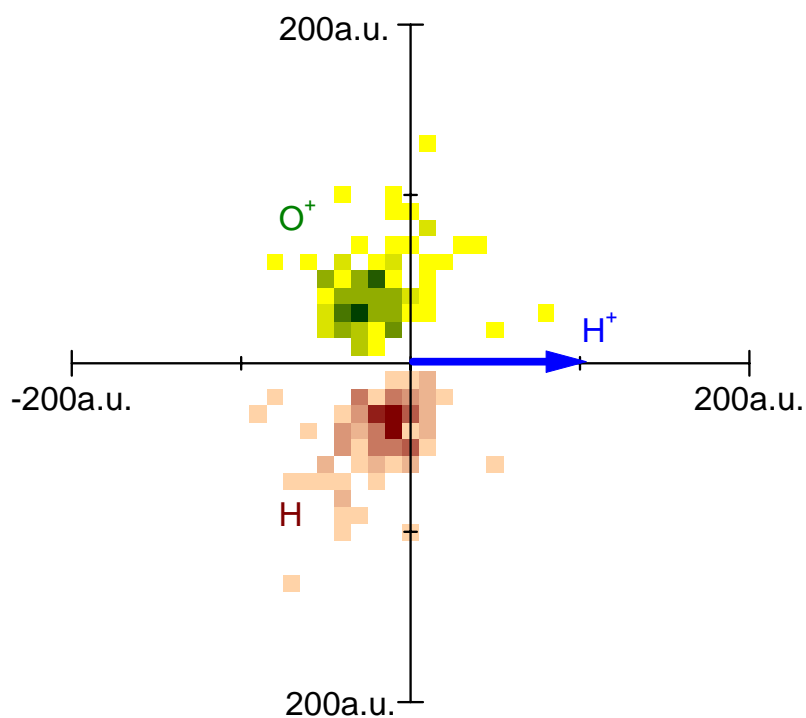
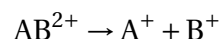


Figure 3.5: Momentum map of all fragments in the break-up $\text{H}_2\text{O}^{2+} \rightarrow \text{H}^+ + \text{O}^+ + \text{H}$. The momentum vector of the first detected ion (H^+) is taken as the reference vector, and the angle made by the momentum vectors of the other two fragments (O^+ and neutral H) is obtained.

erence. One way out is to align the target. A few studies for estimating the geometry of precursor molecular ions aligned by an intense laser field were done [Cor96a, Cor96b, His99a, His99b, San99, Bri07, Sie02b, Bry00]. No work has been reported for free targets. To estimate the geometry of free targets the only way out is to have the complete kinematic information of the fragments.

3.4.2 Energy levels

Consider the fragmentation of a parent ion AB^{2+} of mass m_{AB} , which is initially at rest.



The excess internal energy of the molecular ion due to the energy transfer in the collision is distributed among the internal degrees of freedom. The internal energy of the parent is released as translational energy of departing fragments. The sum of the kinetic energies of all fragments is called as kinetic energy release (KER). Let \vec{p}_A and \vec{p}_B be the momentum vectors of the ionic fragments, in the center-of-mass frame. Once again, due to the near equivalence of the laboratory and centre-of-mass frames, KER is equal to the sum of the kinetic energies of coincident fragments measured in the laboratory frame.

$$KER = \frac{p_A^2}{2m_A} + \frac{p_B^2}{2m_B} \quad (3.5)$$

The energy released depends on the shape of the potential energy surface of the initial and final states of the precursor ion. Thus, measurement of KER is a probe of the potential energy surfaces of the precursor molecular ion that participates in the fragmentation (see Figure 3.6). As an example, Figure 3.6 shows the KER spectrum for the break-up $CO^{2+} \rightarrow O^+ + C^+$.

Measurements of KER have existed for a few decades. Curtis *et al* have estimated the mean kinetic energy release during the break-up from the extents of the correlated TOF distributions [Cur85]. Measured values of KER have been found to be useful for determining the intercharge distances under the coulomb explosion model of molecular ion break-up [Sie00, Tom01]. With the aid of elab-

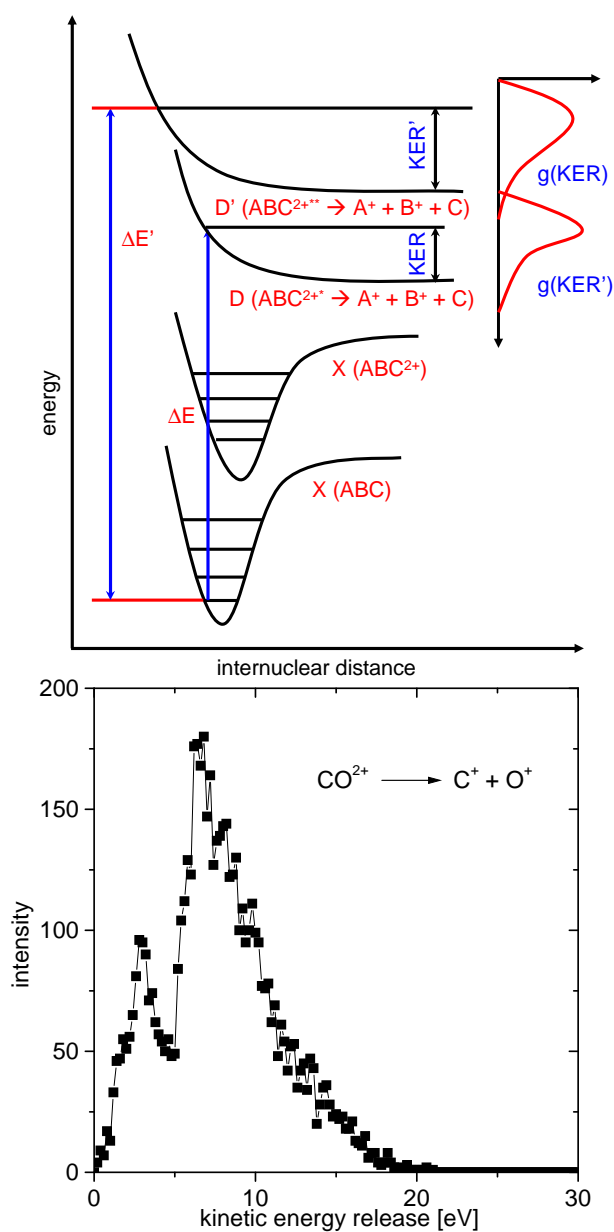


Figure 3.6: [Top] The relation between potential energy surface and kinetic energy release. [Bottom] Kinetic energy release distribution for the $C^+ : O^+$ break-up channel induced by 1300 eV electron impact on CO molecule. The structures in the distribution correspond to the excited states involved in the break-up. A dissociation involving more than one intermediate PES will lead to broad, multi-modal kinetic energy distribution.

orate theoretical modelling, measurements of KER distributions have led to information on binding energies [Las01]. These studies were done by analysing the magnitude or a single component of the fragment velocity, followed by the assumption that the break-up is isotropic. Now, with complete measurement of the momentum vector of the fragment ion this assumption need not be made, in fact the assumption of isotropy can be tested.

3.5 Need for quantum chemical calculations

Experimental KER or angular distributions alone cannot complete the study of dissociation dynamics. What are needed are computations of the potential energy surfaces. A complete theoretical study of a fragmentation which allows full comparisons with the experimental results requires an accurate PES. To find the PES we must solve the electronic Schrödinger equation at a very large number of nuclear configurations [Lev05b]. While the differences in the dissociation limits of the participating states determine the value of the fragment kinetic energy for a specific event, the transition probabilities from one state to other govern the distribution of the KER. It is here that experimental KER can aid theory, and *vice versa*. Similar considerations apply to the synergy of structure calculations and angular distributions leading to bond angles.

With the availability of powerful computers and quantum chemical software the *ab initio* calculations of the total energy of molecules and its ions has become possible. In our work, we have benefited from computations done for some molecular ions by our collaborators at IIT-Kanpur.

Chapter 4

Fragmentation of a linear triatomic : CO₂

The fragmentation dynamics of multiply charged molecular ions of triatomic molecules have attracted growing interest in recent years because the complete kinematics of all fragments arising from a single break-up event can easily be deduced as compared to polyatomic molecules. The most frequently studied molecule is CO₂, primarily due to its importance in terrestrial and planetary atmospheres. Absolute cross-sections for dissociation channels arising from the break-up of double, triple, and quadruple ionisation of CO₂ under electron impact [Tia98] and branching ratios of fragmentation channels initiated by synchrotron radiation [Mil86, Hsi95, Cur85, Ela87a] have been obtained. On the theoretical front, the excited energy levels of CO₂²⁺ were calculated [Hoc95, Hoc98]. Although CO₂²⁺ has both linear and bent excited states, these calculations were restricted to linear states.

We have investigated the fragmentation dynamics of CO₂²⁺ through estimation of its energy levels, deduction of its geometry and the lifetime of its metastable state. Our investigation was supported by quantum chemical *ab initio* calculations using MOLPRO [MOL] suite of programs.

Two sets of experiments were carried out. The first is by electron impact using the set-up described in the preceding chapters. The other is by photoabsorption, done at the INDUS-1 synchrotron. The latter experiment used a simple two-stage Wiley-McLaren TOF spectrometer with multi-hit ion detection capability.

We used a CO₂ sample which was purified in two stages by distillation, in order to get rid of air (N₂ and O₂) and water (H₂O) contamination. In the first distillation stage at 253 K, H₂O remained frozen while CO₂ and air were extracted into another chamber. H₂O was then discarded. In the second distillation stage, just above 77 K, CO₂ remained frozen, while air was pumped out. The process was repeated two to three times. The TOF mass spectrum of the purified sample showed no contamination.

4.1 Break-up channels

Six ionic species – C²⁺, C⁺, O⁺, CO₂²⁺, CO⁺, CO₂⁺ – are prominently seen in the TOF spectrum under 1300 eV electron impact (see Figure 4.1).

There are three prominent islands in the $t_1 : t_2$ coincidence map. They correspond to coincident ion pairs CO⁺:O⁺, O⁺:O⁺ and C⁺:O⁺ arising from the break-up of CO₂²⁺. The branching ratios are 0.61, 0.08 and 0.31, respectively. Of these CO⁺:O⁺ is due to a two-body break-up. O⁺:O⁺ and C⁺:O⁺ are due to three-body break-ups, with the third partner being neutral C and O, respectively.

4.2 Two body break-up

The two body break-up, CO⁺:O⁺, is the dominant channel. Being a two body break-up, the ion momenta are anticorrelated and the CO⁺:O⁺ angular distribution ought to ideally have a peak of zero width at 180°. However, due to instrumental limitation, the angular distribution may have a peak of finite width. Figure 4.2 is the angular distribution of CO⁺ ion relative to O⁺. The FWHM of the lobe is ±8°, and can be taken to be the approximate angular resolution of our instrument.

Due to the anti-correlation between the momenta of CO⁺ and O⁺, we cannot derive non-trivial information related to the geometry. However, the KER, and thereby the excited energy levels of the molecular ion, can be deduced. This break-up shows signatures of a metastable decay, which is discussed next.

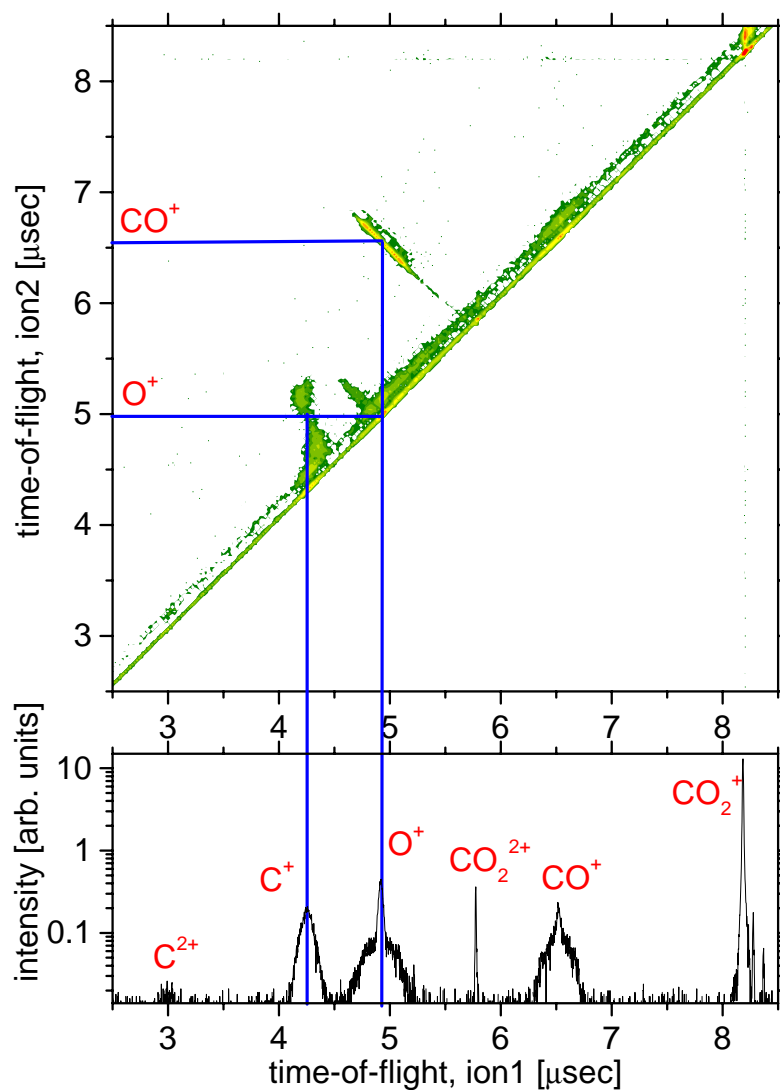


Figure 4.1: The lower panel of the Figure shows the TOF of fragment ions recorded as hit1. The upper panel of the Figure shows the coincidence map of the correlated fragment ion pairs. Three prominent islands are seen in the map which correspond to $\text{CO}^+:\text{O}^+$, $\text{O}^+:\text{O}^+$ and $\text{C}^+:\text{O}^+$ resulting from the break-up of CO_2^{2+} .

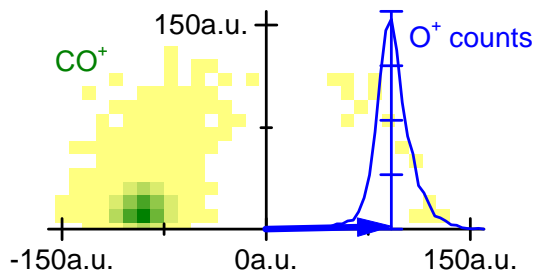


Figure 4.2: Momentum distribution of CO^+ with respect to the momentum of O^+ . The continuous curve is the scalar momentum distribution of O^+ , with 771 counts at the peak. The maximum of the CO^+ colour scale is 550 counts.

4.2.1 Lifetime of metastable CO_2^{2+}

The $t_1 : t_2$ coincidence map under electron impact (Figure 4.1) as well as photoabsorption (Figure 3.2) show $\text{CO}^+ : \text{O}^+$ coincidence counts mainly distributed as an island along the reverse diagonal. This is because the momenta of the two fragments are anticorrelated. This island is due to prompt decay of the CO_2^{2+} , but a tail is seen emerging from it, leading to the forward diagonal. This indicates a metastable decay, even though the V -shaped structure near the diagonal is missing. The reason for the missing V could be that the flight time of the undissociated CO_2^{2+} is shorter than its lifetime. We also note that the states accessed in the two experiments could be different. To investigate this feature, we performed the electron impact experiment at a lower extraction voltage, so that the flight time could be prolonged beyond the lifetime.

Figure 4.3 shows the $t_1 : t_2$ coincidence map for 30 V/cm extraction field. The flight time of the stable CO_2^{2+} in this configuration is 8.2 μs . From the intensities in the tail and the V , we determine the lifetime of CO_2^{2+} to be $5.8 \pm 1.5 \mu\text{s}$ (refer Equation 3.3). The error in the lifetime is due to the error in the determination of tail and V intensities. Lifetimes ranging from 0.9 to 21.6 μs have been reported for this molecular ion [Fie93, New64, Tsai80]. This suggests that CO_2^{2+} has several metastable states.

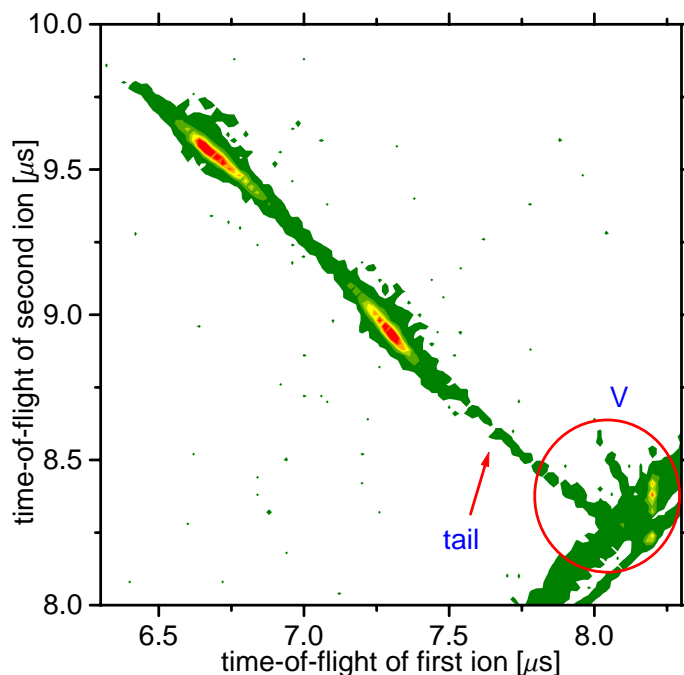


Figure 4.3: Ion pair coincidence map for the break-up $\text{CO}_2^+ \rightarrow \text{CO}^+ + \text{O}^+$ obtained at 30 V/cm extraction field. The tail and the V emerging from the main $\text{CO}^+ : \text{O}^+$ distribution are due to metastable states as explained in the text. The t_1 ordinate of the dotted line is the flight time of CO_2^+ , if it were to remain intact.

4.2.2 Potential energy surface of molecular ion

Figure 4.4 is the kinetic energy release (KER) spectrum of the $(\text{CO}^+ : \text{O}^+)$ break-up. Structures seen in the KER distribution are attributable to dication electronic states that participate in the fragmentation process. An interpretation of these peaks requires knowledge of the PES of the precursor and intermediate species. PES of dicationic CO_2 is developed theoretically by MOLPRO suite of program [MOL].

For studying dissociation dynamics an analytical function was fit to the *ab initio* PES and the dissociation dynamics of CO_2^+ was investigated using time-dependent quantum mechanical wave packet approach. Since the transition follows Frank–Condon principle, the stationary wave function, $|\Psi_g^{\text{CO}_2}(0,0,0)\rangle$, of ground state can be treated as non-stationary wave function of the excited state,

$|\Psi_g^{\text{CO}_2^{2+}}(t=0)\rangle$). This wave function then evolves with time on the potential energy surface for the electronic state of CO_2^{2+} .

$$|\Psi_g^{\text{CO}_2}(0,0,0)\rangle \longrightarrow |\Psi_g^{\text{CO}_2^{2+}}(t=0)\rangle \xrightarrow{H_g^{\text{CO}_2^{2+}}} |\Psi(t)\rangle.$$

Here, $H_g^{\text{CO}_2^{2+}}$ is the Hamiltonian for the ground electronic state of CO_2^{2+} . The autocorrelation function $c(t) = \langle \Psi(t=0) | \Psi(t) \rangle$ for the ground state of CO_2^{2+} is Fourier transformed yielding an excitation spectrum. The excitation spectrum when convoluted with instrumental resolution function yields the theoretical KER spectrum. The computed and experimentally obtained KER spectra are shown in Figure 4.4.

The peak at 4.9 eV is attributed to the $X^3\Sigma_g^-$ state of CO_2^{2+} . In this state the PES has a barrier height of 2.0 eV in the equilibrium geometry. The barrier height decreases with decrease in O–C–O bond angle. The structures in the predicted spectrum are attributed to the metastable states of CO_2^{2+} . The convoluted excitation spectrum is in good agreement with the experimental result in the low energy region. The discrepancy between theory and experiment at higher energies arises presumably due to the non-inclusion of the excited states of CO_2^{2+} . The theoretical *ab initio* calculations of PES were carried out in collaboration with IIT-Kanpur and detailed theoretical calculations are published elsewhere [Sha07].

4.3 Three-body break-up

The mechanisms of three-body break-up as classified by Eland [Ela87b], can be derived on the basis $t_1 : t_2$ coincidence maps alone. Since this information is available to us for both, the electron impact and photoabsorption data, we first carry out this analysis. The photoion coincidence spectrum (Figure 3.2) is richer than the electron impact spectrum (Figure 4.1) due to inner shell excitations. The ion pairs are found to arise from two precursors, namely CO_2^{2+} and CO_2^{3+} , whereas in the case of electron impact, there is only one precursor, CO_2^{2+} .

The slope of the best-fit line to the intensity distributions of ion pairs in the $t_1 : t_2$ coincidence map is compared with the predictions of Equation 3.1. The

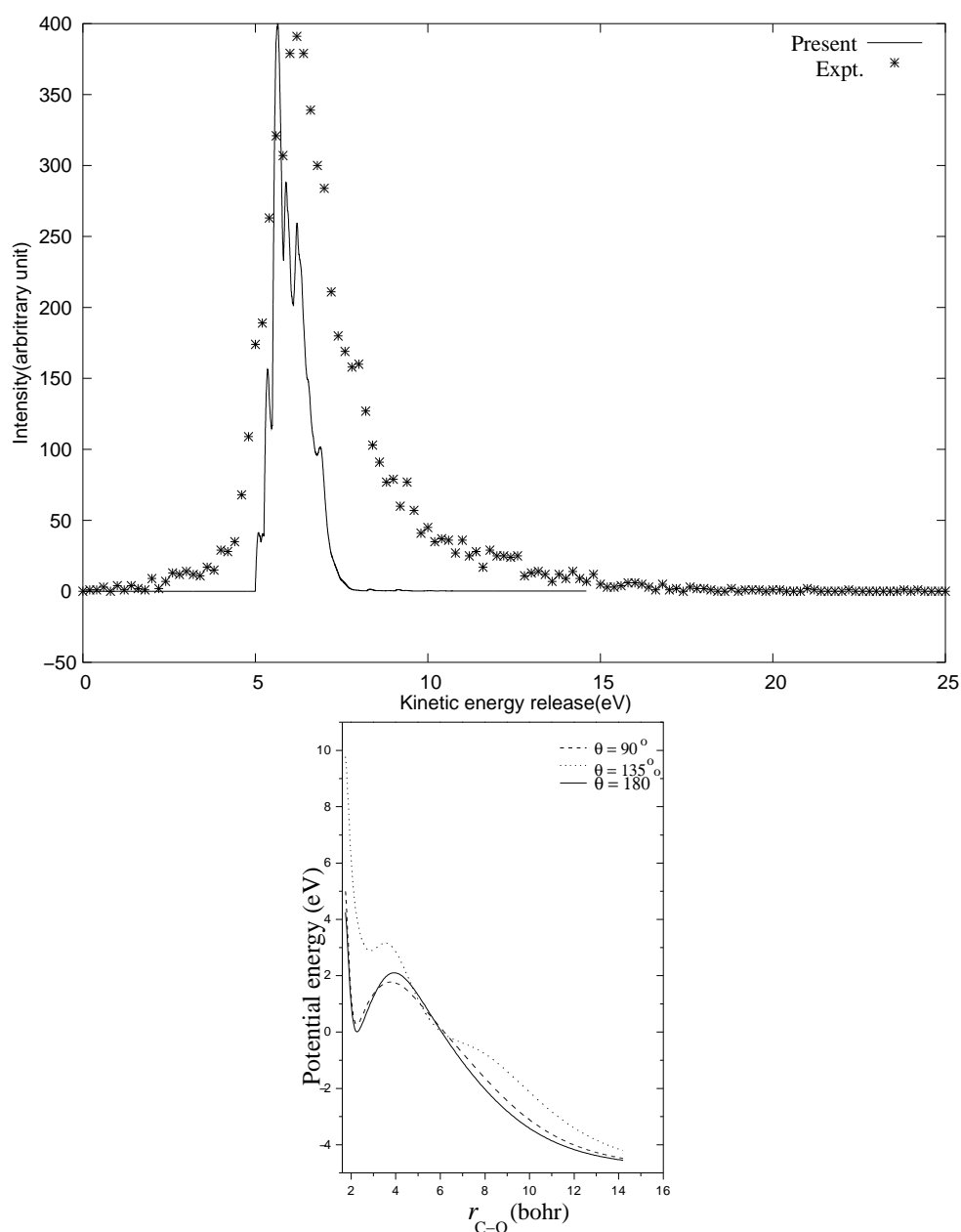


Figure 4.4: [Top] Comparison of the computed kinetic energy release spectrum for the CO^+ ($X^2\Sigma^+$) + O^+ (4S) fragmentation channel with the experimental results obtained by electron impact ionisation of neutral CO_2 . [Bottom] Potential energy profiles for dissociation of CO_2^{2+} are shown for different θ values, with the zero of energy corresponding to the (local) minimum energy geometry of CO_2^{2+}

Table 4.1: Comparison of the slopes of the best-fit line to the ion pair coincidence islands arising from photofragmentation of CO₂³⁺ with predictions of the ICS, DCS and concerted break-up models. R is the regression coefficient of the best-fit line.

channel	slope [ICS]	slope [DCS]	slope [fitted]	R	mode
O ⁺ :C ⁺ :O	-3.7	-1.0	-0.97 ± 0.03	0.90	DCS,c
O ⁺ :C:O ⁺	-2.75	-1.0	-2.1 ± 0.06	0.80	c, ICS
C ²⁺ :O ⁺ :O	-4.7	-2.0	-14.5 ± 1.5	0.70	c
O ²⁺ :C ⁺ :O	-0.86	-2.0	-0.62 ± 0.04	0.78	ICS
O ²⁺ :O ⁺ :C	-1.14	-2.0	-1.44 ± 0.04	0.90	c, ICS

fitted slopes and other parameters are summarised in Table 4.1. We find that no single process can explain the observed distributions. Studies done by Hsieh-Eland and Tian-Vidal on CO₂ lead to similar [Hsi95, Tia98] conclusions for the break-up of CO₂²⁺, as does our electron impact data. Ours is the first report for the break-up of CO₂³⁺.

Since in the electron impact experiment we have complete momentum maps of all fragments including the neutral fragment, we have an opportunity to obtain geometry information of the dissociating molecular ion from the momentum vectors of its fragments, following the method described in Chapter 3.

4.3.1 Geometry of dissociating molecular ion

The O⁺:O⁺:C channel

Figure 4.5 shows the momentum distribution of the second arriving O⁺ ion relative to the momentum vector of the first arriving O⁺ ion. Two distinct lobes are seen in the distribution, a weak one at 80° and the dominant one at 160°. This suggests that there are two precursor states of CO₂²⁺ leading to this break-up, with differing O–C–O angles, neither of which is 180°. The conjecture about the existence of two states is further supported by analysing the KE of the ions and the momentum vector of the neutral. The two sub-channels are separated by sort-

ing the list mode data into two, depending on whether the $O^+ : O^+$ angle lies in the range $40^\circ - 120^\circ$ or $120^\circ - 180^\circ$. It should be noted that the coincidence detection method is blind to events in which KE of two ions of the same species are comparable and the mutual angle is small.

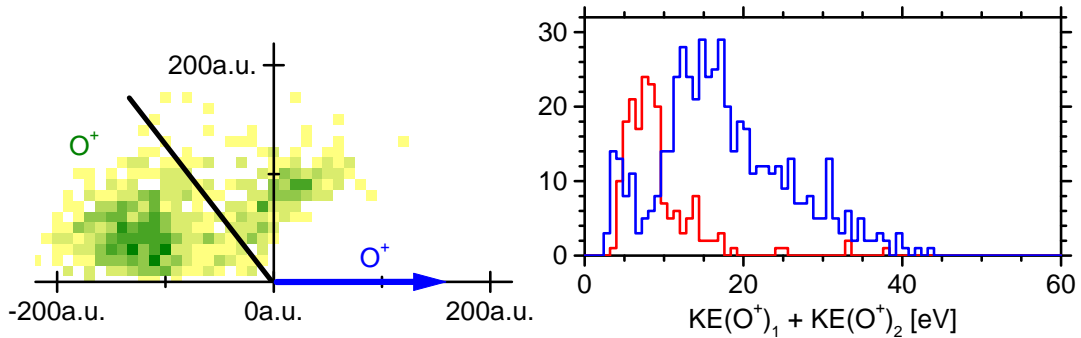


Figure 4.5: [Left] Momentum distribution of the second O^+ ion with respect to the momentum of the first O^+ ion in the break-up $CO_2^{2+} \rightarrow O^+ + C + O^+$. The black line at $\alpha_{O^+:O^+} = 120^\circ$ groups the events into two. The maximum of the colour scale for the second O^+ ion is 12 counts. [Right] Sum of the kinetic energies of the two O^+ ions for $\alpha_{O^+:O^+} < 120^\circ$ (red curve), and $\alpha_{O^+:O^+} > 120^\circ$ (blue curve).

Two KER distributions are obtained for two ranges of the $O^+ : O^+$ angle and plotted in Figure 4.5. These clearly show that for break-up with small $O^+ : O^+$ angle, the KE sum of the two O^+ ions is small whereas for large $O^+ : O^+$ angle the KE sum is large. The mean of the KE sum in the two cases are 8.7 eV and 17.3 eV, respectively. This can be understood as follows: O atoms are the terminal atoms and C is the central atom in the CO_2 molecule. When O^+ ions depart with a large mutual angle, the central C atom would carry small KE. Most of the KE will be carried away by the O^+ ions. On the other hand, when the $O^+ : O^+$ mutual angle is small, the KE carried away by the C atom will be larger.

For the two angular ranges mentioned above we have deduced the momentum of the neutral fragment. This is shown in Figure 4.6. For small $O^+ : O^+$ angle, the C atom is preferentially emitted around 130° to the first O^+ whereas for large $O^+ : O^+$ angle, the preferred angle is approximately 90° . We have verified that

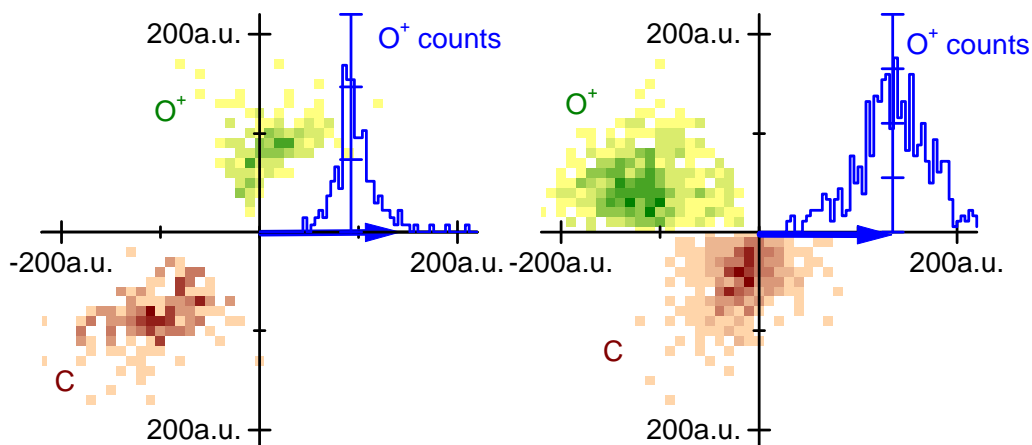


Figure 4.6: Momentum map of all fragments in the break-up $\text{CO}_2^{2+} \rightarrow \text{O}^+ + \text{C} + \text{O}^+$. [Left] For $\alpha_{\text{O}^+:\text{O}^+} < 120^\circ$. The continuous curve shows the momentum distribution of the first arriving O^+ , with 23 counts at the maximum of the peak. The maximum of the colour scale for the second O^+ is 9 counts and for C it is 7 counts. [Right] For $\alpha_{\text{O}^+:\text{O}^+} > 120^\circ$. The continuous curve shows the momentum distribution of the first arriving O^+ with 32 counts at the maximum of the peak. The maximum of the colour scale for the second O^+ is 12 counts and for C it is 20 counts.

these distributions are identical under the exchange of labels 1,2 of the O^+ ions. From these observations we conclude, that the break-up is symmetric and the two bonds break simultaneously. Two preferred geometries as shown in Figure 4.6 for the break-up channel $\text{CO}_2^{2+} \rightarrow \text{O}^+ + \text{C} + \text{O}^+$ emerge from these observations.

The $\text{C}^+:\text{O}^+:\text{O}$ channel

Figure 4.7 is the momentum distribution of O^+ and neutral O relative to the momentum vector of C^+ . Both distributions are broad and single lobed. In the former case the intensity is maximum around 150° while in the latter the intensity is maximum around 30° . The emission of O^+ and neutral O is not symmetric with respect to the emission of C^+ . This implies fragmentation via an asymmetric stretch and can be understood as follows. The two positive charges reside on C

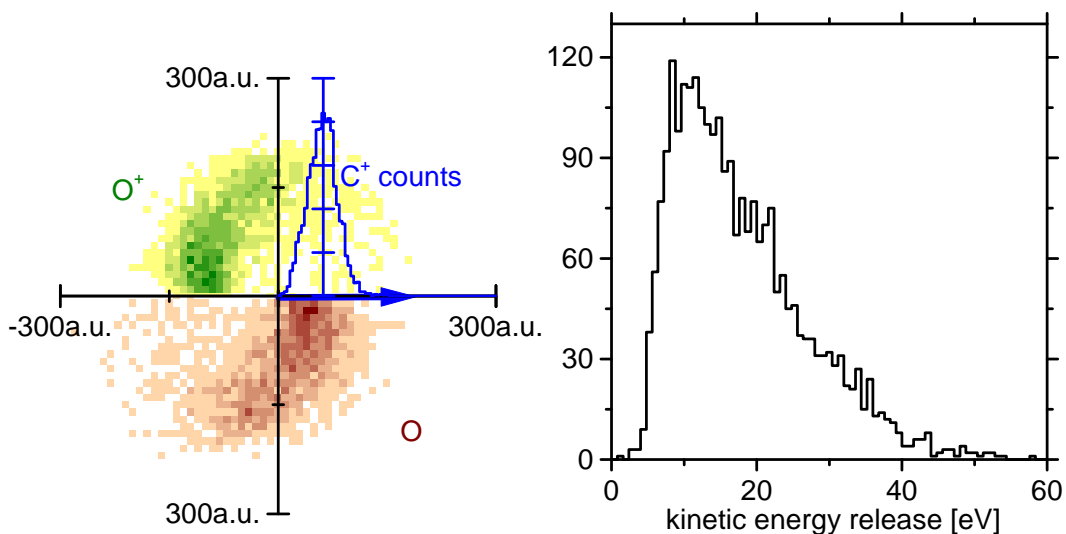


Figure 4.7: [Left] Momentum map of all fragments in the break-up $\text{CO}_2^{2+} \rightarrow \text{C}^+ + \text{O}^+ + \text{O}$. The continuous curve shows the momentum distribution of C^+ with 210 counts at the maximum of the peak. The maximum of the colour scale for O^+ as well as O is 30 counts. [Right] Kinetic energy release spectrum.

and on one of the O atoms. The two atoms move apart under coulomb repulsion. In the absence of the second (neutral) O, the two ions would be emitted back to back. However, the neutral O causes the trajectory of the C^+ to deviate. A $\text{C}^+ - \text{O}$ scattering leads to a small angle between the momentum vectors of C^+ and O. Unlike in the $\text{CO}_2^{2+} \rightarrow \text{O}^+ + \text{C} + \text{O}^+$ break-up, only one O–C–O angle is prominently seen in this break-up. Consistent with the momentum distributions, the KER also has a single broad distribution (Figure 4.7).

We conclude from the above analyses, that the three-body break-ups of CO_2^{2+} follow from two bent dissociative states. The kinematics of each dissociation channel and the geometry of the bent states are summarised in Figure 4.8. Two bent states of CO_2^{2+} , one with mean O–C–O angle $157 \pm 8^\circ$ and the other $86 \pm 8^\circ$ lead to the break-up $\text{CO}_2^{2+} \rightarrow \text{O}^+ + \text{C} + \text{O}^+$. The mean KER for these channels are 18.4 ± 4.4 eV and 20.3 ± 4.8 eV. The second three-body break-up, $\text{CO}_2^{2+} \rightarrow \text{O}^+ + \text{C}^+ + \text{O}$, also arises from bent mode, with mean O–C–O angle $155 \pm 8^\circ$. Within experimental error this O–C–O angle is the same as that for the first break-up

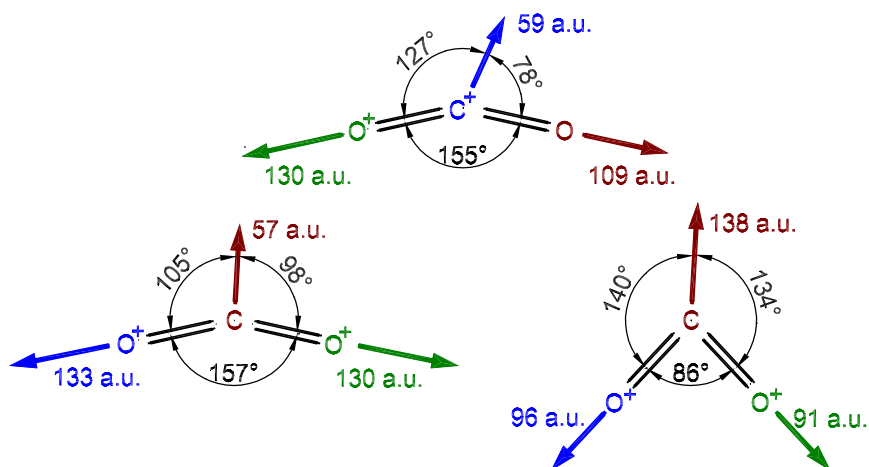


Figure 4.8: Schematic diagrams showing bent dissociative states of CO₂²⁺ leading to three-body break-ups. The mean momentum of each fragment is shown next to the respective symbol. The angles are the mean angles.

channel. However, the break-up CO₂²⁺ → O⁺ + C⁺ + O involves an asymmetric stretch. The mean KER for this channel is 15.5 ± 4.1 eV.

4.4 Considerations for polyatomics

For a triatomic molecule the only possible change that can occur in the geometry is the bond angle. However, for polyatomic molecules which have higher order of symmetry there may occur a multitude of changes. The change can, in fact, be substantial and may lead to an entirely altered geometry, which is the topic of discussion of the next chapter.

Chapter 5

Fragmentation of symmetric polyatomics : CCl₄, SF₆

Fragmentation dynamics of polyatomic molecular ions presents formidable challenges, because of the large number of open dissociation channels as well as the large number of fragments that can arise from a single dissociation. Symmetric polyatomic molecules are in some sense a transition between small molecules and very large ones because of the symmetry related degeneracy of dissociation channels. Removal of a few electrons from the symmetric electron clouds in molecules of high degree of symmetry, such as SF₆ and CCl₄, can lead to drastic changes in the structure of these molecular ions. Bond rearrangement may lead to the formation of ionic species contrary to the expectations based on symmetry. Intramolecular bond rearrangement has been observed by many workers in the past, in simple triatomic [Nag94, Str96] and polyatomic molecules [Ruh90, Rej02, Fur05] upon charged particle or photon impact. Bond rearrangement implies an alteration in the geometry of precursor molecular ions. Explanation of the rearrangements have been largely speculative, there has been no concrete proof of the rearrangement process *per se*.

This chapter deals with the alteration in geometry and migration of atoms in a dissociating molecular ion. Molecules having a high order of symmetry, SF₆ and CCl₄, are chosen for our study. SF₆ has an octahedral geometry whereas CCl₄ has a tetrahedral geometry. Both molecules have an atom at the centre, surrounded by six and four electronegative atoms, respectively. Because they are alike in this

respect, we expect similarities in dissociative ionisation of the two. We have investigated the issue of stability of certain molecular ion fragments arising from the break-up of the two molecules. We have also focused on the formation of molecular ions that require migration of atoms from their locations in the neutral molecule, and finally, on the determination of the geometry of the dissociating state.

5.1 Stability patterns in molecular ion fragments

SF_6

The mass spectrum of SF_6 under 1300 eV electron impact is shown in top panel of Figure 5.1. Eleven ionic peaks, viz., F^+ , SF^{2+} , S^+ , SF_2^{2+} , SF_3^{2+} , SF^+ , SF_4^{2+} , SF_2^+ , SF_3^+ , SF_4^+ and SF_5^+ , are seen. Parent ions, i.e. ions of the type SF_6^{q+} , are absent from the mass spectrum. Hence, we conclude that all parent molecular ions are unstable.

Figure 5.1 is bar plot for the intensity of the fragment ions arising from the break-up of multiply charged SF_6 ions. The probability of formation of SF_{2n+1}^+ ions is higher than that of SF_{2n}^+ ($n = 0-2$). Similarly, SF_{2m}^{2+} ions are more probable than SF_{2m+1}^{2+} ($m = 0-2$). The common thread here is that all ions, which are found to be stable, have even number of electrons.

The number of electrons appears to be of further significance, as is seen from the following considerations. As seen in Figure 5.2, the decay of dicationic SF_6 preferentially follows those channels which lead to fragments with even number of electrons. SF_6^{2+} dissociating into F^+ and SF_{2n-1}^+ shows higher probability than SF_6^{2+} dissociating into F^+ and SF_{2n-2}^+ , where $n = 1-3$. The dominant break-up channel is ($\text{F}^+:\text{S}^+$), in which both fragments are atomic, and hence are stable.

This kind of behaviour has also been observed by a few other groups [Hit79, Nas96, Sin03]. Of these, Hitchcock and Van der Wiel [Hit79] offered an explanation for the observed stability pattern. The primary assumption was that the charge resides on the central S atom. The explanation of bond stability was based on the valence-bond configuration of the fragment ions. Singly charged molec-

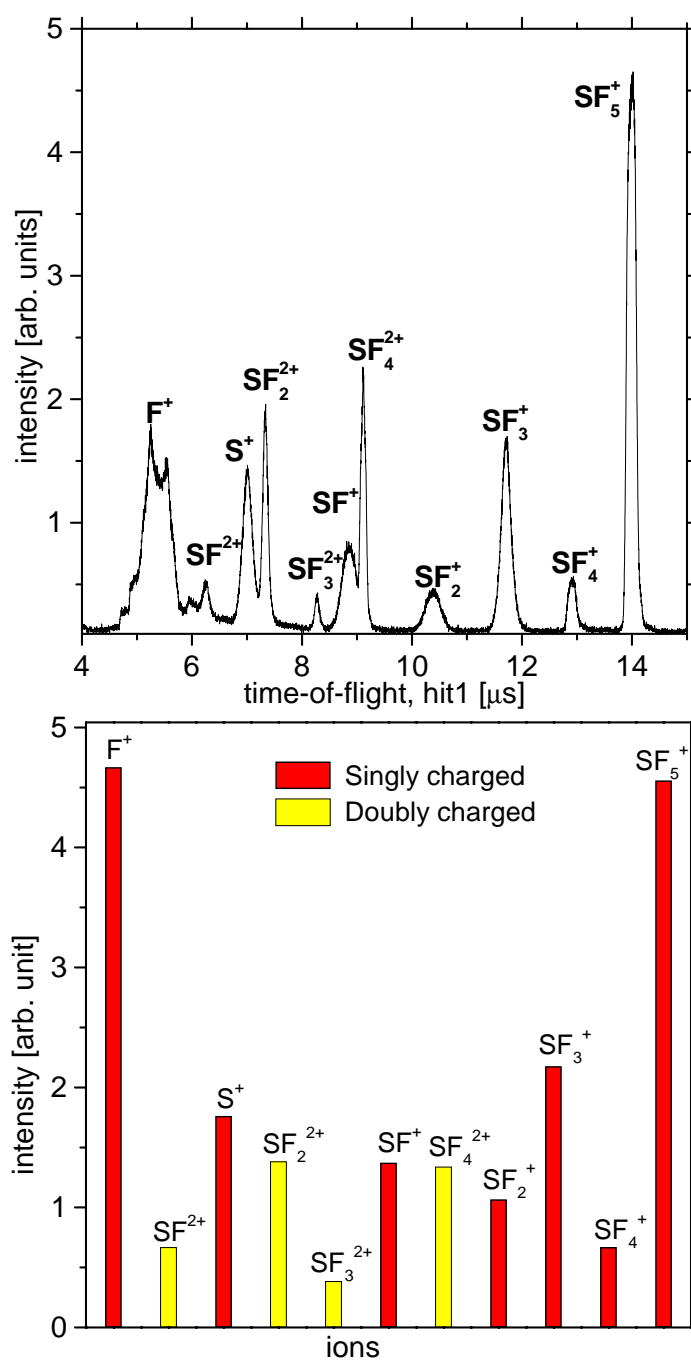


Figure 5.1: [Top] Time-of-flight spectrum of SF_6 . [Bottom] A bar plot showing the intensity of all fragment ions.

ular ions from SF₆ are considered to consist of an S⁺ ion with valence configuration 3s²3p³, and the appropriate number of F atoms. The optimum geometry for overlap consistent with the ground-state configuration of S⁺ implies preferential bonding to three F atoms, forming SF₃⁺. Excitation of one 3s² electron of S to the 3d orbital will give rise to the configuration 3s3p³3d of S⁺, which is optimal for bonding to five F atoms. One thus expects SF₅⁺ to be relatively stable. On the other hand, no configuration can be derived to optimise bonding for SF₄⁺ or SF₂⁺, so these ions are expected to be less stable.

Similarly, doubly charged molecular ion fragments from SF₆ are considered to be formed from S²⁺, whose valence configuration is 3s²3p², and the appropriate number of F atoms. This configuration yields preferential bonding to two F atoms whereas sp³ hybridisation yields optimal bonding for SF₄²⁺. No preferred configuration can be derived for SF_{2m+1}⁺.

CCl₄

The TOF spectrum of fragments from CCl₄ bombarded by 1300 eV electrons shows nine ionic peaks, viz., C²⁺, C⁺, Cl²⁺, CCl₂²⁺, Cl⁺, CCl₂⁺, Cl₂⁺, CCl₂⁺ and CCl₃⁺ (see Figure 5.3)a. Absence of parent ion peaks, viz. CCl₄⁺ and CCl₄²⁺, indicates that they undergo prompt dissociation. Parent molecular ions with charge > 2 would also be unstable, and several ion pairs are expected to be formed from their dissociation.

In a behaviour paralleling that of SF₆, ions of type CCl_{2n}⁺, which have even number of electrons are more likely to be formed, than CCl_{2n+1}⁺, which carry odd number of electrons. This is clearly seen in Fig. 5.3. We explain this behaviour by extending the model of Hitchcock and Van der Wiel. Singly charged fragments of CCl₄ are considered to be constructed from a C⁺ ion (valence configuration 2s²2p¹) and the appropriate number of Cl atoms. Thus, the ground-state configuration of C⁺ implies preferential bonding (optimum geometry for overlap) to one Cl atom. This explains the formation of CCl⁺. Excitation of one 2s² electron of C⁺ ion into one of the 2p orbitals causes sp² hybridisation, forming bonds with three Cl atoms. This explains the relatively stable configuration of CCl₃⁺.

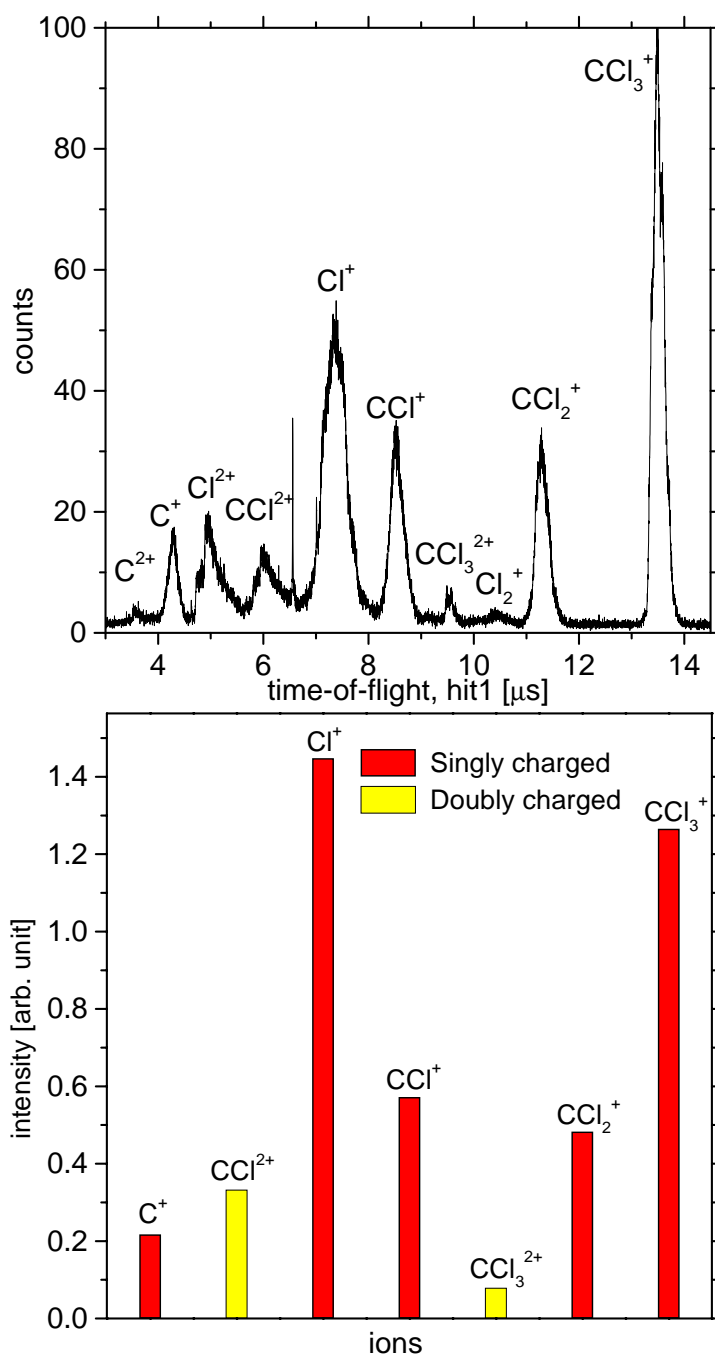


Figure 5.3: [Top] Time-of-flight mass spectrum of CCl_4 . The sharp peak in the spectrum at 6600 ns ($\equiv m/q = 28$) is due N_2 contamination. [Bottom] A bar plot showing the intensity of all fragment ions.

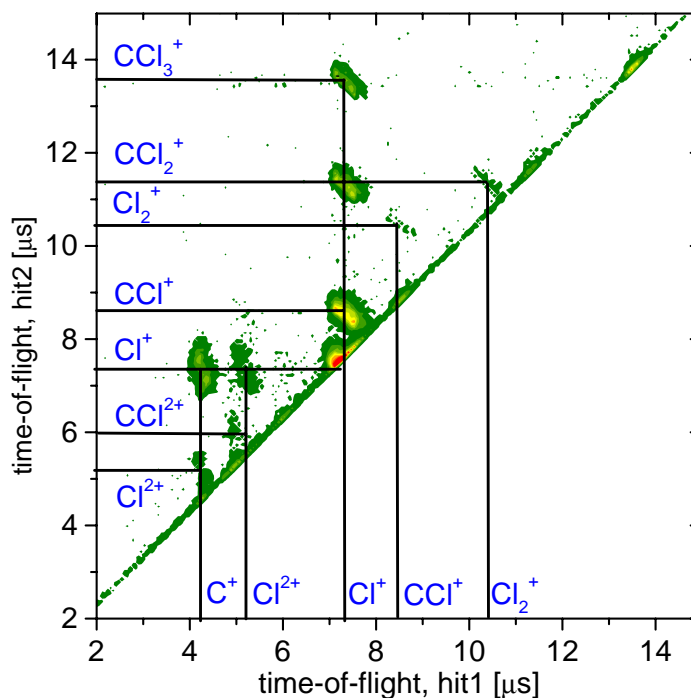


Figure 5.4: The coincidence map of the correlated fragment ion pairs arising from the dissociative ionisation of CCl_4 .

Thus, the high-low probability pattern in the formation of various types of *singly charged* fragment ions is qualitatively explained by this model.

The model fails when applied to the formation of *doubly charged* ions from CCl_4 . For C^{2+} the valence configuration is $2s^1 2p^1$. The best choice for bonding should have been two Cl forming a bond with C, forming stable CCl_2^{2+} . Extending this to the case of more Cl atoms, the valence bond model suggests that CCl_{2n}^{2+} is preferred over CCl_{2n+1}^{2+} . This in complete contradiction to observations. Ions of type CCl_{2n}^{2+} are not seen at all (see Figure 5.3), but ions of the type CCl_{2n+1}^{2+} ($n = 0, 1$) are observed. From the analysis of the shapes and the slopes of the distributions in the coincidence map of the correlated fragment ion pair, we deduced that the only precursors to these break-ups are CCl_4^{2+} and CCl_3^{3+} .

5.2 Migration of atoms during dissociation

The observation of F_2^+ (a tiny peak at $m/q = 38$) in the spectrum of SF_6 and the observation of Cl_2^+ (a tiny peak at $m/q = 71$) in the spectrum of CCl_4 indicate that at least one of the apical atoms in either molecule migrates during dissociative ionisation. This point can be dealt with more closely by looking at the ion pair coincidences. These deductions are based on the shapes and slopes of the ion pair coincidence distributions (Figure 5.2 for SF_6 and Figure 5.4 for CCl_4).

SF_6

We consider channels that lead to F_2^+ . The precursor to its formation can be either SF_6^+ or SF_6^{2+} as shown below.



Formation of F_2^+ ion involves breaking of a S–F bond, and formation of a bond with another F atom. These two dissociation channels provide evidence for a non-octahedral geometry of the precursor ion and indicate migration of at least one F atom from its position at the apex of the octahedron.

CCl_4

The precursor to the formation of Cl_2^+ can be either CCl_4^+ or CCl_4^{2+} . Based on the single and pair coincidences, we deduce three channels which can lead to Cl_2^+ formation:



The relative probabilities for the formation of Cl_2^+ from the three break-up channels are obtained by comparing the intensities in the singles and coinci-

dence spectra. The values are 0.89, 0.07 and 0.04, respectively. These three dissociation channels provide evidence for a non-tetrahedral geometry of the precursor ion.

For both molecules, we find evidence for migration of atoms during dissociative ionisation – the formation of F_2^+ and Cl_2^+ . A fallout of migration is a change in the charge distribution within the molecule. A consequence of this can be alteration of the geometrical structure of the molecular ion. How severe this alteration is, will be discussed next.

5.3 Alteration in geometry

SF_6

Figure 5.2 shows the coincidence map of the fragment ions arising from dissociative ionisation of SF_6 . Two dissociation channels are from two body break-up, viz. $F^+:SF_5^+$ and $F_2^+:SF_4^+$. Rest of the channels are due to more than two-body break-up. The probability of break-up into three ions is estimated to be much less than one percent, based on the relative counts in the triple and pair coincidence maps. Therefore the analysis that follows is based on the ion pair coincidence maps, with the tacit assumption that the third partner is neutral.

As discussed in chapter 3, estimation of the geometry of fragmenting molecular ion is possible only when $n - 1$ out of n fragments are charged and are detected. Of the several channels seen in the coincidence map, only two qualify for this analysis. The channels are:



However, the statistics for first channel is poor, therefore it is not analysed. In the second channel the third partner is taken to be F_2 , because we have evidence for migration of F, and because F is a highly electronegative atom and will immediately form a bond with another F atom.

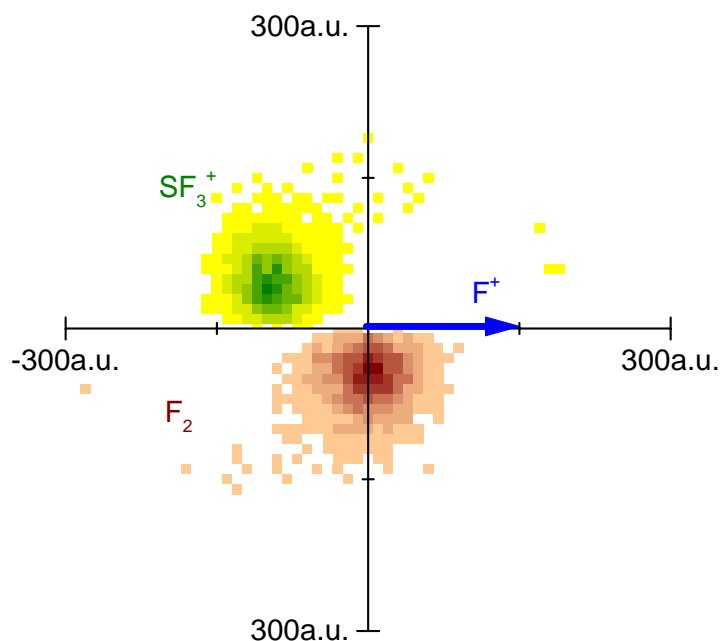


Figure 5.5: Momentum map of all fragments in the break-up $\text{SF}_6^{2+} \rightarrow \text{F}^+ + \text{SF}_3^+ + \text{F}_2$. The maximum of the colour scale for SF_3^+ is 140 and F_2 is 120 counts.

Figure 5.5 shows the angular distribution of SF_3^+ and the neutral F_2 fragment relative to the momentum vector of F^+ . The mean angle between F^+ and SF_3^+ is 138° , that between F^+ and F_2 is 96° , while that between SF_3^+ and F_2 is 126° . These observations indicate that the geometry of SF_6^{2+} is no longer octahedral like the parent. The average momenta carried away by F^+ , SF_3^+ and F_2 are 93 a.u., 121 a.u. and 83 a.u., respectively. The inequality of the emission angles and the mean momenta further suggest that the six F atoms in SF_6^{2+} are not equidistant, as in the original octahedral geometry. We have no theoretical support for the altered geometry, but work is in progress.

There are other clear pointers to alteration of geometry of SF_6^{2+} from the original octahedral geometry, although the angular distribution of all the fragments cannot be deduced as there are more than one neutral fragments. The channels

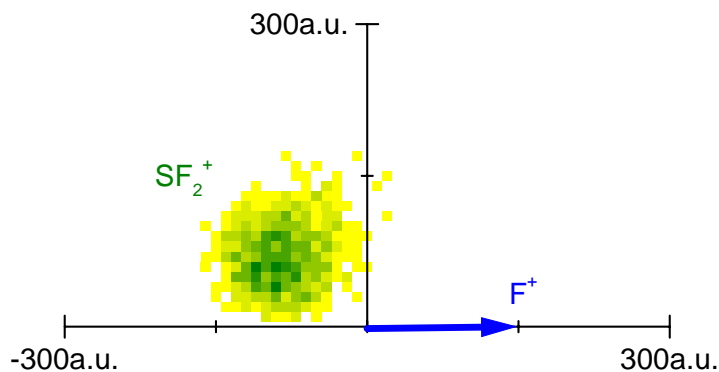
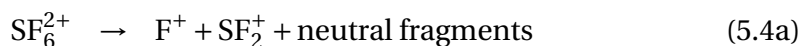


Figure 5.6: Momentum map of SF_2^+ relative to F^+ in the break-up $SF_6^{2+} \rightarrow F^+ + SF_2^+ + \text{neutral fragments}$. The maximum of the colour scale for SF_2^+ is 30.

pointing to alteration of geometry are:



Only first break-up channel is dealt with here. Figure 5.6 shows the angular distribution of SF_2^+ relative to the momentum vector of F^+ . The mean angle of emission of SF_2^+ relative to F^+ is 128° and the mean momenta carried away by F^+ and SF_2^+ are 100 a.u. and 124 a.u., respectively. In neutral SF_6 , F atoms are positioned either neighbouring or on opposite sides of the S atom i.e. the F-S-F angle is either 90° or 180° . The present observation shows that the angle has deviated from the original angle of 90° or 180° . The conclusion thus is, that the geometry of SF_6^{2+} is not the same as that of SF_6 .

The KER $SF_6^{2+} \rightarrow F^+ + SF_3^+ + F_2$ break-up is plotted in Figure 5.7. The experimental KER data is fitted with three Gaussians, with means 4.6 ± 0.03 , 6.02 ± 0.53 and 9.43 ± 0.63 .

CCl_4

To estimate the geometry of CCl_4^{2+} , only those break-up channels, in which the momentum of all the three partners can be deduced, should be considered. The

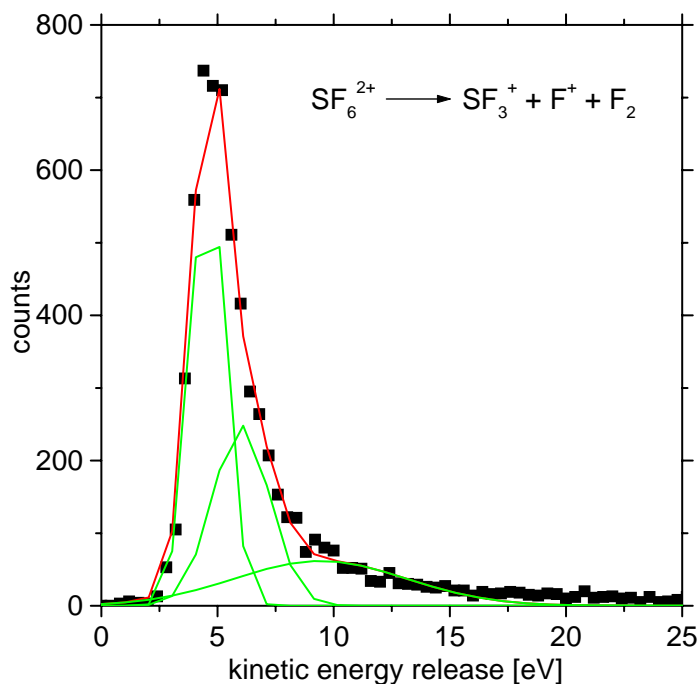
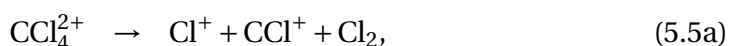


Figure 5.7: Kinetic energy release for the break-up $\text{SF}_6^{2+} \rightarrow \text{F}^+ + \text{SF}_3^+ + \text{F}_2$. Mean KER is 7.1 eV.

break-up channels are:



In the first of the above equations, we have assumed that the neutral fragment is Cl_2 . The precursor for this reaction is the same as that leading to Cl_2^+ in Equation 5.2c. The electronegativity of Cl is very high, and there are no electropositive atoms in the molecule. Thus, it is reasonable to assume that two Cl atoms will form a stable covalent bond if they are in a favourable position to form a bond. The formation of Cl_2^+ suggests that this is indeed the case. A proof for this altered position may be provided by the angles between the departing fragments, which we obtain from the momentum map of the fragments.

Figure 5.8 shows the angular distribution of CCl^+ ion and neutral Cl_2 relative to the momentum vector Cl^+ ion. The momentum distribution between the

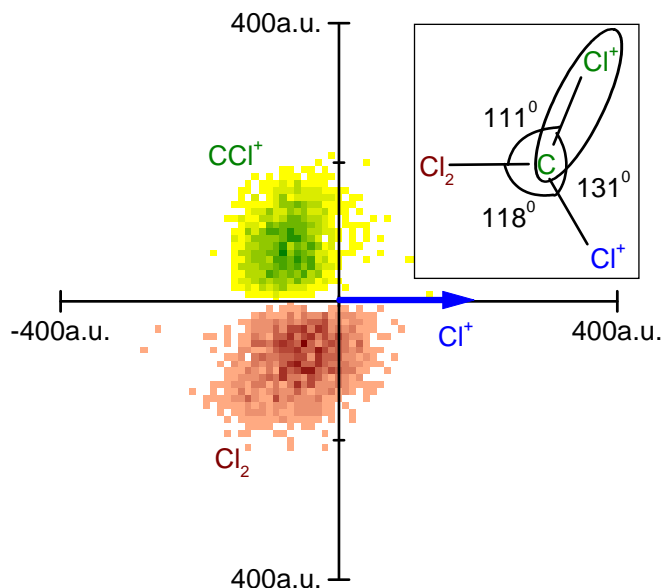


Figure 5.8: Momentum distribution of CCl^+ with respect to the momentum of Cl^+ . The maximum of the colour scale is 40 counts.

three bodies is nearly symmetric. The mean angle between Cl^+ and CCl^+ is 131° , that between Cl^+ and Cl_2 is 118° , while that between CCl^+ and Cl_2 is 111° . This further supports the assertion that the four Cl atoms are no longer equidistant, as in the original tetrahedral geometry. The average momenta carried away by Cl^+ , CCl^+ and Cl_2 are 126 a.u., 122 a.u. and 114 a.u., respectively.

Figure 5.9 shows the angular distribution of CCl_2^+ ion and neutral Cl relative to the momentum vector of Cl^+ ion. The mean angle between Cl^+ and CCl_2^+ is 141° , that between Cl^+ and Cl is 106° , while that between CCl_2^+ and Cl is 113° . The average momenta carried away by Cl^+ , CCl_2^+ and Cl are 120 a.u., 128 a.u. and 95 a.u., respectively.

Putting together the information about the two three-body dissociation channels, we are led to the conjecture that the geometry of CCl_4^{2+} in the dissociating state is trigonal. Since we have no evidence to the contrary, we assume that the C atom is at the centre of the molecule. The Cl atoms are rearranged: a pair of Cl atoms lie along one of the trigonal arms, the two lone Cl atoms are along the two other arms. In the first dissociation channel, this Cl-Cl bond is not broken and

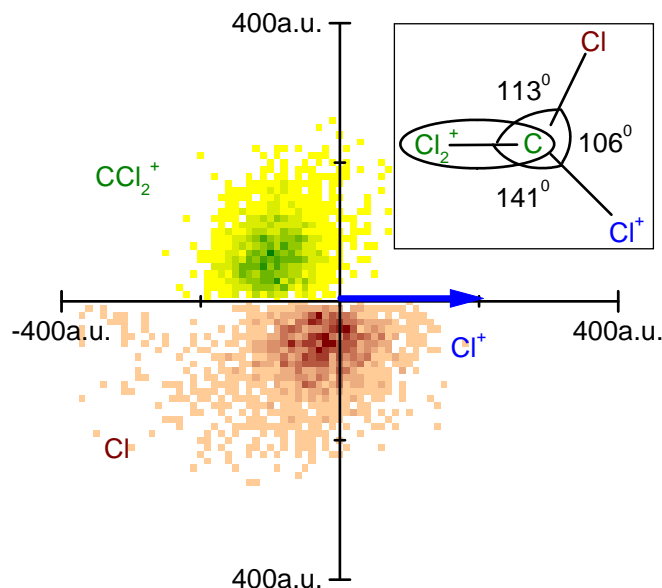


Figure 5.9: Momentum distribution of CCl_2^+ with respect to the momentum of Cl^+ . The maximum of the colour scale is 22 counts.

the pair remains neutral. The central C and one of the lone Cl atoms combine to form the second partner, while the other lone Cl is the third partner in the dissociation. The charge is shared between CCl and Cl. In the second dissociation channel, the paired Cl atoms and the central C atom combine and carry away one charge, while one of the two lone Cl atoms carries away the other.

Support for migration of the Cl atoms and modification of the bond angles also comes in from theory. The geometry optimisation of CCl_4^{2+} was carried out without any symmetry constraint using Gaussian03 program package with 6-31g* basis set at Restricted Hartree-Fock level. Figure 5.10 shows the geometry of CCl_4^{2+} calculated in this manner. It is clear that the geometry of the dication is very different from that of the neutral.

The kinetic energy of all fragments, including neutrals, can be determined for the fragmentation channels described above (reactions 5.5a, 5.5b). The KER in the two channels is nearly identical, as can be seen from Figure 5.11. The experimental KER data for $\text{CCl}_4^{2+} \rightarrow \text{CCl}_2^+ + \text{Cl} + \text{Cl}^+$ break-up channel is fitted with three Gaussians, with means 5.9 ± 0.07 , 9.8 ± 0.21 and 12.7 ± 3.1 . Similarly, the

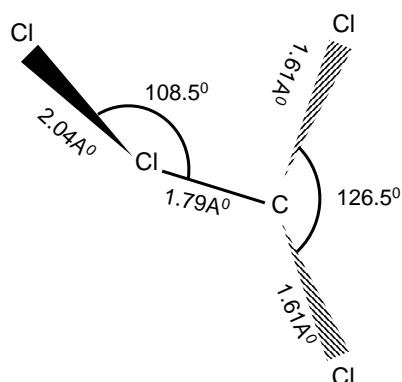


Figure 5.10: The computed structure of CCl_4^{2+} . The charge on the molecular ion is not shown.

experimental KER data for $\text{CCl}_4^{2+} \rightarrow \text{Cl}^+ + \text{CCl}^+ + \text{Cl}_2^+$ break-up channel is fitted with three Gaussians, with means 5.9 ± 0.03 , 9.8 ± 0.08 , 10.4 ± 0.9 . The similarity in the structures of KER indicates that the same set of states of CCl_4^{2+} lead to the two dissociation channels.

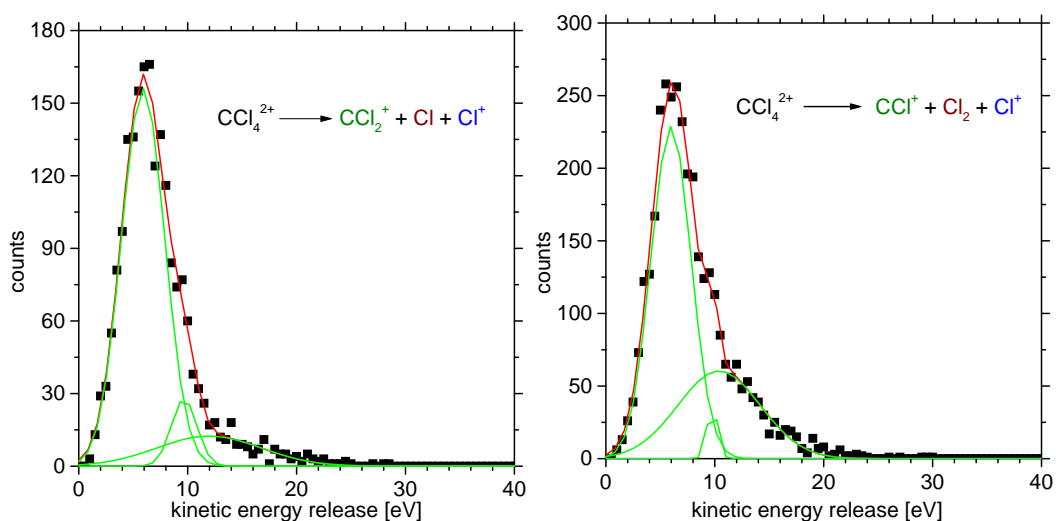


Figure 5.11: The kinetic energy release distribution for the $\text{CCl}_4^{2+} \rightarrow \text{Cl}^+ + \text{CCl}_2^+ + \text{Cl}_2^+$ and $\text{CCl}_4^{2+} \rightarrow \text{Cl}^+ + \text{CCl}^+ + \text{Cl}_2$ break-up channels induced by 1300 eV electron impact.

5.4 Effects due to asymmetry

In polyatomic molecules with high order of symmetry, like the ones considered here, dissociation of bonds or migration of atoms will be indistinguishable with respect to the site that was active during the process. It will be independent of the site at which the atom was located prior to dissociation. However, when one considers a polyatomic molecule which has several identical atoms attached to different atoms, or in other words a few identical atoms attached to different skeletal atoms, the issue of site selectivity or specificity in dissociation comes up. Alcohols are good candidates for this class of molecules. The site specificity in the bond breakage and bond rearrangement in ethanol is dealt with in the next chapter.

Chapter 6

Site specific dissociation:

C₂H₅OH

The discovery in the planetary atmospheres and interstellar atmospheres of organic molecules, such as alcohols has seen a new-found interest amongst chemists and atomic physicists [Kea87, Kis87, Man80]. Several spectroscopic and collision studies, under a variety of excitation schemes, have been done. Partial cross-sections for dissociative ionisation of methanol and ethanol by electron impact have been measured by Duric *et al*, Srivastava *et al* and Rejoub *et al* [Dur89, Sri96, Rej02]. Beyond cross-section measurements are more interesting issues, such as the formation of molecular ions involving non-intuitive bond rearrangements, exemplified by the observation of H₂⁺ and H₃⁺. The observation of H₃⁺ from CH₃OH by photoabsorption was reported by Ruhl *et al*, Rejoub *et al* and Furukawa *et al* [Ruh90, Rej02, Fur05]. Some explanations for the formation of H₂⁺ and H₃⁺ from CH₃OH and C₂H₅OH by photon and charged particle impact have been reported [Ruh90, Fur05, Kri04]. H atoms in alcohols are attached to different skeletal atoms such as C or O. Since the neighbours of H atoms at different sites are not identical, we expect H atoms at different sites to respond differently to a perturbation. A typical alcohol molecule carries a few identically sited H atoms and a variety of skeletal atoms. This makes alcohols ideal candidates for studying site-specific dissociation.

Ethanol (H₃C–CH₂–OH) is the simplest molecule for such a study, offering three different skeletal sites. We have studied the fragments arising from disso-

ciative ionisation of ethanol by electron-impact. The most significant observation is the large scale rearrangement of H atoms during dissociative ionisation, reflected in the formation of H_2^+ , H_3^+ , HOH^+ and H_2OH^+ ions. These ions can only be formed by breaking of bonds between the H and the skeletal C or O atoms, followed by association of the H atoms or ions. In order to understand these rearrangements, we need answers to questions such as – Are all bonds equally active in this rearrangement? Which excited states are responsible for the observed fragment ions? What are the energetics of the fragmentation channels of $C_2H_5OH^{2+}$? One of the most exciting challenges in chemistry is control over bond breaks. Understanding site selectivity in dissociation is the first step towards that goal. It requires a detailed knowledge of the potential energy surfaces as well as of the dynamics that governs the dissociation.

6.1 Tools of trade: Isotopic substitution

The optimised structure of C_2H_5OH is shown in Figure 6.1. Of the six H atom sites, the H''' site is very different from the rest in terms of the bond strength and symmetry of the orbital. The structure suggests that fragments arising from dissociative ionisation of ethanol can be grouped into two: those involving only the peripheral H atoms, and those involving one or more of the skeletal C and O atoms. To figure out whether the H atom attached to O does indeed behave differently from the other H atoms, it is necessary to tag it differently from the other H atoms. For this, we use isotopically altered ethanol (H_3C-CH_2-OD). The strategy then, is to perform the experiment with both isotopomers, and compare the fragmentation patterns. An important point here is that the electronic structure of the molecules is to a very great extent independent of the isotopic composition.

Isotopically altered ethanol used in the experiment was a commercially available sample with a D-atom purity of 99%. In the following discussion, we will refer to the H (or D) atom on the O site as *A*, to distinguish it from other H atoms. In the analysis that follows, we treat the C_2H_5OH molecule (henceforth

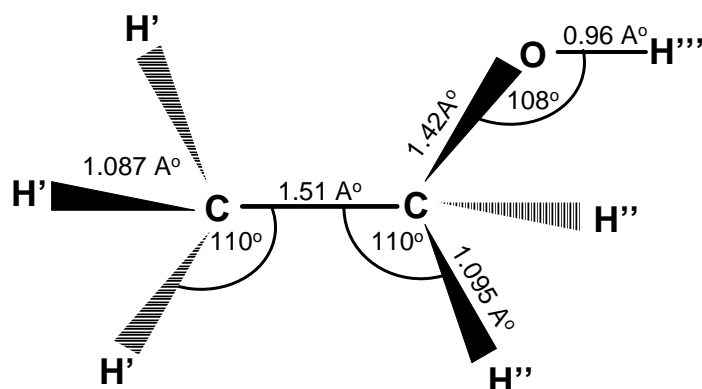


Figure 6.1: Structure of C_2H_5OH . The labelling H' , H'' , H''' is for distinguishing various H atom sites.

called h-ethanol) as the primary molecule being investigated, falling back upon the C_2H_5OD molecule (henceforth called d-ethanol) only when the identification of the dissociation channels calls for assistance from the isotopically altered species.

6.2 Identification of fragment ions

The time-of-flight spectra of ions from h-ethanol and d-ethanol, calibrated in terms of m/q are shown in Figure 6.2. Twenty-two and twenty-six ions are seen in the two cases, respectively. The peaks at $m/q = 28, 32$ in the C_2H_5OH spectrum are due to air contamination, but these do not affect the analysis. In addition to the parent ion peak we observe many other dissociation products. No multiply charged parent ion peak is observed in the mass spectrum. This leads us to the conclusion that multiply charged ethanol decays promptly.

The spectra are normalised to the area within the FWHM of the peak of the methyl ion (CH_3^+). A normalisation using the entire area was likely to give an error due to the merging tails of the adjacent peaks. The choice of this peak for normalisation is based on the fact that this is an ion which can arise from a unique site, and does not involve the isotopically substituted site. Thus, the relative intensity of all site-dependent fragments from the two isotopomers will

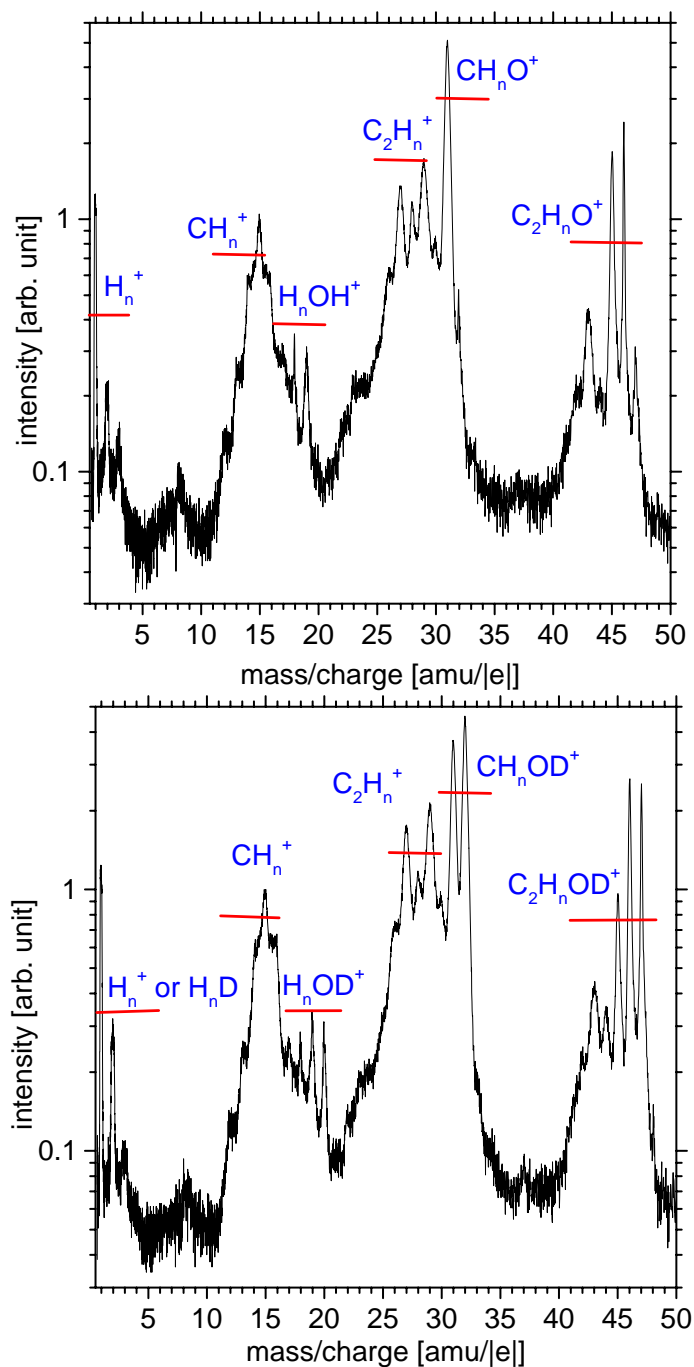


Figure 6.2: TOF spectra of C_2H_5OH and C_2H_5OD under 1300 eV electron impact normalised to the intensity of the CH_3^+ peak.

be correctly represented with this normalisation. We have verified, that this normalisation matches the normalisation against the total ion yield. It is obvious that differences in intensities of the peaks at the same m/q in the two cases point to reactions that involve the O–A bond. The peak at $m/q = 47$ in the mass spectrum of C_2H_5OH is the combined effect of natural fractions of isotopes of H, C and O. Corrections due to this have been taken into account in the analysis.

The peaks in the mass spectrum fall into six groups, namely the H_n^+ , CH_n^+ , H_nOH^+ , $C_2H_n^+$, COH_n^+ and $C_2OH_n^+$ groups. The parent ion peak is the most intense. The grouping in the mass spectrum can be linked to the structure of the molecule; the groups are consistent with the structure in Figure 6.1. Among the ion groups listed, the groups H_n^+ and H_nOH^+ involve rearrangements of H–bonds, while the others do not. We analyse the two categories separately.

6.2.1 Ions not requiring rearrangement of bonds

The CH_n^+ group

The relative intensities of CH_n^+ ions for a given n are equal for h-ethanol and d-ethanol. Thus the O–A bond is not involved in the formation of ions in this group. Ions of this group are formed when the C–C or C–O bonds break.

$C_2H_n^+$ group

Peaks at mass 24, 25, 26 and 27 are due to the C_2^+ , C_2H^+ , $C_2H_2^+$ and $C_2H_3^+$ ions, respectively. Mass 28 cannot be assigned to a single species, it could be either CO^+ or $C_2H_4^+$. The peaks in this group are identical for the two isotopomers (barring contamination due to N_2^+). This implies, that the formation of these ions does not require breaking of the O–A bond.

CH_nO^+ group

The masses in this group range from 29 to 31 in case of h-ethanol. Three ions, viz. $H_3C-CH_2^+$, $HC-O^+$ and $C-OH^+$ have mass 29. To determine which of these

ions formed the peak, we compare the normalised mass spectra of the two isotopomers. If the peak is due the $C-OH^+$ ion, then in d-ethanol this will contribute to the peak at mass 30 and the intensity at mass 29 will be different in the two cases. Since the ratio I_{29}/I_{30} for h-ethanol is same as that for d-ethanol, we conclude that the peak at mass 29 in h-ethanol cannot be due to $C-OH^+$. It is not possible to rule out or confirm the formation of the two other ions, $H_3C-CH_2^+$ and $HC-O^+$. A scheme of site-by-site substitution of H by D may shed some light on this. For the scheme to succeed, it is necessary to determine the intensity of each peak accurately. However, broad mass peaks in this group preclude the possibility at the moment. Masses 31 and 32 are exclusively assigned to CH_2OA^+ .

The $C_2H_nO^+$ group

In case of h-ethanol, three structurally different ions viz. $CH_3CH_2O^+$, CH_3CHOA^+ , $CH_2CH_2OA^+$ appear at the same m/q , but in case of d-ethanol the CH_3CHOA^+ and $CH_2CH_2OA^+$ ions would appear at $m/q = 46$. The ratio of the intensity of the peak corresponding to loss of one H atom to the intensity of the parent ion is the same in both molecules. (This fact is not obvious from the peak heights in the mass spectrum, due to differing peak widths.) This indicates that only C-H bonds, and not the O-A bond, are broken in processes involving loss of a single H atom.

6.2.2 Ions requiring rearrangement of bonds

The H_n^+ group

The h-ethanol spectrum has peaks at $m/q = 1, 2, 3$ corresponding to H^+ , H_2^+ and H_3^+ respectively. The d-ethanol spectrum, on the other hand, has peaks at $m/q = 1, 2, 3, 4$ corresponding to H^+ , H_2^+ or D^+ , H_3^+ or HD^+ , and H_2D^+ respectively. The comparison tells us, that the formation of H_2^+ or H_3^+ from h-ethanol involves a rearrangement necessitating the breaking of the O-H bond.

To calculate the site-specific probability of formation of H_n^+ ions, we proceed as follows. We assume that the sum of the normalised intensities of the peaks

at $m/q = 1 \dots 3$ in case of h-ethanol equals the sum over $m/q = 1 \dots 4$ in the case of d-ethanol. In other words, we assume that the sum of the cross-sections for rearrangements involving the peripheral H (or D) bonds is the same for the two molecules. The sum of the intensities of all ions in this group is arbitrarily set to 1, and the intensity of each peak is renormalised to this sum.

We label the contribution to the intensity of H_n^+ due to rearrangement of the H- bonds on the CH_3 , CH_2 , and OH sites by symbols with a prime, double prime and triple prime respectively. The normalised intensity of a particular mass peak is denoted by $p_{m/q}$. Thus, for the case of h-ethanol we have

$$p_1 = 0.694 \pm 0.004 = 3p_{H'} + 2p_{H''} + p_{H'''} \quad (6.1a)$$

$$p_2 = 0.189 \pm 0.001 = 3p_{H'H'} + p_{H''H''} + 2p_{H''H'''} \quad (6.1b)$$

$$p_3 = 0.117 \pm 0.001 = p_{H'H'H'} + p_{H''H''H'''} \quad (6.1c)$$

This scheme is justified on the grounds that the C-C bond is the longest and the H' atoms are far apart from the H'' and H''' atoms. Likewise, using the symbol P for the case of d-ethanol, we have

$$P_1 = 0.601 \pm 0.002 = 3P_{H'} + 2P_{H''} \quad (6.2a)$$

$$P_2 = 0.216 \pm 0.001 = 3P_{H'H'} + P_{H''H''} + P_D \quad (6.2b)$$

$$P_3 = 0.102 \pm 0.001 = P_{H'H'H'} + 2P_{H''D} \quad (6.2c)$$

$$P_4 = 0.081 \pm 0.001 = P_{H''H''D} \quad (6.2d)$$

We further assume the following equivalences:

$$p_{H'} = p_{H''} = P_{H'} = P_{H''} \quad (6.3a)$$

$$p_{H'H'} = p_{H''H''} = P_{H'H'} = P_{H''H''} \quad (6.3b)$$

$$p_{H'H'H'} = P_{H'H'H'} \quad (6.3c)$$

$$p_{H''H''H'''} = P_{H''H''D} \quad (6.3d)$$

The error in the probabilities is the net error due to statistical uncertainty and error in determining the baseline of the mass peak. Solving these equations, we find that H^+ formation has $86 \pm 0.3\%$ contribution from the five C-sited bonds and

$14 \pm 0.3\%$ from the O-sited bond. The contribution to H_2^+ from rearrangement of the bonds at the CH_3 site is $49 \pm 2\%$ and due to rearrangement of bonds at the CH_2 and OH sites is $51 \pm 2\%$. Similarly, $30 \pm 4\%$ of the H_3^+ intensity is due to rearrangement of the bonds at the CH_3 site while $70 \pm 4\%$ is due to the CH_2 and OH sites together. The last result is surprising, because it implies a large probability of breaking of the strong O–H bond. This result may be compared with the formation of H_3^+ by photoionisation of CH_3OH , for which Ruhl *et al* have reported rearrangement involving the O–H bond to be thrice as likely as the one not involving the O–H bond [Ruh90].

The H_nOH^+ group

The peaks at mass 18 and 19 for the case of h-ethanol and the peaks at mass 19 and 20 for the case of d-ethanol confirm formation of HOA^+ and H_2OA^+ ions. As in case of the H_n^+ group, the formation of these ions necessitate rearrangement of the H– bonds. The normalised intensity of HOH^+ from h-ethanol equals that of HOD^+ from d-ethanol. Similarly the intensities of H_2OH^+ in h-ethanol and H_2OD^+ in d-ethanol are equal within a percent. This implies, that the O–A bond does not break in any of these rearrangements.

KE distributions for H_n^+ and H_nOH^+ groups

Since H_2^+ , H_3^+ , HOH^+ and H_2OH^+ are formed due to bond rearrangement, several excited states may be involved in their formation, whose signatures would be seen in the kinetic energy distributions (KED). The excited states may be of either singly or doubly charged C_2H_5OA ions. The probability of single ionisation leading to dissociation is determined to be five times that of double ionisation leading to dissociation, based on the singles and coincidence spectra.

The KED of H_2^+ and H_3^+ ions from h-ethanol is plotted in Figure 6.3. The KED shown do not take into account whether that intermediate ion is singly or doubly charged. The KED could not be determined unambiguously for HOH^+ and H_2OH^+ from h-ethanol, as they are not very well resolved. However, the HOD^+

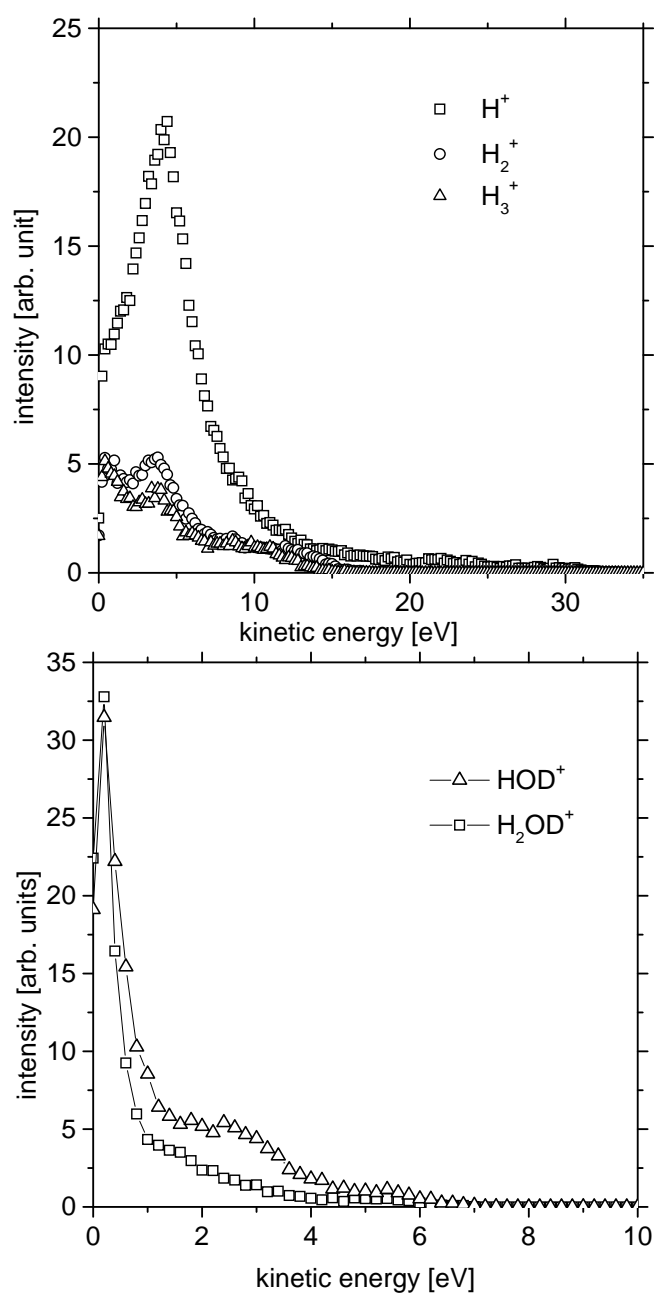


Figure 6.3: [Top] Distribution of kinetic energy of H^+ , H_2^+ , and H_3^+ ions from C_2H_5OH . For H_2^+ and H_3^+ distributions, the experimental data points are fitted to the sum of several Gaussian distributions, as indicated in the text. [Bottom] Distribution of kinetic energy of HOD^+ and H_2OD^+ ions arising from C_2H_5OD .

and H₂OD⁺ ions arise from a similar rearrangement in d-ethanol, and are better resolved. We take the KED of HOD⁺ and H₂OD⁺ to be similar to those of HOH⁺ and H₂OH⁺, respectively (barring a $\sqrt{\mu}$ scaling due to differences in the reduced mass). The KED of HOD⁺ and H₂OD⁺ ions are plotted in Figure 6.3.

We attempted to fit the observed KEDs to sum of Gaussian distributions:

$$y = \sum_i \frac{a_i}{\sigma_i \sqrt{\pi/2}} \exp[-2[(x - \mu_i)/\sigma_i]^2]$$

This attempt succeeded partly for H₂⁺ and H₃⁺ ions, but not for the others, although the KED of other ions also show a multi-peak structure. For H₂⁺ we obtain a fit of four Gaussian distributions (a_i, μ_i, σ_i): (480,0.64,1.1), (2249,3.3,3.5), (657,8.0,3.9), (435,12.4,3.6) with $\chi^2/\text{dof} = 190$. For H₃⁺ the fit consists of three Gaussian distributions (a_i, μ_i, σ_i): (533,0.63,1.2), (1588,3.2,3.6), (836,9.1,5.1) with $\chi^2/\text{dof} = 237$. We note, that the first two Gaussian distributions are almost identical for these ions (barring the amplitude). This suggests that the two ions may arise from the same transition to the intermediate excited state. The presence of multiple peaks can be taken to be an indication of the participation of many electronically excited states. A proper interpretation of these peaks requires knowledge of the potential energy surfaces of the parent and intermediate species. If this information is available, then a procedure based on the reflection approximation [Woo77, Liu89], and a linear combination of excitation functions from initial bound states to repulsive intermediate states can lead to an understanding of the dissociation dynamics. Such a scheme is employed in recent times to the study of fragmentation of CO and H₂O by ion impact [Tar00, Leg05]. A complete understanding of our data requires the calculation of PE surfaces of ethanol.

6.3 Decay channels of C₂H₅OH²⁺

Figure 6.4 shows the coincidence map of the TOF of the first and second ions arising from h-ethanol. All ions in this map are singly charged. Furthermore, no ion is recorded as third hit. Therefore, the precursors to all ion pairs are C₂H₅OH²⁺. The situation for d-ethanol is identical.

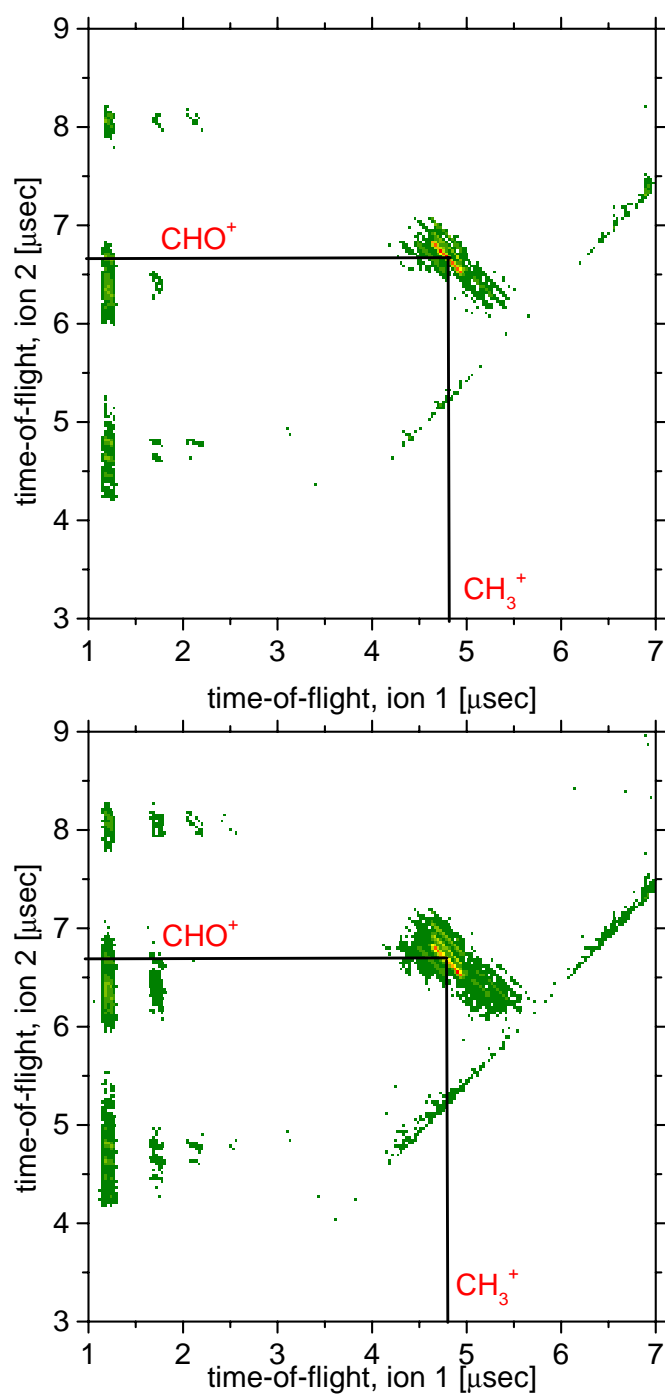


Figure 6.4: Top and bottom panel figures show the coincidence map of the correlated fragment ion pairs arising from the break-up of multiply charged C_2H_5OH and C_2H_5OD , respectively.

6.3.1 Preferred channels

We will mainly focus on the dominant fragmentation channel in the map, i.e. the ion pair at ($m/q = 15 : m/q = 29$) from h-ethanol. $m/q = 15$ is uniquely assigned to CH_3^+ . The ion at $m/q = 29$ can be $C-OH^+$ or $H-C-O^+$. If the O-H bond breaks, the ion formed is $H-CO^+$; if it does not, $C-OH^+$ is formed. The O-H bond has the highest bond energy of all. If we base our argument on bond strength alone, the O-H bond is the least likely to break. Whether this is true in the formation of the ion corresponding to $m/q = 29$ is resolved by comparing the coincidence maps of d-ethanol and h-ethanol (see Figure 6.4). For the case of d-ethanol, the most dominant ion pair is $m/q = 15 : m/q = 29$. This makes it clear that the second ion of the $m/q = 15 : m/q = 29$ pair is $H-CO^+$ and that it is the O-H bond that preferentially breaks in fragmentation of $C_2H_5OH^{2+}$. This evidence runs contrary to the expectation based on bond strength, but molecular orbital considerations can explain why the formation of $H-C-O^+$ is preferable.

The oxygen atom in C_2H_5OH possesses four non-bonding orbitals, two of which are free from mixing and have the lowest ionisation potentials of any of the electrons in the molecule. Hence, electrons from the oxygen atom can be removed easily [Mul35]. O^+ is trivalent, so the C-O- group in the neutral molecule becomes $C=[O^+]-$ in the ion, assuming that the charge is localised on the oxygen atom. Thus, $[H-C\equiv O]^+$ is more stable than $[C\equiv O-H]^+$. Hence, it can be concluded that CHO^+ ion is preferentially formed as compared to $C_2H_5^+$ or COH^+ .

Conclusions drawn from the coincidence map and the molecular orbital argument go hand in hand. Thus, it is clear that the decay via the formation of $H-CO^+$ is the preferred pathway for dissociative double ionisation of ethanol.

6.3.2 Electronic energy levels

Figure 6.5 is the kinetic energy release spectrum of the channel $CH_3^+ : CHO^+$. The mean value of the KE sum for the break-up $C_2H_5OH^{2+} \rightarrow CH_3^+ + CHO^+ + H_2$ is 5.2 eV and for the break-up $C_2H_5OD^{2+} \rightarrow CH_3^+ + CHO^+ + HD$ is 5.1 eV.

The structures seen in the two distributions correspond to the number of pos-

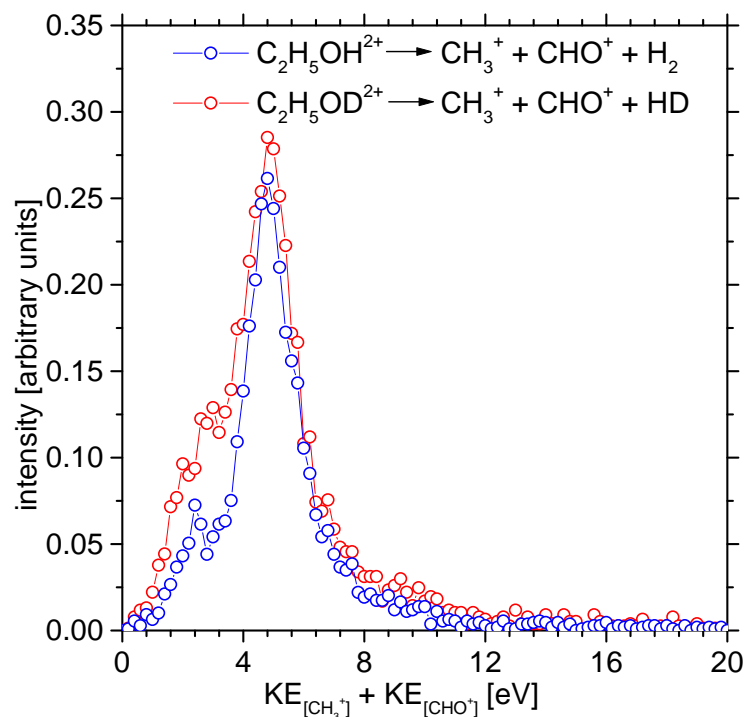


Figure 6.5: Kinetic energy sum of the fragment ions for the break-up $C_2H_5OH^{2+} \rightarrow CH_3^+ + CHO^+ + H_2$

sible electronically excited states of $C_2H_5OH^{2+}$ and $C_2H_5OD^{2+}$ involved in the break-up. The position of the peaks in the two cases are almost identical. This implies that same set of electronically excited energy levels are involved in the two break-ups. We have no quantum chemical calculations of this spectrum, so no assignments have been attempted.

6.3.3 Open questions

While we have been able to identify active sites and preferred decay channels, many questions remain. For example, we do not have a conclusive explanation of why certain pathways are more likely. Does the functional group play any role in rearrangement and dissociation? To answer these questions, it might help to perform experiments with other alcohols, or other molecules with the same skeleton but different functional groups. Patterns in selective bond breaking could

emerge from such studies. As is always the case, support from quantum chemical calculations will also be needed.

Chapter 7

Summary and future direction

7.1 Summary of the present work

The focus of the present work has been on the study of fragmentation dynamics of the multiply charged molecular ions using the technique of multi-hit momentum imaging. This is a powerful method to observe the mechanism of the fragmentation process. Multiply charged molecular ions in electronically excited states are generally unstable, and decay via different dissociation channels. The momentum distributions of the fragments from the dissociation of the precursor molecular ion reveal detailed information about the break-up. Energy levels of the electronically excited molecular ion, geometry of the dissociating molecular ion, preferential bond breakage etc can be derived from the kinematics of the fragments.

We built a momentum spectrometer in our laboratory to carry out the study. Multiply charged molecular ions are produced by 1300 eV electron interaction with a molecule. The electron energy is high enough to fall under the first Born regime, ensuring that the decay is unimolecular. We studied the fragmentation dynamics of the triatomic and polyatomic molecules.

No experimental data was available which could suggest the geometry of electronically excited molecular ions. The geometry of the precursor molecular ion is often different from that of the ground state. We have made a successful attempt to determine the geometry of electronically excited CO_2^{2+} molecular ions. Our study suggests that there exist two bent states of CO_2^{2+} . Both bent states have

symmetric and asymmetric stretch modes leading to dissociation. The one with symmetric stretch decays via the $\text{CO}_2^{2+} \rightarrow \text{O}^+ + \text{C} + \text{O}^+$ channel and the one with asymmetric stretch decays via the $\text{CO}_2^{2+} \rightarrow \text{O}^+ + \text{C}^+ + \text{O}$ channel. CO_2^{2+} is found to have a metastable state which decays via a two body break-up $\text{CO}_2^{2+} \rightarrow \text{O}^+ + \text{CO}^+$. Its lifetime, determined experimentally, is $5.8 \pm 1.5 \mu\text{s}$. On the basis of KER spectrum and concomitant quantum chemical calculations, we have determined the potential energy surfaces of CO_2^{2+} leading to the two body decay. The initial state of CO_2^{2+} for this break-up channel is assigned as $X^3\Sigma_g^-$.

We demonstrated that dissociating polyatomic molecular ions, whose neutrals have a centre of symmetry in their ground state, undergo a change in their geometry, accompanied by association of atoms within the molecular ion. We have established that the tetrahedral structure of CCl_4 changes to quasi-planar, and trigonal CCl_4^{2+} . Moreover, one of the Cl atoms breaks away from the central C atom and forms a bond with another Cl atom. The theoretically predicted structure of CCl_4^{2+} is in qualitative agreement with the experimentally deduced structure. Similarly, the geometry of SF_6^{2+} is found to change from the octahedral geometry of the neutral. A firm conclusion about the change could not be drawn. No calculations are available for this molecular ion. Our estimation of the geometry of the dications will simplify the calculation for their PES by providing input parameters for the geometry.

We have shown that the stability of fragment ions arising from dissociation of these molecules shows a certain pattern. The stability depends on whether the number of electrons in the fragment molecular ion is odd or even. The stability pattern of SF_6 fragments is explained by the valence bond model, but the model fails for CCl_4 .

Similar to the case of CCl_4 and SF_6 , intramolecular migration was also seen in dissociative ionisation of $\text{C}_2\text{H}_5\text{OH}$. This is exemplified by the observation of H_2^+ and H_3^+ peaks in the mass spectrum of $\text{C}_2\text{H}_5\text{OH}$. These ions can only be formed by breaking of bonds between the H and skeletal C or O atoms, followed by association of the H atoms or ions. We determined the most active H sites for rearrangement that leads to the formation of H_2^+ and H_3^+ . We deduced that the

formation of H_3^+ due to the breaking of the O–H bond and rearrangement of the H atoms on the CH_2 site is more likely than its formation involving atoms from the CH_3 site alone. No such difference was seen in case of the H_2^+ ion. Although there have been reports of site-specificity of bond breaks, no report of a quantitative estimate is found in the literature. In the dissociative double ionisation of $\text{C}_2\text{H}_5\text{OH}$, we demonstrated that the most probable decay channel leads to the formation of $[\text{HC-O}]^+$ rather than $[\text{C-OH}]^+$ ions. This implies preferential breaking of the O–H bond, even though the O–H bond is the strongest bond in that molecule.

7.2 A view into the future

The ionisation source used for our experiments was an electron beam. Electron impact ionisation follows hardly any selection rules, enabling the excitation of a wide range of states, including optically forbidden ones. However photon excitation has the advantage of energy selectivity. This might prove useful for breaking a specific bond of a complex molecular system and for understanding processes close to threshold. Controlling the energy may enable us to bring about transitions from one structure to another, including those transitions in which molecular bonds are broken and new bonds are formed. In line with this, we have set-up a momentum spectrometer at the INDUS-1 synchrotron. Another idea is selective excitation of the target molecules to a specific electronic state and then probing the potential energy surfaces of the excited molecular system.

For another class of studies of fragmentation dynamics of molecular ions, we have started some experiments at the Inter-University Accelerator Centre, Delhi, in which we will use a low energy oxygen ion beam as a projectile. The interaction of low energy oxygen ions with a diatomic molecule like CO or NO may form a short lived multiply charged triatomic molecule. The behaviour of this multiply charged molecular ion will be studied and compared with the unimolecular dissociation of the corresponding multiply charged triatomic molecular ion.

The reaction dynamics of multiply charged ions – both in the gas phase and

at the gas-surface interface, i.e. when the reactions are no longer unimolecular – are expected to be far more complicated because of the competition between different collision pathways. Such pathways include charge transfer, dissociative charge transfer, collision-induced dissociation and chemical reactions. Measurements on propensities for each of the possible pathways, as a function of collision energy can be carried out, accompanied by accurate calculations of PES for the various electronic states involved in the collision process. These will lead us to understanding reactive chemistry and provide new insights into the interaction of multiply charged ions with other species.

Bibliography

- [Ali92] R Ali, V Frohne, C L Cocke, M Stöckli, S Cheng, M L A Raphaelian, *Phys. Rev. Lett.*, **69**, 2491 (1992).
- [Ama69] Jr U Amaldi, A Egidi, R Marconero and G Pizzella, *Rev. Sci. Instrum.*, **40**, 1001 (1969).
- [Asc03] D Ascenzi, P Franceschi, P Tosi, D Bassi, M Kaczorowska, J N Harvey, *J. Chem. Phys.*, **118**, 2159 (2003).
- [Bak01] B L G Bakker, D H Parker, and W J van der Zande, *Phys. Rev. Lett.*, **86**, 3272 (2001).
- [Ban04] D P K Banerjee, W P Varricatt and N.M. Ashok, *Ap. J. (Letters)*, **615**, L53 (2004).
- [Bap99] B Bapat, R Moshhammer, S Keller, W Schmitt, A Cassimi, L Adoui, H Kollmus, R Dörner, Th Weber, K Khayyat, R Mann, J P Grandin and J Ullrich, *J. Physics B*, bf 32, 1859 (1999).
- [Bap00] B Bapat, S Keller, R Moshhammer, R Mann and J Ullrich, *J. Physics B*, **33**, 1437 (2000).
- [Bey52] J H Beynon, R M Caprioli and J W Richardson, *J. Am. Chem. Soc.*, **93**, 1852 (1971).
- [Bor26] M Born, *Z. Phys.*, **38**, 803 (1926).
- [Bri07] J P Brichta, S J Walker, R Helsten and J H Sanderson, *J. Phys. B*, **40**, 117 (2007).

- [Bry00] W A Bryan, J H Sanderson, A El-Zein, W R Newell, P F Taday and A J Langley, *J. Phys. B*, **33**, 745 (2000).
- [Cas96] A Cassimi, S Duponchel, X Flechard, P Jardin, P Sortais, D Hennecart and R E Olson, *Phys. Rev. Lett.*, **76**, 3679 (1996).
- [Chr83] *Electron-Molecule Interaction and their Applications*, Volume 1 and 2, Edited by L G Christophorou (Academic Press, Inc., 1983).
- [Coo65] R G Cooks, D T Terwilliger and J H Beynon, *J. Chem. Phys.*, **42**, 1208 (1965).
- [Cor95] C Cornaggia, M Schmidt and D Normand, *Phys. Rev. A*, **51**, 1431 (1995).
- [Cor96a] C Cornaggia, *Phys. Rev. A*, **54**, R2555 (1996).
- [Cor96b] C Cornaggia, F Salin and C Le Blanc, *J. Phys. B*, **29**, L749 (1996).
- [Cur85] D M Curtis and J H D Eland, *International Journal of Mass Spectrometry and Ion Process*, **63**, 241 (1985).
- [CHIA] <http://www.journals.uchicago.edu/ApJ/journal/issues/ApJS/v162n1/63297/63297.html>.
- [Dal76] A Dalgarno and J H Black, *Rep. Prog. Phys.*, **39**, 573 (1976).
- [Dor93] R Dörner, J Ullrich, R E Olson, O Jagutzki, H Schmidt-Böcking, *Phys. Rev. A*, **47**, 3845 (1993).
- [Dor94] R Dörner, V Mergel, R Ali, U Buck, C L Cocke, K Froschauer, O Jagutzki, S Lencinas, W E Meyerhof, S Nüttgens, R E Olson, H Schmidt-Böcking, L Spielberger, K Tökesi, J Ullrich, M Unverzagt, and W Wu, *Phys. Rev. Lett.*, **72**, 3166 (1994).
- [Dor96] R Dörner, J M Feagin, C L Cocke, H Bräuning, O Jagutzki, M Jung, E P Kanter, H Khemliche, S Kravis, V Mergel, M H Prior, H Schmidt-Böcking, L Spielberger, J Ullrich, M Unverzagt, and T Vogt, *Phys. Rev. Lett.*, **77**, 1024 (1996).

- [Dur89] N Duric, I Čadež, and M Kurepa, *Fizika (Zagreb)*, **21**, 339 (1989).
- [Ehr69] H Ehrhardt, M Schulz, T Tekaatt and K Willmann, *Phys. Rev. Lett.*, **22**, 89 (1969).
- [Ela87a] J H D Eland, *Chem. Phys. Lett.*, **201**, 353 (1987).
- [Ela87b] J H D Eland, *Mol. Phys.*, **61**, 725 (1987).
- [Ela87a] J H D Eland, L A Coles and H Bountra, *International Journal of Mass Spectrometry and Ion Process*, **89**, 265 (1989).
- [Ela91] J H D Eland, *Laser Chem.*, **11**, 259 (1991).
- [Fie93] T A Field and J H D Eland, *Chem. Phys. Lett.*, **211**, 436 (1993).
- [Fra86] L J Frasinski, M Stankiewicz, K J Randall, P A Hatherly and K Codling, *J. Phys. B*, **19**, L819 (1986).
- [Fra03] P Franceschi, R Thissen, J Žabka, J Roithová, Z Herman, O Dutuit, *Int. J Mass Spectrom.*, **228**, 507 (2003).
- [Fur05] Yusuke Furukawa, Kennosuke Hoshina, Kaoru Yamanouchi and Hidetoshi Nakano, *Chemical Physics Letters*, **414**, 117 (2005).
- [Glu03] K Gluch, J Fedor, S Matt-Leubner, R Parajuli, C Mair, A Stamatovic, O Echt, C Lifshitz, J Harvey, F Hagelberg, Z Herman, M Probst, P Scheier, and T D Märk, *Eur. Phys. J. D*, **24**, 131 (2003).
- [His99a] A Hishikawa, A Iwamae and K Yamanouchi, *Phys. Rev. Lett.*, **83**, 1127 (1999).
- [His99b] A Hishikawa, A Iwamae and K Yamanouchi, *J. Chem. Phys.*, **111**, 8871 (1999).
- [Hit79] A P Hitchcock and M J Van der Wiel, *J. Phys. B*, **12**, 2153 (1979).
- [Hoc98] M Hochlaf, F R Bennett, G Chambaud, P Rosmus, *J. Phys. B*, **31**, 2163 (1998).

- [Hoc95] H Hogreve, *J. Phys. B*, **28**, L263 (1995).
- [Hsi95] S Hsieh and J H D Eland, *J. Chem. Phys.*, **103**, 1006 (1995).
- [Hsi95] S Hsieh and J H D Eland, *J. Phys. B*, **30**, 4515 (1997).
- [Iwa01] A Iwasaki, A Hishikawa and K Yamanouchi, *Chem. Phys. Lett.*, **346**, 379 (2001).
- [Jag98] O Jagutzki, V Mergel, K Ullmann-Pfleger, L Spielberger, U Meyer, R Dörner, and H Schmidt-Böcking, *Imaging Spectroscopy IV, Proceedings of International Symposium on Optical Science Engineering and Instrumentation*, Eds. M. R. Descour & S.S. Shen, Proc. SPIE, **3438**, 322 (1998).
- [Jag06] MSc Thesis of Jagannath Mondal (2006).
- [Jan02] T Jahnke, Th Weber, A L Landers, A Knapp, S Schössler, J Nickles, S Kammer, O Jagutzki, L Schmidt, A Czasch, T Osipov, E Arenholz, A T Young, R Diez Muino, D Rolles, F J Garcia de Abajo, C S Fadley, M. A. Van Hove, S K Semenov, N A Cherepkov, J Rösch, M H Prior, H Schmidt-Böcking, C L Cocke and R Dörner, *Phys. Rev. Lett.*, **88**, 073002 (2002).
- [Kam95] T Kambara, J Z Tang, Y Awaya, B D DePaola, O Jagutzki, Y Kanai, M Kimura, T M Kojima, V Mergel, Y Nakai, H Schmidt-Böcking and I Shimamura, *J. Phys. B*, **28**, 4593 (1995).
- [Kay88] D C Kayser, W T Chater, A B Christensen, C K Howey, and J B Pranke, *Ultraviolet technology II*, Edited by R E Huffman, 119 (1988)
- [Kea87] G M Keating, R W Shorthill, H Masursky and L S Elson, *Adv. Space Res.*, **7**, 50 (1987).
- [Kel00] S Keller, B Bapat, R Moshhammer, J Ullrich and R M Dreizler, *J. Phys. B*, **33**, 1447 (2000).
- [Kis87] J Kissel and F R Kruger, *Adv. Space Res.*, **15**, 59 (1995).

- [Kri04] M Krishnamurthy, F A Rajgara, and D Mathur, *J. Chem. Phys.*, **121**, 9765 (2004).
- [Las01] L Laskin and C Lijshiz, *J. Mass Spect.*, **36**, 459 (2001).
- [Lah89] A Lahmam-Bennani, C Dupré and A Duguet, *Phys. Rev. Lett.*, **63**, 1582 (1989).
- [Leg05] S Legendre, E Giglio, M Tarisien, A Cassimi, B Gervais and L Adoui, *J. Phys. B*, **38**, L233 (2005).
- [Lev05a] Raphael D Levine, *Molecular Reaction Dynamics*, (Cambridge University Press, 2005).
- [Lev05b] Ira N Levine, *Quantum Chemistry*, (Pearson Education, 2005).
- [Liu89] J W Liu, *J. Phys. B*, **22**, 2605 (1989).
- [Mai03] C Mair, Z Herman, J Fedor, M Lezius, T D Märk, *J. Chem. Phys.*, **118**, 1479 (2003).
- [McC65] K E McCulloh, T E Sharp and H M Rosenstock, *J. Chem. Phys.*, **42**, 3501 (1965).
- [Man80] A P C Mann and D A Williams, *Nature*, **283**, 721 (1980).
- [Mas69] *Electronic and Ionic Impact Phenomena*, Volume 1, Edited by H S W Massey and E H S Burhop (Clarendon Press, 1969).
- [Mer95a] V Mergel, R Dörner¹, J Ullrich, O Jagutzki, S Lencinas, S Nüttgens, L Spielberger, M Unverzagt, C L Cocke, R E Olson, M Schulz, U Buck, E Zanger, W Theisinger, M Isser, S Geis, and H Schmidt-Bööcking, *Phys. Rev. Lett.*, **74**, 2200 (1995).
- [Mer95b] V Mergel, R Dörner¹, J Ullrich, O Jagutzki, S Lencinas, S Nüttgens, L Spielberger, M Unverzagt, C L Cocke, R E Olson, M Schulz, U Buck and H Schmidt-Bööcking, *Nucl. Instrum. Method. B*, **95**, 593 (1995).

- [Mil86] P Millie, I Nenner, Pi Archirel, P Lablanquie, P Fournier and J H D Eland, *J. Chem. Phys.*, **84**, 1259 (1986).
- [MOL] MOLPRO is a package of ab initio programs written by H J Werner and J P Knowles with contributions from J Almlöf, R D Amos, M J O Deegan, S T Elbert, W Meyer, K Peterson, R Pitzer, A J Stone and P R Taylor. The calculation has been done by out collaborators at IIT-Kanpur.
- [Mor83] Michael A Morrison, *Aust. J. Phys.*, **36**, 239 (1983).
- [Mos96a] R Moshhammer, M Unverzagt, W Schmitt, J Ullrich and H Schmidt-Böcking, *Nuclear Instruments and Methods B*, **108**, 425 (1996).
- [Mos96b] R Moshhammer, J Ullrich, H Kollmus, W Schmitt, M Unverzagt, O Jagutzki, V Mergel, H Schmidt-Böcking, R Mann, C J Woods, and R E Olson, *Phys. Rev. Lett.*, **77**, 1242 (1996).
- [Mos97] R Moshhammer, J Ullrich, H Kollmus, W Schmitt, M Unverzagt, H Schmidt- Böcking, C J Wood and R E Olson, *Phys. Rev. A*, **56**, 1351 (1997).
- [Mul35] Mulliken, *J. Chem. Phys.*, **3**, 506 (1935).
- [Nag94] K Nagesha, V R Marathe, E Krishnakumar and Bhas Bapat, *Chemical Physics Letters*, **230**, 283 (1994).
- [Nas96] A H Al-Nasir, M A Chaudhry, A J Duncan, R Hippler, D M Campbell and H Kleinpoppen, *J. Phys. B*, **29**, 1849 (1996).
- [Neu40] David A Neufeld and A Dalgarno, *Phy. Rev. A*, **40**, 633 (2005).
- [New64] A S Newton and A F Sciamanna, *J. Chem. Phys.*, **40**, 718 (1964).
- [NIST] <http://www.nist.gov/srd/atomic.htm>.
- [Par03] David Parker, *Imaging in Molecular Dynamics*, Edited by B J Whitaker (Cambridge University Press, 2003).

- [Pra05] A K Pradhan, D W Norcross, and D G Hummer, *Phy. Rev. A*, **23**, 619.
- [Qay04] A Qayyum, Z Herman, T Tepnual, C Mair, S Matt-Leubner, P Scheier, T D Märk, *J. Phys. Chem. A*, **108**, 1 (2004).
- [Red03] Tim Reddish, *Nature*, **431**, 404 (2003).
- [Rej02] R Rejoub, C D Morton, B G Lindsay, and R F Stebbings, *J. Chem. Phys.*, **118**, 1786 (2003).
- [Roent] <http://www.roentdek.com>.
- [Ruh90] E Ruhl, S D Price, S Leach, and J H D Eland, *Int. J. Mass Spec. Ion Proc.*, **97**, 175 (1990).
- [San99] J H Sanderson, A El-Zein, W A Bryan, W R Newell, A J Langley, and P F Taday, *Phys. Rev. A*, **59**, R2567 (1999).
- [Sav95] D W Savin, L D Gardner, D B Reisenfeld, A R Young, and J L Kohl, *Rev. Sci. Instrum.*, **66**, 67 (1995).
- [Sch93] O Schwarzkopf, B Krässig, J Elmiger, and V Schmidt, *Phys. Rev. Lett.*, **70**, 3008 (1993).
- [Sha06a] V Sharma and B Bapat, *J. Chem. Phys.*, **125**, 044305 (2006).
- [Sha06b] V Sharma, B Bapat, *Eur. Phys. J. D*, **37**, 223 (2006).
- [Sha07] Vandana Sharma, Bhas Bapat, Jagannath Mondal, M Hochlaf, Kousik Giri and N Sathyamurthy, *J. Phys. Chem.*, DOI: 10.1021/jp070257k, (2007).
- [Sie00] B Siegmann, U Werner, R Mann, N M Kabachnik, and H O Lutz, *Phys. Rev. A*, **62**, 022718 (2000).
- [Sie02a] B Siegmann, U Werner, Z Kaliman, Z Roller-Lutz, N M Kabachnik, and H. O. Lutz, *Phys. Rev. A*, **66**, 052701 (2002).

- [Sie02b] B Siegmann, U Werner, H O Lutz and R Mann, *J. Phys. B*, **35**, 3755 (2002).
- [Sin06] R K Singh, G S Lodha, Vandana Sharma, I A Prajapati, K P Subramanian, and B Bapat, *Phys. Rev. A*, **74**, 022708 (1996).
- [Sin03] R K Singh, R Hippler and R Shanker, *Phys. Rev. A*, **67**, 022704 (2003).
- [Spi95] L Spielberger, O Jagutzki, R Dörner, J Ullrich, U Meyer, V Mergel, M Unverzagt, M Damrau, T Vogt, I Ali, Kh Khayyat, D Bahr, H G Schmidt, R Frahm, and H Schmidt-Böcking, *Phys. Rev. Lett.*, **74**, 4615 (1995).
- [Spi96] L Spielberger, O Jagutzki, B Krässig, U Meyer, Kh Khayyat, V Mergel, Th Tschentscher, Th Buslaps, H Bräuning, R Dörner, T Vogt, M Achler, J Ullrich, D S Gemmell, and H. Schmidt-Böcking, *Phys. Rev. Lett.*, **76** 4685 (1996).
- [Sri96] S K Srivastava, E Krishnakumar, A F Fucaloro, and T van Note, *J. Geophys. Res.*, **101**, 26155 (1996).
- [Str96] H C Straub, B G Lindsay, K A Smith, and R F Stebbings, *J. Chem. Phys.*, **105**, 4015 (1996).
- [Tak05] M Takahaschi, N Watanabe, Y Khajuria, Y Udagawa and J H D Eland, *Phys. Rev. Lett.*, **94**, 213202 (2005).
- [Tar00] M Tarisien, L Adoui, F Frémont, D Leli'evre, L Guillaume, J-Y Chesnel, H Zhang, A Dubois, D Mathur, Sanjay Kumar, M Krishnamurthy and A Cassimi, *J. Phys. B*, **33**, L11 (2000).
- [Tia98] Cechan Tian and C R Vidal, *Phys. Rev. A*, **58**, 3783 (1998).
- [Tom01] S Tomita, H Lebius, A Brenac, F Chandezon, and B A Huber, *Phys. Rev. A*, **65**, 053201 (2001).
- [Tsai80] B P Tsai and J H D Eland, *Int. J. Mass. Spec. Ion Phys.*, **36**, 143 (1980).

- [Ueda03] K Ueda, A De Fanis, N Saito, M Machida, K Kubozuka, H Chiba, Y Muramatsu, Y Sato, A Czaschd, O Jaguzki, R Dörner, A Cassimi, M Kitajima, T Furuta, H Tanaka, S L Sorensen, K Okada, S Tanimoto, K Ikejiri, Y Tamenori, H Ohashi, I Koyano, *Chemical Physics*, **289**, 135 (2003).
- [Ull97] J Ullrich, R Moshhammer, R Dörner, O Jagutzki, V Mergel, H Schmidt-Böcking and L Spielberger, *J. Phys. B*, **30**, 2917 (1997).
- [Ull03a] J Ullrich, R Moshhammer, A Dorn, R Dörner, L P Schmidt and H Schmidt-Böcking, *Rep. Prog. Phys.*, **66**, 1463 (2003).
- [Ull03b] *Many-Particle Quantum Dynamics in Atomic and Molecular Fragmentation*, Edited by J Ullrich and V P Shevelko (Springer, 2003).
- [Wil55] W C Wiley and I H McLaren, *Rev. Sci. Instrum.*, **26**, 1150 (1955).
- [Woo77] R M Wood, A K Edwards, and M F Steuer, *Phys. Rev. A*, **15**, 1433 (1977).

Publications

In Journals

1. Energy levels and metastability of CO_2^{2+} : experimental measurement and ab-initio prediction
Vandana Sharma, Bhas Bapat, Jagannath Mondal, Kousik Giri, N Sathya-murthy, M Hochlaf, *J. Phys. Chem.* DOI: 10.1021/jp070257k (2007).
2. Evidence for alteration of molecular symmetry during dissociative ionisation
Vandana Sharma and Bhas Bapat, *Phys. Rev. A*, **75**, 040503(R) (2007).
3. Bent dissociative states of CO_2^{2+}
Bhas Bapat and Vandana Sharma, *J. Phys. B*, **40**, 13 (2007).
4. Determination of active sites for H atom rearrangement in dissociative ionisation of ethanol
Vandana Sharma and Bhas Bapat, *J. Chem. Phys.*, **125**, 044305 (2006).
5. Triply charged carbon dioxide molecular ion: Formation and fragmentation
R K Singh, G S Lodha, Vandana Sharma, I A Prajapati, K P Subramanian, B Bapat, *Phys. Rev. A*, **74**, 022708 (2006).
6. Mean kinetic energy of molecular fragment ions from time-of-flight and momentum analysis
Bhas Bapat and Vandana Sharma, *Int. J. Mass Spec.*, **251**, 10 (2006).

7. An apparatus for studying momentum-resolved electron-impact dissociative and non dissociative ionisation
Vandana Sharma and Bhas Bapat, *Eur. Phys. J. D*, **37**, 223 (2006).
8. Role of symmetry in dissociation of symmetric molecules
Under preparation.
9. Comparative study of site specific dissociation of dicationic ethanol and methanol
Under preparation.

Conference presentations

- Recoil Ion Momentum Spectrometer
Vandana Sharma and Bhas Bapat, 11th ISMAS workshop on Mass Spectrometry, Simla, India, 7th–12th October 2004.
- Momentum Spectroscopic studies of carbon dioxide
Vandana Sharma and Bhas Bapat, XV National Conference on Atomic and Molecular Physics, Ahmedabad, India, 20th–23rd December 2004.
- Recoil Ion Momentum Spectroscopy
Vandana Sharma and Bhas Bapat, XV National Conference on Atomic and Molecular Physics, Ahmedabad, India, 20th–23rd December 2004.
- Momentum spectra of electron-impact fragmentation of CO₂
Vandana Sharma and Bhas Bapat, X05 – The 20th International Conference on X-ray and Inner Shell Processes, Melbourne, Australia, 4th–8th July 2005.
- Ion-ion coincidence measurement of fragments of C₂H₅OH using RIMS
Vandana Sharma and Bhas Bapat, Topical Conference on Atomic and Molecular Physics, Kolkata, India, 11th–15th December 2005.

- Fragmentation study of ethanol by electron-ion-ion coincidence technique
Vandana Sharma and Bhas Bapat, Current Developments in Atomic, Molecular and Optical Physics, Delhi, India, 21st–23rd March 2006.
- Geometry of dissociating molecular ions
Vandana Sharma and Bhas Bapat, XVI National Conference on Atomic and Molecular Physics, Ahmedabad, India, 8th–11rd January 2007.
- Role of symmetry in dissociation of highly symmetric molecules
Vandana Sharma and Bhas Bapat, International Conference on Photonic, Electronic and Atomic Collisions, Freiburg, Germany 25th–31st July 2007.

Acknowledgements

My last remaining task is to acknowledge all those people who have contributed to the work described in this thesis. This is an impossible task, given that many people have helped me to design and implement, have criticised and sponsored the work. I am going to try anyway, and if your name is not listed, rest assured that my gratitude is not less than for those listed below.

This thesis represents not only my work at the keyboard, it is a milestone in my stay in the Atomic and Molecular Physics Laboratory. My experience at PRL has been nothing short of amazing. I have been given unique opportunities and I have taken advantage of them. This thesis is the result of many experiences I have encountered at PRL from dozens of remarkable individuals whom I wish to acknowledge. First and foremost I wish to thank my advisor, Dr Bhas Bapat. He has been supportive since the days I began working on my experimental system. I remember he used to say whenever we used to open our chamber for the modification without getting any result . . . this time the problem would be solved and we won't have to reopen our chamber . . . to encourage me to stay in the lab. Ever since, he has supported me not only by providing a research assistantship over almost all the years of my research, but also academically and emotionally through the rough road to the completion of this thesis. He helped me come up with the thesis topic and guided me over almost an year of development. And during the most difficult times when writing this thesis, he gave me the moral support and the freedom I needed for moving on. His enthusiasm and words of motivation have always inspired me and helped me to do better each time. It is thanks to him that I enjoyed my journey through the atomic and molecular

wonderland.

In no way less brilliant is Dr K P Subramanian, to whom I am much obliged for his merciless comments, for unerringly revealing weak points in my arguments. I praise the enormous amount of help and teaching by him throughout these years. Timely help from O Jagutzki and K Ullmann-Pfleger of Roentdek GmbH in matters related to data acquisition is also acknowledged.

During my tenure we have performed experiments at Centre for Advance Technology (CAT), Indore and Inter-University Accelerator Centre (IUAC), Delhi. The experiments could not have been possible without the help of the staff at CAT and IUAC. I am grateful to all of them, specially to Dr G S Lodha , Dr C P Safvan, Sankar De and Jyoti Rajput.

Experiments and theory go hand in hand. I have benefited from the theoretical expertise of Prof N Sathyamurthy and his students specially Jagannath and Pradeep of IIT-Kanpur. I thank them all.

Special thanks to Prof Maarten Vos from Australian National University at Canberra, Australia for hosting me in their group. I am also grateful to Dr Julian Lower and Susan Belm who made my life easy far from motherland.

I thank Dr S D Rindani, Prof S K Bhattacharya, Dr P Sharma and all other members of academic committee for critically reviewing the progress of my work and giving valuable suggestions at various stages of my research.

I sincerely thank colleagues in the group, R K Singh, I A Prajapati, A P Gohil and V K Lodha, for their continuous assistance in the setting up of my experimental apparatus and for their constructive criticism and encouragement. I also acknowledge with thanks the generous support of the staff of the mechanical workshop, library, maintenance, liquid nitrogen plant, computer centre and accounts section. Special thanks are due to P Ubale, H R Vaghela, Jigar Raval, G G Dholakia, Hitendra Mishra, Alok Shrivastava, G K K Sivasankaran, M P Kurup, Nishtha, Uma Desai, Parul Parikh, A Puthawala and A K Jain for their help.

I am deeply indebted to all other members of Space and Atmospheric Sciences division for their constant encouragement through thoughts and ideas. I specially acknowledge Prof Shyam Lal, Prof A Jayaraman, Dr R Sekar, Dr S Ra-

machandran, Dr Varun Sheel and Dr S A Haider.

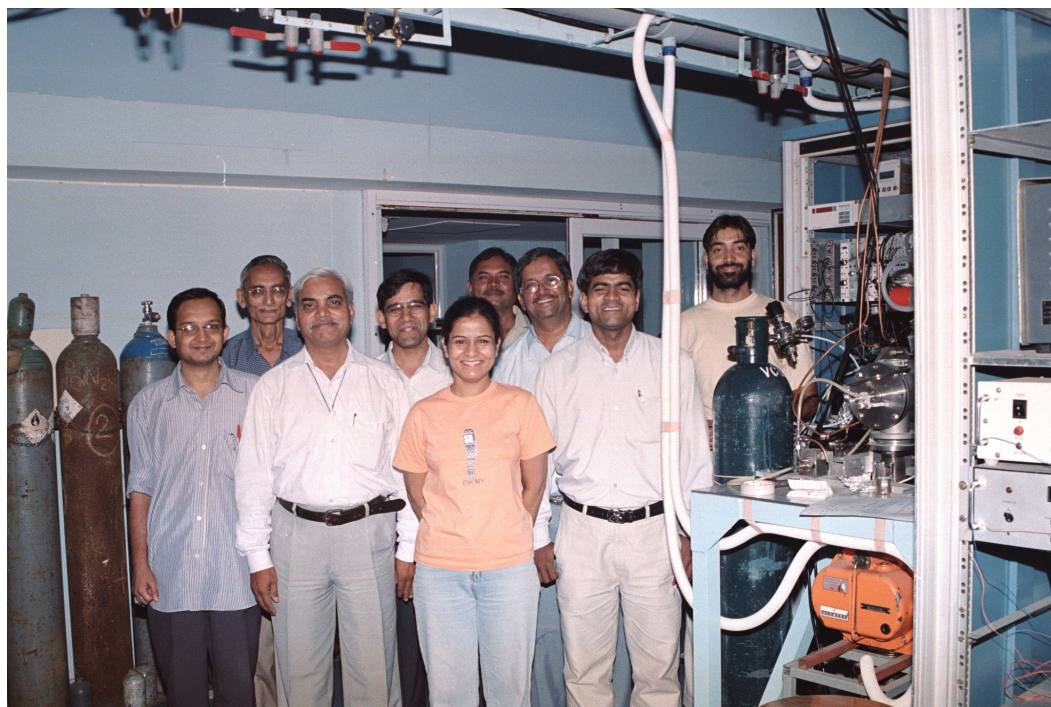
I am deeply indebted to my colleague and friend, Antra, who has been an inspiration on how to make things 'perfect'. A special acknowledgement goes to her for many years of help and meaningful discussions, and the fun we had both inside and outside the laboratory. Together we managed to overcome the days of exertion of a PhD student. Special thanks go to her and Dilip, who helped me in the hard times of illness.

I would like to express my gratitude to other colleagues in my laboratory Bhavesh, Rajesh, and Nabi, for fruitful discussions and various insights and also have been supportive in every way. I extend my gratitude to my other colleagues S B Banerjee, Dibyendu Chakrabarty, Som Kumar Sharma, R D Deshpande, Amit and Uma.

I would like to thank Department of Space for offering a research scholarship and providing the necessary facilities.

The contribution of hostel canteen and PRL's canteen is no means small. A great thank-you goes to all the staff members of the canteen and the hostel who have taken care of daily needs.

I end with my home town, Khetri Nagar, where the most basic source of my life resides – my family. Their support has been unconditional all these years; they have cherished with me every great moment and gave me support whenever I needed it.



My group at Physical Research Laboratory. From left: Bhavesh Patel, A P Gohil, I A Prajapati, Bhas Bapat, myself, V K Lodha, K P Subramanian, Rajesh Kushawaha, Gulam Nabi Dar.